12-16-2010 12:00 AM

Improvements in Cardiac Spect/CT for the Purpose of Tracking Transplanted Cells

Eric Sabondjian, *The University of Western Ontario*

Supervisor: Robert Z. Stodilka, *The University of Western Ontario*

A thesis submitted in partial fulfillment of the requirements for the Doctor of Philosophy degree in Medical Biophysics

IMPROVEMENTS IN CARDIAC SPECT/CT FOR THE PURPOSE OF TRACKING TRANSPLANTED CELLS

(Spine title: Improving SPECT/CT for tracking transplanted cells)

(Thesis format: Integrated-Article)

by

Eric Sabondjian

Graduate Program
in
Medical Biophysics

A thesis submitted in partial fulfillment
of the requirements for the degree of
Doctor of Philosophy

School of Graduate and Postdoctoral Studies
The University of Western Ontario
London, Ontario, Canada

THE UNIVERSITY OF WESTERN ONTARIO
SCHOOL OF GRADUATE AND POSTDOCTORAL STUDIES

CERTIFICATE OF EXAMINATION

Supervisor	Examiners
Dr. Robert Z. Stodilka	Dr. Curtis B. Caldwell
Supervisory Committee	Dr. Jonathan Romsa
Dr. Frank S. Prato	Dr. R. Terry Thompson
Dr. R. Terry Thompson	Dr. Eugene Wong
Dr. Gerald Wisenberg	

The thesis by

Eric Sabondjian

entitled:

IMPROVEMENTS IN CARDIAC SPECT/CT FOR THE PURPOSE OF TRACKING TRANSPLANTED CELLS

is accepted in partial fulfillment of the
requirements for the degree of
Doctor of Philosophy

Date_____ _____
Chair of the Thesis Examination Board

ABSTRACT

Regenerative therapy via stem cell transplantation has received increased attention to help treat the myocardial injury associated with heart disease. Currently, the hybridisation of SPECT with X-ray CT is expanding the utility of SPECT. This thesis compared two SPECT/CT systems for attenuation correction using slow or fast-CT attenuation maps (μ-maps). We then developed a method to localize transplanted cells in relation to compromised blood flow in the myocardium following a myocardial infarction using SPECT/CT. Finally, a method to correct for image truncation was studied for a new SPECT/CT design that incorporated small field-of-view (FOV) detectors.

Computer simulations compared gated-SPECT reconstructions using slow-CT and fast-CT μ-maps with gated-CT μ-maps. Using fast-CT μ-maps improved the Root Mean Squared (RMS) error from 4.2% to 4.0%. Three canine experiments were performed comparing SPECT/CT reconstruction using the Infinia/Hawkeye-4 (slow-CT) and Symbia T6 (fast-CT). Canines were euthanized prior to imaging, and then ventilated. The results showed improvements in both RMS errors and correlation coefficients for all canines.

A first-pass contrast CT imaging technique can identify regions of myocardial infarction and can be fused with SPECT. Ten canines underwent surgical ligation of the left-anterior-descending artery. Cells were labeled with ^{111}In-tropolone and transplanted into the myocardium. SPECT/CT was performed on day of transplantation, 4, and 10 days post-transplantation. For each imaging session first-pass perfusion CT was performed and successfully delineated the infarct zone. Delayed-enhanced MRI was performed and correlated well with first-pass CT. Contrast-to-noise ratios (CNR) were calculated for ^{111}In-SPECT and suggested that cells can be followed for 11 effective half-lives.

We evaluated a modified SPECT/CT acquisition and reconstruction method for truncated SPECT. Cardiac SPECT/CT scans were acquired in 14 patients. The original projections were truncated to simulate a small FOV acquisition. Data was reconstructed in three ways: non-truncated and standard reconstruction (NTOSEM), which was our gold-standard; truncated and standard reconstruction (TOSEM); and truncated and a modified reconstruction (TMOSEM). Compared with NTOSEM, small FOV imaging incurred an average cardiac count ratio error greater than 100% using TOSEM and 8.9% using TMOSEM. When we plotted NTOSEM against TOSEM and TMOSEM the correlation coefficient was 0.734 and 0.996 respectively.

Keywords: SPECT/CT, attenuation maps, slow-rotating CT, fast-rotating CT, stem cell imaging, first-pass perfusion CT, cell localization, ^{111}In labelling, contrast-to-noise ratio, local tomography, cardiac imaging, projection truncation.

CO-AUTHORSHIP

CHAPTER 2

Mr. Eric Sabondjian developed the experimental design, performed the experiments and the simulations, analysed all the data and wrote the manuscript. Benoit Lewden helped organize the simulation software and aided in computer programming. Dr. Martin King performed experiments and helped with experimental design. Dr. Gerry Wisenberg helped in revising the manuscript, and Drs Frank Prato and Robert Stodilka were also involved in revising the manuscript in addition to supervising the project.

CHAPTER 3

Mr. Eric Sabondjian established the SPECT/CT imaging protocols, acquired, reconstructed, and analyzed the data, in addition to drafting the manuscript and preparing it for submission. Andrea Mitchell was responsible for a large portion of data acquisition and cell preparation. Jane Sykes and Lela Deans performed the cardiac surgeries and delivered the epicardial cell injections. Dr. Kimberley Blackwood was involved with revisions. Dr. James White was responsible for the MR delayed enhancement data acquisition and was also involved in the revision process. Dr. Gerald Wisenberg played a role in the conception, and development of the study. He also delivered the endocardial injections, and was involved in the revision process. Drs. Frank Prato and Robert Stodilka were involved in the conception, and development of the study, and were involved on revisions to the manuscript in addition to supervising the project.

CHAPTER 4

Mr. Eric Sabondjian performed all image reconstructions and analysis, in addition to writing the manuscript. Dr. Tarik Belhocine acquired the patient data. Drs. Martin King and Gerald Wisenberg were involved in manuscript revisions. Drs. Frank Prato and Robert Stodilka were also involved with manuscript revisions in addition to supervising the project.

ACKNOWLEDGEMENTS

When a new tree is planted, it is typically tied to a large stick placed directly adjacent to it. This is done to make sure the young tree does not fall over due to the wind. When I began my path in the Ph. D. program, I was this young tree, but instead of only one stick keeping me up, I had many pillars. The winds at times were very strong, and without all these people I may not have remained standing. First and foremost was my supervisor Dr. Robert Stodilka, who has become a very close friend through the years. In addition to mentoring my project, he has taught me how to be successful in both my personal and professional life, and has provided me with all the tools to achieve both these goals. Dr. Frank Prato's office door was always open for me; whether it was to chat about science or just about anything else I could think of. He has been a tremendous mentor for me through the years at Lawson, and I will never forget all that he has done for me. Dr. Gerry Wisenberg was always there for me when I needed him, and trusted me and my abilities to solve any problem that came our way. Dr. Terry Thompson always had the time to answer any question I had, and I always enjoyed our quick chats in the Lawson hallways. Dr. Martin King was there for me during very difficult times. He has become a great friend, and I never know where the conversation will end up with Martin, it can range from rally racing to the dark matter in space. Thanks Martin! I will always be there for you, as you were for me. I'd like to thank Jane Sykes and Lela Deans who have become my family away from home. Jane has always taken great care of me, and made sure I was surviving during very difficult times. Lela was my big sister at Lawson, and we always had a blast working together. I would also like to thank Dominique Ouimet for the laughs, Jill MocCormick for the fun chats, and Jennifer Hadway for always yelling at me. I need to thank *Sifu* Steve Pascoe, who without

realizing helped me tremendously these past 6 years. He gave me the confidence and the ability to believe in myself so that I can achieve anything I set my sights on. Dr. Glenn Wells, who supervised my M.Sc. degree and taught me how to become a great scientist. I would also like to thank my close friend and office mate John Patrick, who without his encouragement and friendship I would never had made it to this point. Finally, I would like to thank my soul mate Susan Patrick. She helped me a great deal by believing in me, and supported me through all the ups and downs over the year. This is only the beginning, and the best is yet to come. I love you Susan! The future will only get harder, and I look forward to your love and support without which I would never succeed. Last but not least my family played a major role over the years. I need to thank all my grand-parents for the unconditional love they provided, my brother and sister for always being there and taking care of me. To conclude, I cannot forget all the sacrifices my Mom and Dad have made to give me the opportunity to succeed in every aspect of my life. They have been nothing but supportive and I owe them everything. Thanks to all these individuals for letting me lean on them through the years.

ACKNOWLEDGEMENTS

CHAPTER 2

The authors would like to thank the nuclear medicine staff at both London Health Sciences (University Campus), and St. Joseph's Health Care – London for the use of the medical imaging equipment. The authors would also like to thank Jane Sykes for helping with the animal studies, and transportation between hospital sites.

Financial support for this project was received from the Heart and Stroke Foundation of Ontario (Toronto, Ontario, Canada), the Canadian Institutes for Health Research (Ottawa, Ontario, Canada), and the Ontario Research Fund. This work was also funded by scholarships for Mr. Eric Sabondjian from the Canadian Institute of Health Research and the Ontario Graduate Scholarship in Science and Technology.

CHAPTER 3

The authors would like to thank Jennifer Hadway for supplying the CT contrast agent. The authors would also like to thank Drs. Aaron So and Ting-Yim Lee for useful discussions concerning CT acquisitions with contrast.

Financial support for this project was received from the Heart and Stroke Foundation of Ontario (Toronto, Ontario Canada), the Canadian Institutes for Health Research (Ottawa, Ontario, Canada), Ontario Research Fund, Siemens Medical Systems (Erlangen, Germany), Bayer AG Health Care (Leverkusen, Germany), and Boston Scientific (Natick, Massachusetts). This work was also funded by scholarships for Mr. Eric Sabondjian from the Canadian Institute of Health Research and the Ontario Graduate Scholarship in Science and Technology.

CHAPTER 4

The authors would like to thank Benoit Lewden for programming the defect size analysis code. This work involving the *Local OSEM* algorithm is the subject of a United States Provisional Patent: Stodilka RZ and Prato FS / Method and System for Performing Local Tomography / US Provision Patent Application 60/840,010.

This work was supported by grants from the Canadian Institutes of Health Research, the Natural Sciences and Engineering Research Council, the Canadian Foundation for Innovation, the Heart and Stroke Foundation of Canada, Cancer Care Ontario (distributed through the Cancer Imaging Network of Ontario), and the Ontario Research Fund (distributed through the Imaging in Cardiac Therapeutics and Multi-Magnetics Inc.).

TABLE OF CONTENTS

LIST OF TABLES

LIST OF FIGURES

LIST OF ABEVIATIONS

σ	- Standard Deviation
μ-map	- Attenuation Map
4D	- Four Dimensional
ACF	- Attenuation Correction Factor
AHA	- American Heart Association
^{64}Cu	- Copper-64
CdTe	- Cadmium Telluride
CNR	- Contrast to Noise Ratio
CT	- Computed Tomography
CTDI	- Computed Tomography Dose Index
CZT	- Cadmium Zinc Telluride
DE	- Delayed Enhancement
DE-MRI	- Delayed Enhanced Magnetic Resonance Imaging
DTPA	- Diethylenetriamine Penta-acetic Acid
ECG	- Echo-cardiograph
EPC	- Endothelial Progenitor Cell
^{18}F	- Fluorine-18
FBP	- Filtered Backprojection
FDG	- Fluorodeoxyglucose
FOV	- Field of View
FRC	- Functional Residual Capacity

FWHM	- Full Width Half Maximum
HBSS	- Hanks Balanced Salt Solution
LAD	- Left Anterior Descending
keV	- Kilo-electron Volt
^{111}In	- Indium-111
MAP-OSEM	- Maximum A Posteriori Ordered Subset Expectation Maximization
mAs	- Milliamp Second
MBq	- Mega-becquerel
mgI	- Milligrams of Iodide
MIBI	- Methoxyisobutyl Isonitrile
MLEM	- Maximum Likelihood Expectation Maximization
ml	- Milliliter
mm	- Millimeter
MPI	- Myocardial Perfusion Imaging
MRI	- Magnetic Resonance Imaging
NaI(Tl)	- Sodium Iodide doped with Thallium
NCAT	- NURBS based Cardiac-Torso
NTOSEM	- Non Truncated Ordered Subset Expactation Maximization
NURBS	- Non-Uniform Rational B-Spline
OSEM	- Ordered Subset Expectation Maximization
PET	- Positron Emission Tomography
PMT	- Photomultiplier tube

PTSM	- Pysuvaldehyde-Bis(N4-Methylthiosemicarbazone)
PSIR	- Phase-sensitive Inversion Recovery
RBI-EM	- Rescaled Block Iterative Expectation Maximization
RMS	- Root Mean Square
ROI	- Region of Interest
SD	- Standard Deviation
SEM	- Standard Error of the Mean
SimSET	- Simulation System for Emission Tomography
SPECT	- Single Photon Emission Computed Tomography
^{99m}Tc	- Technetium-99m
TC	- Transplanted Cell
TEW	- Triple Energy Window
TMOSEM	- Truncated Modified Ordered Subset Expactation Maximization
TOSEM	- Truncated Ordered Subset Expactation Maximization
TV	- Tidal Volume
VOI	- Volume of Interest

CHAPTER 1: GENERAL INTRODUCTION

1.1 INTRODUCTION

The World Health Organization estimates that by the year 2020 heart disease will be the number one cause of disability [1]. Therefore, methods to diagnose and treat heart disease will take on increasingly important roles in managing the health of the population.

This thesis focuses on myocardial infarction, which is the destruction of heart tissue resulting from obstruction or reduction of blood flow to the myocardium. Once the myocardium is damaged the contracting muscle is replaced by fibrotic scar over a period of months [2]. The self-healing or regenerative capacity of the heart is limited compared with other organs, because of the small number of native cardiac stem cells, making recovery from the infarction dependent upon medical intervention in the healing process [3].

Current treatments for heart disease involve medications, surgery or a combination or both. Patients with myocardial infarctions are currently treated acutely with medications such as blood thinners to reduce the risk for a second event in the short term; however, if blood flow remains compromised to the region of injury and there is still viable heart muscle, balloon angioplasty or bypass surgery may improve heart function and reduce the risk for another myocardial infarction [4]. In cases of extensive injury with little to no hope for improvement in function a heart transplant may be required. Unfortunately, transplant procedures have significant disadvantages including

severity of surgery, a scarcity of donor hearts, transplant rejection, and the requirement that the patient be on long term immunosuppressive therapy which increases the risk for infections and cancer.

One potential alternative to heart transplantation that is receiving increased attention over the past decade is regenerative therapy via stem cell transplantation [5]. The hope of this alternative is to restore the function of the original heart *in situ* in a minimally invasive manner. In 2001, Orlic et al reported that the cardiac transplantation of marrow-derived cells differentiated into cardiomyocytes and significantly reduced myocardial fibrosis in a mouse model [6]. Although this study sparked great interest in stem cell transplantation to help in myocardial regeneration, subsequent work in clinical trials did not show the same level of improvement and gave mixed results [7, 8, 9]. It is now clear that developing regenerative therapy is a very difficult undertaking that will require scientific discovery on many fronts, from molecular biology to biomaterials and imaging sciences. In addition, the optimum cell line to use, the route of administration of the cells, the timing of the transplant in relationship to the infarct, and whether the recipient tissue has been reperfused or is still subject to coronary occlusion still remains to be determined. For medical imaging, techniques to visualize cell delivery, degree of retention, and long-term survival are needed to help provide the answers to the above questions [10, 11].

1.2 IMAGING THE HEART FOR MONITORING STEM CELL THERAPY

Three popular modalities for cardiac imaging are: Magnetic Resonance Imaging (MRI), Positron Emission Tomography (PET), and Single Photon Emission Computed Tomography (SPECT). Cardiac applications on these modalities may require the use of exogenous contrast agents to measure aspects of tissue or vascular properties; or – in the case of cell therapies – the transplanted cells themselves.

A common contrast agent for MRI is Gadolinium-Diethylenetriamine Penta-acetic Acid (DTPA), which is marketed as Magnevist by Bayer Schering Pharma. Its paramagnetic property, in a concentration dependent fashion, reduces the T1 relaxation time (and to some extent the T2 and T2* relaxation times) in MRI, which is the source of its clinical utility. A popular method of using Gd-DTPA is for delayed enhancement MRI (DE-MRI) where the contrast agent is injected and allowed sufficient time (approximately 10 minutes depending on the exact protocol) to accumulate in infarcted regions, due to the breakdown in cellular membrane integrity, and then MR images are acquired [12]. MRI currently provides the most accurate means of identifying infarct extent and location [13].

In cell therapy applications, MRI may also be used to visualize specially-labeled cells that have been transplanted into the heart. One class of cellular label that has attracted considerable attention is nano-sized iron oxide particles, such as Super Paramagnetic Iron Oxide nanoparticles that are incorporated into the transplanted cells. MRI of transplanted iron oxide labeled cells has shown promise in several animal studies [14, 15]. However, interesting challenges for this label include the lack of specificity for intact, viable cells since the iron label from dead cells is taken up by macrophages that

are attracted as part of the inflammatory response to the infarction, and the dilution of the label that occurs while cells are dividing [10, 16].

Positron Emission Tomography (PET) is in widespread use for cardiac applications. Although perceived as expensive, it is currently enjoying tremendous growth that has only been accelerated by the ongoing shortage of reactor-produced radio-isotopes. Like MRI, PET too can image tissue properties and track labeled cells with the use of ^{18}F-fluorodeoxyglucose (^{18}F-FDG), but is limited by the short half-life (110 minutes) of the radioisotope and rapid clearance from labeled cells [17]. Recently, it has been shown that cells may also be labeled with ^{64}Cu-Pysuvaldehyde-Bis(N4-Methylthiosemicarbazone) (PTSM), allowing cells to be followed for longer periods of time than with ^{18}F-FDG. However, ^{64}Cu is not readily available and its half-life of 13-hours is still short for following cell lines over extended periods [18].

Single Photon Emission Computed Tomography (SPECT) is the most widely used nuclear medicine modality. Even with the availability of MRI and PET, the majority of myocardial perfusion studies are performed with SPECT. Like MRI and PET, SPECT can assess multiple parameters including the imaging of myocardial perfusion and the visualization of labeled stem cells. In addition, SPECT is multi-spectral; therefore multiple parameters may be assessed simultaneously if different radio-nuclides can be assigned to each parameter. For example, a ^{99m}Tc labeled molecule is typically used for perfusion imaging and allows inferring coronary obstruction to a limited extent [19]; while, transplanted cells can be labeled with an ^{111}In labeled molecule [20]. Since ^{99m}Tc and ^{111}In emit gamma rays of energies sufficiently different to be discriminated by a gamma camera, they can be imaged simultaneously by SPECT.

The radiotracer in wide-spread use for imaging cardiac blood flow is ^{99m}Tc-labeled methoxyisobutyl isonitrile (MIBI) [21]. ^{99m}Tc has a radioactive half-life of 6.02 hours and emits 140 keV gamma-rays. A popular protocol for MIBI SPECT involves comparing coronary perfusion in a resting state to the stressed state to detect stress-induced myocardial blood flow deficits. This test is typically included in the initial assessment of suspected ischemia, and as a prognostic indicator following infarction. Rest/Stress imaging requires two radioisotope injections, each one followed by SPECT imaging [19, 22]. The first injection takes place with the patient in a resting state, while the second injection takes place with the patient in a stressed state. Stress can either be induced by running on a treadmill to reach a certain specified heart rate (90% of maximum heart rate), or via intravenous injection of the vasodilator dipyridamole which induces coronary hyperemia, or the sympathomimetic drug dobutamine, which by increasing myocardial oxygen demands, also induces a hyperemic response.

^{111}In-tropolone is used routinely to label white blood cells for imaging inflammation [23]. The ^{111}In radionuclide has a radioactive half-life of 2.82 days and emits gamma rays at both 173keV and 247keV. The relatively long half life of ^{111}In makes it useful for tracking cells over days or even weeks [24]. ^{111}In-tropolone labels cells by first diffusing freely across the cell membrane. Once inside the cell, cytosolic proteins bind the radiolabel, thus radiolabeling the cell from the inside.

In the end, the ^{99m}Tc SPECT image shows cardiac perfusion, and the ^{111}In SPECT the transplanted cells location within the heart and also their relationship to the area of reduced perfusion. This information is potentially useful to evaluate the accuracy of

transplantation, monitor the migration pattern of the cells, infer viability of the transplanted cells, or monitor the size of the underlying infarct.

1.2.1 Radiation dose from ^{99m}Tc and ^{111}In

Research has demonstrated that, in the process of labeling, the radiation dose per cell cannot exceed certain levels depending on the type of cell since toxicity analysis has shown that higher levels of radiation can cause cell death [25]. To determine the whole body dose that one would receive from labeled cells transplanted in the myocardium, one can use the typical dose of ^{111}In-tropolone for labeling white blood cells as part of a clinically performed inflammation study as a comparison. Labeled white blood cells would provide a whole body equivalent dose of 7mSv [26]. The whole body radiation exposure dose for a patient undergoing a rest/stress protocol is approximately 12.5mSv [26]. However, for stem cell labeling we would be using a tenth of the ^{111}In dose to label the cells reducing the whole body exposure dose to less than 1mSv.

1.3 SPECT DATA ACQUISITION

Data in SPECT are acquired using a Gamma Camera. A typical gamma camera consists of a collimator, a scintillation crystal, photomultiplier tubes, and positioning electronics. The role of the collimator is to act as a 'lens' for the imaging system by rejecting gamma rays with undesirable trajectories. In the case of a parallel-hole collimator, which was used in all of our experiments, the holes are parallel to each other and perpendicular to the plane of imaging. This configuration passes only gamma rays that are approximately perpendicular to the imaging plane and hence useful for image

formation. The gamma rays that pass through the collimator impinge onto the scintillation crystal, which converts them into light. Currently, the most popular choice of scintillation crystal in SPECT is thallium-doped sodium iodide – NaI(Tl). The photomultiplier tubes convert the light from the scintillation crystal into an electrical signal, via the photoelectric effect, and amplify the signal using a series of dynodes. The amplified electrical signal is then passed through circuits that combine signals from adjacent photomultiplier tubes to determine the position of the original gamma ray's interaction with the scintillation crystal. These locations are transferred to a computer that tabulates successive gamma ray detection events into a two-dimensional array, which is a projection of the radioactive distribution. In SPECT, these projections are acquired at multiple angles around the patient. After data acquisition is complete, these projections are used to reconstruct three-dimensional tomographic images of the original distribution of radioisotope inside the patient.

Making SPECT quantitative is not straightforward. Three physical phenomena that are central to interfering with quantitative SPECT are: photon attenuation, photon scatter and distance-dependent resolution [27].

In an ideal SPECT imaging scenario all gamma rays emitted by the radioactively decaying radionuclides would escape the body and be available for detection by a gamma camera. In a realistic scenario, however, gamma rays pass through many layers of tissue and often interact with that tissue prior to exiting the body. In this interaction, gamma-rays can be either absorbed photoelectrically, or scattered from their original trajectory potentially away from the gamma camera [28]. Either way, they may not reach the gamma camera. The amount and extent of attenuation is dependent on the gamma ray

energy, the thickness of tissue the gamma ray has to pass through as well as the composition of the tissue, since bone will attenuate more per unit path length than softer tissues such as fat and muscle [29, 30].

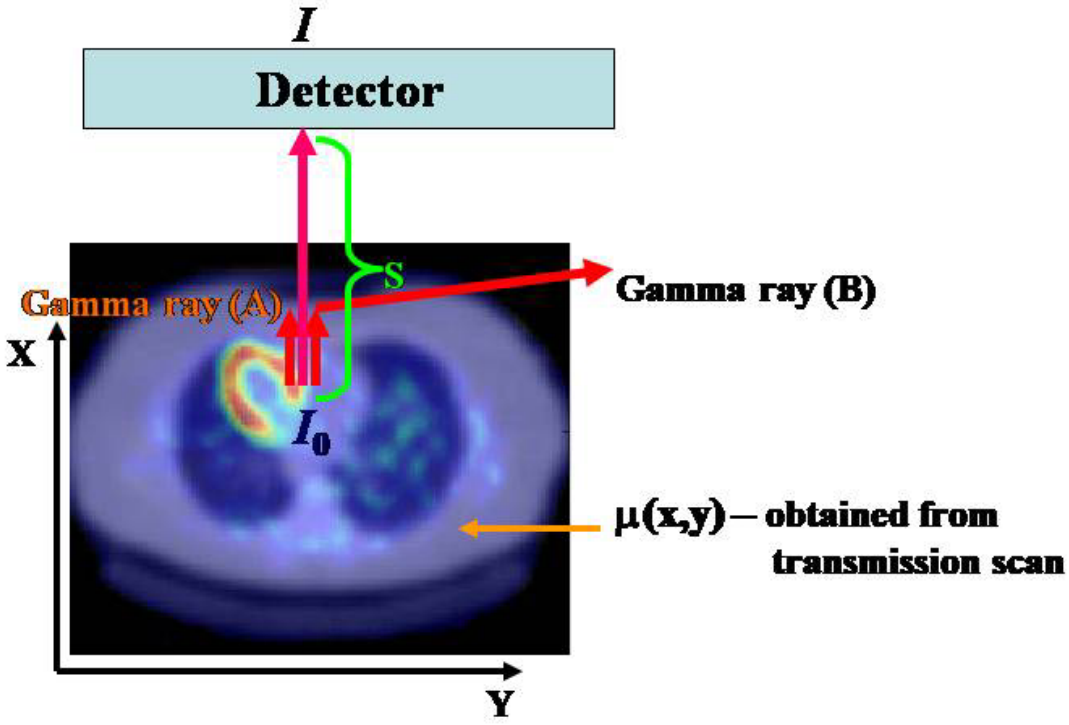

Figure 1.1: Attenuation

Figure displaying a radioactive distribution inside a patient with initial intensity I_0. When the gamma ray travels through the patient, it will experience attenuation through either photoelectric absorption (gamma ray A), or scattering (gamma ray B).

The gamma rays that are measured by the detector will have a measured intensity value of I. μ is the linear attenuation coefficient of the object and is dependent on its composition, and S is the path the gamma ray travels before reaching the detector (figure 1.1). These are related through the following equation for attenuation [28]:

$$I = I_o e^{-\int_S \mu(x,y)ds} \quad (1.1)$$

$\boldsymbol{I_0}$ = reference intensity
I = measured intensity
S = Path taken by gamma ray
μ(x,y) = linear attenuation coefficient as a function of location in tissue
ds = differential of the tissue thickness encountered along path S

Scatter can also be defined as the detection of mis-positioned gamma rays. The presence of scatter in SPECT imaging generally degrades image contrast and compromises quantitative accuracy. In SPECT, gamma rays can become mis-positioned through the physical phenomenon of Compton scattering. In Compton scattering, a gamma ray emitting from a decaying radionuclide is deflected from its original trajectory but is detected anyway. Fortunately, since the energy of Compton scattered gamma rays are different from those of primary gamma rays, they may be distinguishable through energy discrimination. Thus, the energy of each gamma ray is measured as it is detected. If that gamma ray's energy falls outside a pre-set tolerance – commonly referred to as an energy 'window' – then that gamma ray can be rejected. A common window for clinical SPECT using ^{99m}Tc is 140 keV +/-7.5%. However, scatter rejection by energy discrimination is not perfect: in clinical SPECT imaging, a 140 keV +/-7.5% energy window contains approximately 1/3 scattered gamma rays [31]. Reducing this scatter is the subject of extensive research, and is described in section 1.6.

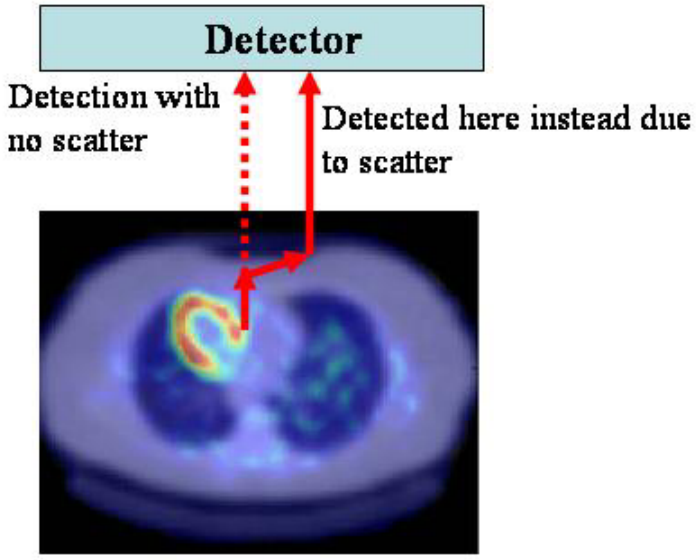

Figure 1.2: Scatter

Figure displaying the effect of scatter that occurs within an object. Gamma rays that should have been detected at a certain location are detected elsewhere due to the scatter interaction.

A third important source of image quality degradation is the loss of spatial resolution due to the physical collimator on a gamma camera and the intrinsic spatial resolution of the detection crystal. The collimator consists of a series of holes separated by septa, made from a material with high atomic number, such as lead. Typically, the holes are hexagonal in shape and arranged into a honeycomb (see figure 1.3).

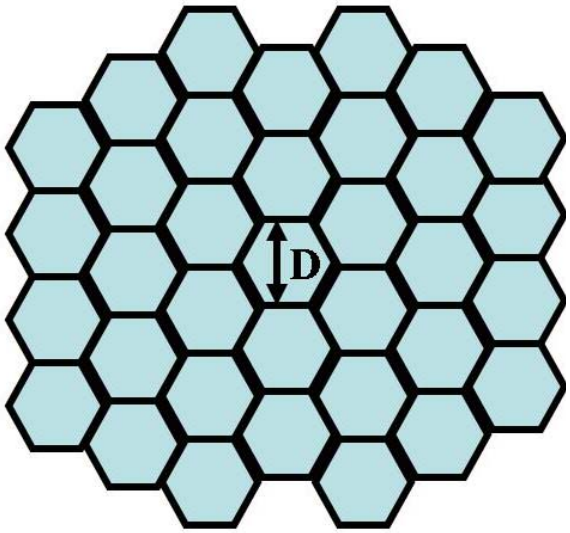

Figure 1.3: Collimator holes

Figure displaying the hexagonal holes of the collimator arranged in a honeycomb pattern. The number of holes typically range from 10000 to 150000. The hole diameter (D) can range from 1 mm to 3 mm

As stated previously, the purpose of the collimator is to admit gamma rays traveling in a preferred direction (i.e. perpendicular) relative to the imaging plane, and reject other gamma rays. In practice, however, collimators admit gamma rays with a small angular deviation away from the perpendicular imaging plane. The geometry of this 'acceptance angle' strongly influences spatial resolution on the imaging plane (see figure 1.4). In fact, the spatial resolution on the image becomes a function of the distance between the source of gamma rays and the collimator [30]. This phenomenon is referred to as distance-dependent resolution. The acceptance angle can be reduced by making the collimators holes smaller in diameter or increasing the length of the septa (figure 1.4), leading to improvements in spatial resolution. However, the trade-off to reducing the

acceptance angle is a decrease in sensitivity, leading to increases in image noise due to the decrease in signal. The following equation can be used to relate the distance-dependent resolution (figure 1.4):

$$R = D \cdot \tan(\Phi) \tag{1.2}$$

Where R = Resolution
D = Distance from point source to crystal
Φ = Acceptance angle

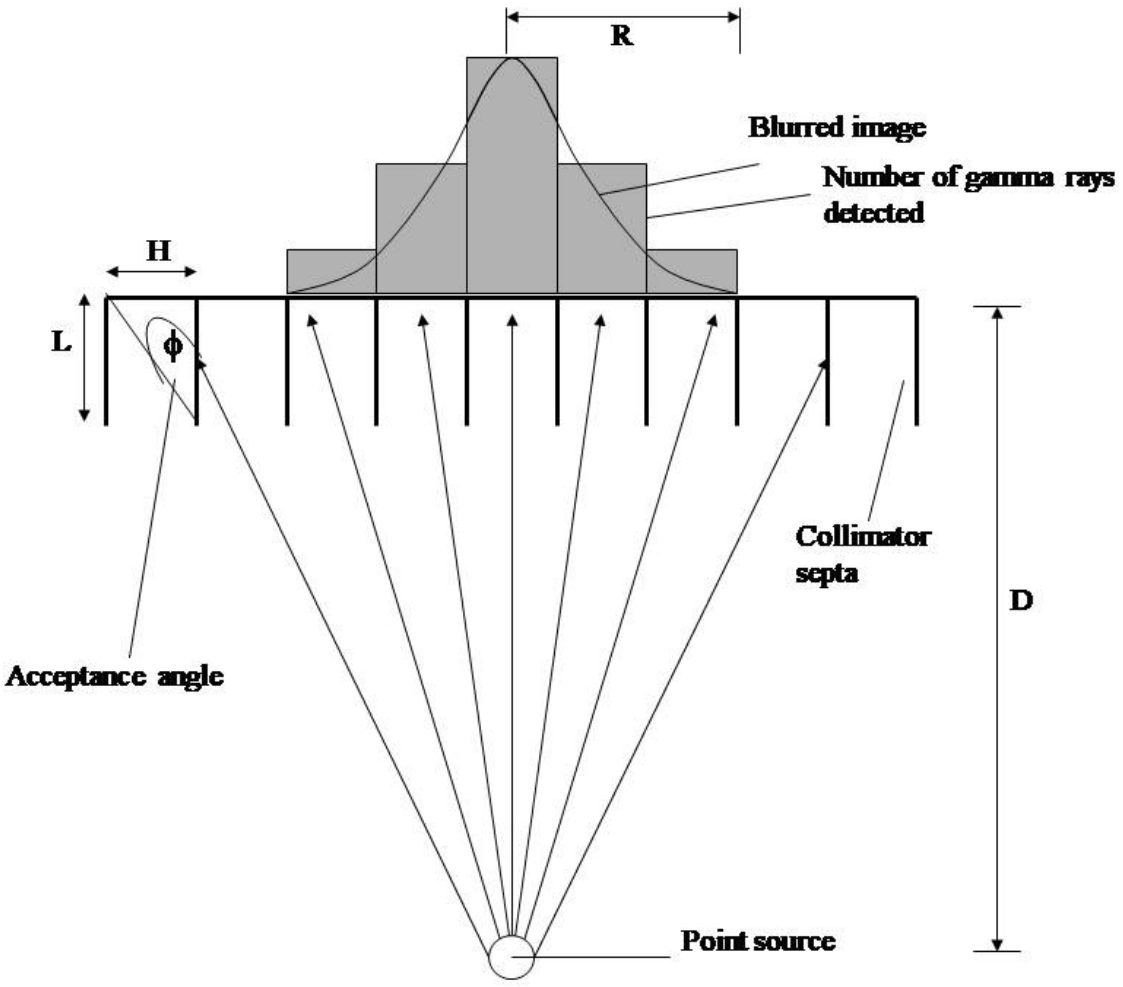

Figure 1.4: Distance-dependant blurring

This figure demonstrates how a radioactive point source is blurred due to the acceptance angle of a parallel hole geometry collimator. D is the distance from the point source to the crystal, H is the hole diameter of the septa, while L is the length.

1.4 TOMOGRAPHIC RECONSTRUCTIONS IN SPECT

Many algorithms have been developed for tomographic reconstruction from projection data. Up until the past decade, the most popular algorithm was filtered back-projection, which was adapted from X-ray Computed Tomography [32]. Although

computationally efficient, filtered back-projection did not allow the reconstruction of quantitative images in SPECT. This was due primarily to the inability to incorporate the physics of gamma ray propagation into the filtered back-projection algorithm, and to a lesser extent, the inaccurate modeling of Poisson noise in gamma ray detection [33]. Today, filtered back-projection has been replaced extensively with iterative reconstruction. Although much more computationally demanding, iterative reconstruction can incorporate gamma ray attenuation, Compton scatter, and distance-dependent resolution effects, as well as modeling noise properly [34].

We provide a brief introduction to iterative reconstruction. The reader is referred to [35] for a detailed review. First, we consider the process of measuring a distribution of radioactivity using a gamma camera. Let the vector **F**, with size M×1 and elements $f_1 \ldots f_M$, be a discretized representation of the distribution of radioactive disintegrations in a region that we are interested in measuring. The elements of **F** represent the individual volume elements, or voxels, of the object. Let the vector **G**, with size N×1 and elements $g_1 \ldots g_N$, represent the pixel-by-pixel measurements of the radioactivity as recorded by a gamma camera as it rotates around the source of radioactivity – the elements of a sinogram. Thus **G** would be a measure of the projection of **F**. This can be written mathematically as:

$$G = AF \tag{1.3}$$

Where A is an N×M matrix. Each element in A, corresponds to the probability that the gamma ray emitted in a particular voxel is detected by a particular pixel at a particular gamma camera position (during its rotation around the radioactive source). For example, elements in A represent the probability that voxel f_i emits gamma rays that are recorded

by the gamma camera in pixel g_j. Equation (1.3) is commonly referred to as the forward projection, and A the transition matrix. The attractiveness of iterative reconstruction lies in the flexibility of the transition matrix. The transition matrix can include extremely detailed models of the physics of both photon propagation in non-uniform media and detection with a gamma camera. Various groups have developed methods to include attenuation effects using radioisotope transmission images [36, 37] or X-ray CT [38, 39, 40] or even MRI [41]. Incorporation of Compton scatter, although more computationally demanding, has received considerable attention [42, 43], as has distance-dependent resolution effects [44].

One of the most popular iterative reconstruction algorithms is Maximum-Likelihood Expectation Maximization (MLEM), introduced to the nuclear medicine society by Shepp and Vardi [45], and Lange and Carson [46]. We provide a brief introduction to the algorithm, but the reader is referred to Lange and Carson [46] for a detailed derivation. The objective of tomographic reconstruction is to solve Equation (1.3) by finding the best estimate of **F**: the mean number of radioactive disintegrations in the measurement region that can produce the measurements **G** with the highest likelihood assuming Poisson statistics. The MLEM formula is designed to find this best estimate of F. It can be written as [46]:

$$f_m^{k+1} = \frac{f_m^k}{\sum_{n=1}^{N} a_{nm}} \sum_{n=1}^{N} \frac{g_n}{\sum_{m=1}^{M} a_{nm} f_m^k} a_{nm} \qquad (1.4)$$

Where f_m^{k+1} = new estimate

f_m^k = old estimate

g_n = measured number of counts

n = bin number

m = pixel number

k = iteration number

a_{nm} = probability photon emitted from m^{th} pixel will be detected in n^{th} bin

This equation seems complex at first presentation, but is simply a set of successive projection and back-projection operations. It can be expressed more simply in words [47]:

$$\text{Image}^{(k+1)} = \text{Image}^{(k)} \times \text{Normalized Backprojection of } \frac{\text{Measured Projections}}{\text{Projection of image}^{(k)}} \qquad (1.5)$$

The MLEM algorithm requires a starting estimate of the image to be reconstructed, referred to as F^0 in Equation (1.4) or Image^0 in Equation (1.5). This is often a uniform disk of the value 1. As the MLEM iterations proceed, the image gradually converges to the tomographic representation of the original distribution of radioactivity that was measured. My research utilized a modified version of MLEM known as Ordered Subsets Expectation Maximization (OSEM) [48]. Studies have shown that OSEM converges to a useful image faster than MLEM, and so it is sometimes termed an accelerated version of MLEM. Similar equations and process previously described are used by both algorithms, but are implemented differently. For the case of

MLEM a projection/back-projection calculation must be done for every projection angle before an updated estimate can be generated. In OSEM, only a portion of the projection angles are projected and back-projected for each iteration. Successive iterations utilize different subsets, gradually stepping through all projection angles.

Attenuation, scatter, and distant-dependent resolution are important forms of image degradation. For the purpose of this thesis we will discuss methods to compensate for all these physical effects, but will concentrate more on attenuation correction since this thesis' primary focus is on methods of attenuation correction.

1.5 CORRECTING FOR ATTENUATION IN SPECT

To correct for the effects of attenuation the distribution of electron density must be determined in the object being imaged. Two popular methods for measuring density include radioisotope transmission imaging [37], and more recently X-ray Computed Tomopgraphy – leading to the so-called Hybrid SPECT/CT [38]. The technique of radioisotope transmission imaging placed a gamma-ray emitting radioisotope adjacent to the patient but opposite to the gamma camera, as shown in figure 1.5. The gamma camera would record the passage of gamma rays through the patient, and then repeat that measurement without the patient. By comparing the two measurements and by using the principles of computed tomography, one could calculate the distribution of attenuation inside the patient's body [49]. The advantages of radioisotope transmission imaging are a large field of view and a relatively small radiation burden. Perisinakis et. al. [50] report that for a ^{153}Gd radioisotope source, the radiation dose would be approximately 3.2 μSv, and since both transmission and emission could be performed simultaneously (with some

implementations) there would be only minimal probability of mis-registration between the patient's SPECT scan and their attenuation map [37]. Some disadvantages include the requirement of high activity radioisotope source, and the final attenuation maps tended to have poor spatial resolution and considerable noise [49].

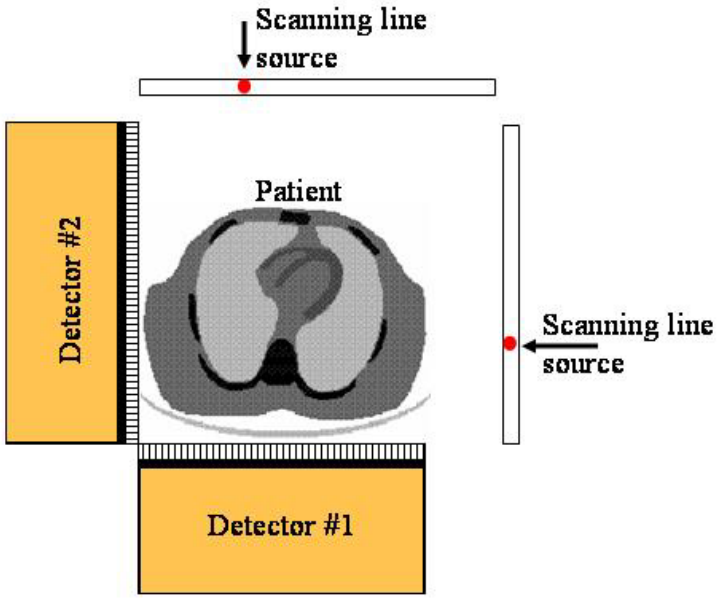

Figure 1.5: Transmission imaging with a scanning line source

Figure displaying a dual detector SPECT camera with a scanning line source transmission imaging system.

Over the past decade, radiosotope transmission imaging was gradually replaced with X-ray Computed Tomography (a concept first proposed by Hasegawa [51]), bringing about the hybrid SPECT/CT scanner. X-ray CT had several important advantages over radioisotope transmission imaging, including (i) images of sufficient resolution and low-noise to offer some diagnostic value, (ii) images acquired fast enough (depending on the implementation) to be relatively free of motion artifacts, and (iii) a

radiation source that could be de-activated and would not decay. Disadvantages include: the SPECT and CT are acquired sequentially providing the potential of mis-registration, and higher costs and radiation dose [49].

One chapter of this thesis examines two different SPECT/CT systems, where the two systems are differentiated primarily based on their CT rotational speed. One system utilizes a slow-rotation CT for acquiring the transmission data. In this scenario the X-ray tube and detector are attached to the gamma camera gantry, and therefore can only rotate as fast as the gamma camera gantry, which is approximately 15 seconds for a full 360^0 rotation. For each rotation four slices of data are acquired, with each slice being 5mm thick. Scanning a 10cm axial field-of-view therefore requires approximately 5 minutes. This period of time is too long for a patient to hold their breath, thus patients are freely breathing during data acquisition. Although these images are subject to respiratory motion, they still have a much better spatial resolution than those acquired via radioisotope transmission imaging. Although the images are not of diagnostic quality, some studies have shown that for attenuation correction an image of diagnostic resolution is not required [52, 53]. In terms of ionizing radiation burden to the patient: for a rest/stress cardiac scan (which is a typical SPECT/CT application), two CT scans would be required for a combined dose of 0.5mSv [54]. Despite this dose being higher than from radioisiotope transmission imaging (few micro Sieverts [50]) it still compares favourably relative to the dose attributed to the injected radiotracer – which is approximately 12.5mSv [26].

A second SPECT/CT design features a SPECT scanner coupled to a high-speed CT capable of producing images of diagnostic quality. A typical 360^o rotation speed for

such a system is 0.6 seconds, while acquiring between 6 to 64 slices per rotation. This high speed enables a CT acquisition within a single breath-hold, which eliminate motion artifacts related to breathing, and therefore yields a higher contrast image. The improved image quality however, is associated with increased ionizing radiation dose: the CT portion of a cardiac rest/stress scan will contribute 2-4mSv of radiation burden to the patient [55].

1.6 CORRECTING FOR SCATTERED GAMMA RAYS IN SPECT

In SPECT imaging, the gamma ray detects both primary gamma rays as well as scattered gamma rays. One method of reducing scatter content is to reject scattered gamma rays via energy discrimination. Currently, this is employed by all gamma cameras, as previously described. For example ^{99m}Tc imaging is frequently acquired using an energy window centered at 140 keV, with a 15% width. Gamma rays with energies outside that range are rejected – but low-angle scatter is still admitted. In principle one could further remove scatter rejection by reducing the width of the energy acceptance. Unfortunately this width is ultimately limited by the finite energy resolution of the gamma camera, which is approximately 10%. In an effort to improve energy resolution, recent efforts have focused on solid state detectors which replace both the scintillation crystal and photomultiplier tubes found in conventional gamma cameras . Solid-state detectors using either Cadmium Zinc Telluride (CZT) or Cadmium Telluride (CdTe) are currently being studied [56]. Early indications have demonstrated that these materials could improve the energy resolution to approximately 5% -- a substantial improvement over conventional gamma cameras [57, 58, 59].

Despite the use of energy discrimination, some scattered gamma rays cannot be differentiated from primary gamma rays and thus end up being included during data acquisition. The presence of scatter in SPECT degrades resolution and image contrast, and therefore it is desirable to minimize its presence. A popular method of scatter correction used clinically is to acquire projection data from energy windows adjacent to the photopeak window, and use this data to estimate the distribution of scatter in the photopeak energy window. In ^{99m}Tc radioisotope imaging (which represents the majority of SPECT imaging), a typical scatter correction is the "dual-energy" scatter correction method first presented by Jaszczak et al [60] and later refined by Ogawa et al [61], illustrated in figure 1.6. This scatter correction method assumes that the spatial distribution of scattered gamma rays in the photopeak energy window is the same as all gamma rays recorded in the adjacent (lower energy) window. The scatter correction is effected by scaling the data recorded in the adjacent energy window by an experimentally-determined constant and then subtracting that scaled data from the data measured in the photopeak energy window. After the scattered gamma rays are removed from the photopeak projection data, the 'corrected' measurements are processed for tomographic reconstruction. For the case of radio-isotopes that have two energy peaks, which is the case of ^{111}In, down-scatter is present at the photo-peak centered at 173keV coming from the higher photo-peak centered at 247keV. In this situation a triple-energy window (TEW) scatter correction method is used by placing one scatter window just below and one just above the primary window around 173keV (figure 1.6) [62].

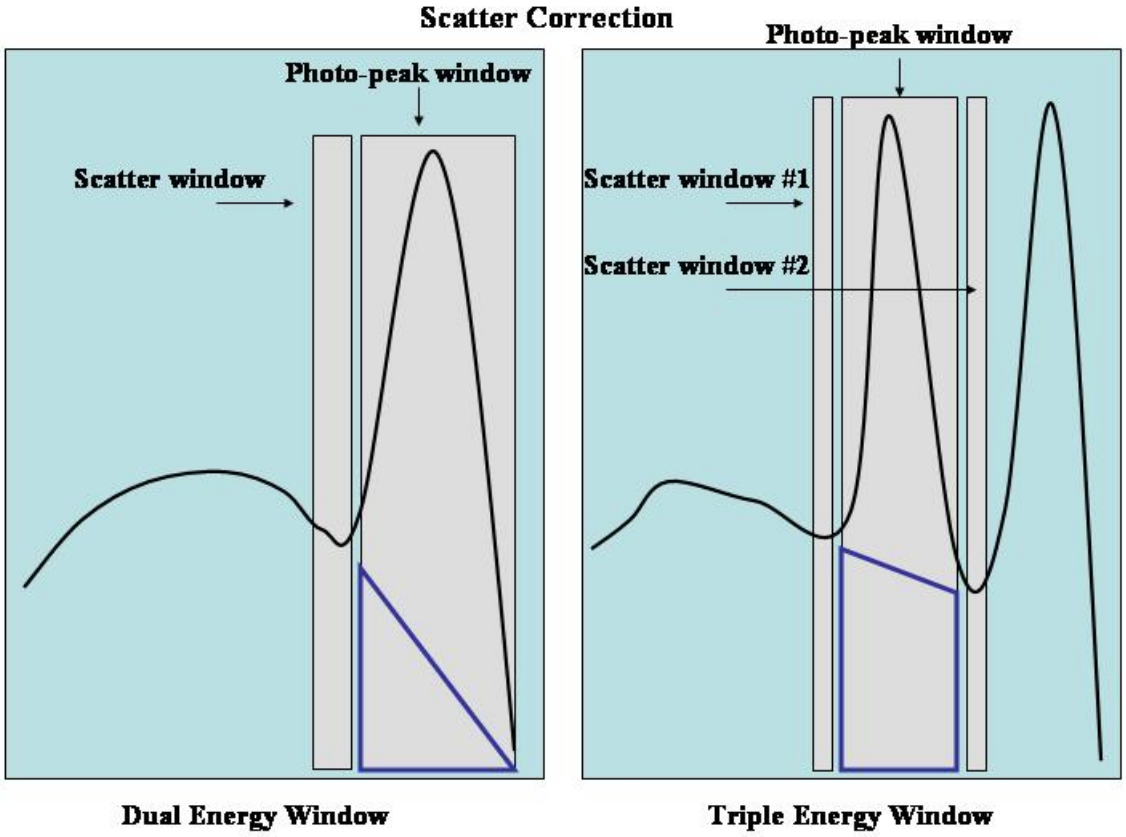

Figure 1.6: Scatter correction techniques

For ^{99m}Tc imaging and "dual energy" scatter correction a narrow window just below the photopeak window is chosen. With this scatter window a triangle is made, with the height equivalent to the average number of counts measured in the scatter window, and the base being the width of the primary window. The area under this triangle is an estimate of the scatter measured in the photopeak window. Scatter correction is then implemented by subtracting this scatter estimate from the counts in the photopeak window. For ^{111}In imaging and TEW scatter correction a trapezoid is formed with the scatter windows above and below the photopeak window, with the base being the width of the photopeak window, and the area under the trapezoid would be subtracted from the photopeak window to correct for scatter.

1.7 CORRECTING FOR DISTANCE-DEPENDENT RESOLUTION IN SPECT

The detector and collimator response functions can be measured and incorporated into the iterative reconstruction algorithm to compensate for the distance-dependent resolution [63]. To measure the detector response function the collimator is removed and a lead plate consisting of a narrow slit is placed on the NaI(Tl) crystal and is irradiated with a radioactive source. The FWHM of this slit is then measured and is typically calculated to be approximately 4.0mm. It should be noted that the detector response is not dependent on distance. The collimator response function is however distance-dependent (as discussed in Section 1.3), and can be measured with a line source of activity placed at different distances from the collimator. The line profile of the activity source is measured at different distances and fit to a Gaussian function and the FWHM is measured. The FWHM of the detector and collimator response functions are then combined and plotted to fit a line. This data is then incorporated into the transfer function of the iterative reconstruction algorithm to correct for distance-dependent blurring in a SPECT image.

1.8 TOWARDS THE MONITORING OF CARDIAC STEM CELL THERAPY USING SPECT/CT

My thesis explores several technical challenges associated with the use of SPECT/CT in monitoring cardiac regenerative therapy. This first aspect concerns the adoption of solid-state gamma cameras, which is inevitable if their costs continue to decrease.

Since stem cells are sensitive to radiation dose, it is desirable to label them with as little radioisotope as possible. Our group has performed studies to determine the toxicity levels acceptable for cells to continue to proliferate, which was shown to be 0.1 Bq of ^{111}In per cell, for the case of bone marrow derived mesenchymal stem cells [25]. In our studies involving canine models of heart disease, we would aim to transplant approximately 30 million cells [64]. Thus, at most, the activity transplanted to a target site (such as an infarction) would be 3 MBq. This activity level is much lower than the 20 to 30MBq of ^{111}In used to label white blood cells in routine clinical applications. In addition, these cells are widely dispersed throughout the whole body, as opposed to the limited geographic distribution of the transplanted stem cells. With such a limited amount of radioactivity, greater attention must be paid to maximizing image quality including the implementation of corrections for the physical effects of gamma ray attenuation and scatter. One opportunity for minimizing the presence of scatter in SPECT may lie with the adoption of solid-state gamma cameras. Compared with conventional gammas cameras utilizing scintillation crystals and photomultiplier tubes, solid-state detectors can achieve superior energy and spatial resolution, in addition to enhanced image contrast [56]– all of which would benefit imaging transplanted radiolabeled cells. The use of solid-state gamma cameras is currently limited due to very high manufacturing costs, especially for large field-of-view (FOV) detectors. For the application of monitoring cardiac stem cell therapy, however, a large FOV detector may not be necessary since the region of interest – the heart – is relatively small. However, in general, the use of small detectors requires caution since object truncation always becomes more of a concern [65, 66]. However no one has addressed the problems of

image truncation when performing hot-spot imaging. It will be shown that provided the hot-spot is within each projection that truncation is less of a problem if the reconstruction method is guided by an anatomical imaging method such as CT.

When imaging radioactive distributions larger than the gamma camera, artifacts caused by object truncation can appear at the periphery of the FOV. These artifacts can be especially prominent in iterative reconstructions, and are the result of the reconstruction algorithm attempting to find a distribution of activity in that FOV most consistent with the projection data (as described in Section 1.4 earlier). However, since there is by definition, radioactivity beyond the FOV, the algorithm converges to an incorrect solution; and the error is seen as the "hot rim" truncation artifact.

Correcting for truncation artifacts is important when imaging a small FOV because the artifact can easily interfere with the imaging of the object of interest. Methods for correcting image truncation have been discussed in the past [66, 67]. In CHAPTER 4, I evaluate an iterative reconstruction algorithm modified to reduce the presence of truncation artifacts. The algorithm is evaluated in the context of cardiac imaging where the imaging apparatus is a small FOV gamma camera coupled to a large FOV X-ray CT.

The low amount of activity used in cardiac stem cell therapy monitoring using SPECT emphasizes the need for dealing with the physical effects of scatter and attenuation. The previous section introduced the necessity for improved scatter rejection; however, the matter of gamma-ray attenuation will also need to be addressed. Currently the most widely implemented method for attenuation correction is via X-ray CT. However, as previously described, two CT designs exist for SPECT/CT systems; a slow-

rotation CT and a fast-rotation CT. We should note a third CT design exists that incorporates a flat panel x-ray detector that can image the entire chest in a single rotation. At the time of the experiments the flat panel design was not available and therefore the latter two were studied. Experiments were required to determine which design will perform a more correct method of attenuation correction. In Chapter 2, I study how respiratory motion impacts the quality of cardiac SPECT imaging when attenuation correction is based on fast vs slow rotation CT. I evaluate both designs using computer simulations and experiments in a canine model.

Many aspects of cardiac stem cell therapy remain to be studied and optimized. To achieve successful cell therapy, it is believed that cells should be transplanted into the periphery of the infarct, and not directly in the infarct center where blood flow is compromised [68]. Therefore, methods to properly localize transplanted cells in relation to blood flow must be developed. Here, SPECT can offer a solution due to its multi-spectral imaging capabilities. We previously demonstrated the ability of SPECT to image simultaneously, in a canine model, cardiac-transplanted ^{111}In-labeled cells, myocardial perfusion using ^{99m}Tc-MIBI, and an ^{131}I-labeled FIAU reporter probe (See Figure 1.7). However, the resolution of the SPECT blood flow image with ^{99m}Tc is not ideal to properly localize the cells relative to the region of reduced blood flow. CT has been shown to be a viable alternative for perfusion imaging [69, 70], and has the resolution required to localize the ^{111}In labeled cells seen on SPECT. Recent studies have confirmed that the CT in hybrid systems such as PET/CT can be used for perfusion imaging [71]. In Chapter 3, I demonstrate a newly developed method of combining

SPECT with first-pass perfusion CT for the localization of cells in relation to region of reduced blood flow in a canine model of myocardial infarction.

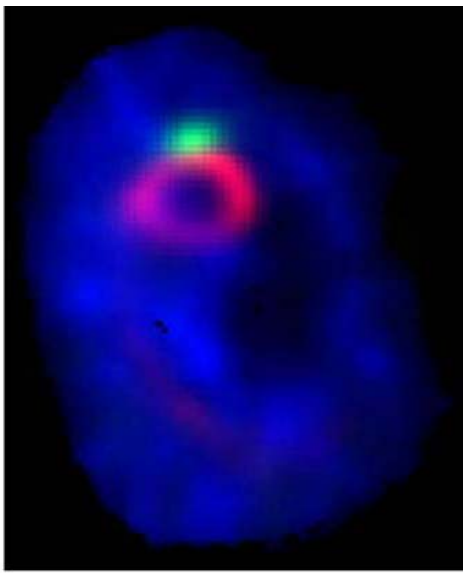

Figure 1.7: Multi-spectral imaging using SPECT

SPECT is capable of imaging multiple isotopes simultaneously. In this particular example of a canine study, the injected cells were labeled with ^{111}In (GREEN), the cardiac perfusion image was obtained with ^{99m}Tc (RED), and a reporter probe imaged with ^{131}I (BLUE). All of these isotopes are combined to form a single image.

1.9 REFERENCES

1. Bloom BR. Public health in transition. *Scientific American.* 2005 Sept;293(3):92-99.

2. Pfeffer MA, Braunwald E. Ventricular remodelling after myocardial infarction. *Circulation.* 1990;81:1161-1172.

3. Blackwood KJ, Sabondjian E, Goldhawk DE, Kovacs MS, Wisenberg G, Merrifield P, Prato FS, DeMoor JM, Stodilka RZ. Progress in Stem Cell Applications. *Chapter V: Towards Image-Guided Stem Cell Therapy.* 2008 Nova Biomedical books; New York. 153:180.

4. Kones R. Recent advances in the management of chronic stable angina II. Anti-ischemic therapy, options for refractory angina, risk factor reduction, and revascularization *Vasc Health Risk Manag*. 2010;6:749–774.

5. Wollert KC, Drexler H. Clinical applications of stem cells for the heart. *Circ Res*. 2005;96:151-163.

6. Orlic D, Kajstura J, Chimenti S, Jakoniuk I, Anderson SM, Li B, et al. Bone marrow cells regenerate infracted myocardium. *Nature.* 2001;410(6829):701-705.

7. Lunde K, Solheim S, Aakhus S, Arnesen H, Abdelnoor M, Egeland T, et al. Intracoronary injection of mononuclear bone marrow cells in acute myocardial infarction. *N Eng J Med.* 2006;355(12):1199-1209.

8. Meyer GP, Wollert KC, Lotz J, Steffens J, Lippolt P, Fichtner S, et al. Intracoronary bone marrow cell transfer after myocardial infarction: eighteen months' follow-up data from the randomized, controlled BOOST (Bone marrow transfer to enhance ST-elevation infarct regeneration) trial. *Circulation.* 2006;113(10):1287-1294.

9. Schachinger V, Erbs S, Elsasser A, Haberbosch W, Hambrecht R, Holschermann H, et al. REPAIR-AMI Investigators. Intracoronary bone marrow-derived progenitor cells in acute myocardial infarction. *N Eng J Med.* 2006;355(12):1210-1221.

10. Beeres SLMA, Bengel FM, Bartunek J, Atsma DE, Hill JM, Vanderheyden M, et al. Role of imaging in cardiac stem cell therapy. *JACC*. 2007;49(11):1137-1148.

11. Zhou R, Acton PD, Ferrari VA. Imaging stem cells implanted in infarcted myocardium. *JACC.* 2006;48(10):2094-2106.

12. Diesbourg LD, Prato FS, Wisenberg G, Drost DJ, Marshall TP, Carroll SE, et al. Quantification of myocardial blood flow and extracellular volumes using a bolus injection of Gd-DTPA: kinetic modeling in canine ischemic disease. *Magn Reson Med.* 1992;23(2):239-253.

13. Kim RJ, Wu E, Rafael A, Chen EL, Parker MA, Simonetti O, et al. The use of contrast-enhanced magnetic resonance imaging to identify reversible myocardial dysfunction. *N Engl J Med* 2000 Nov;343(20):1445-1453.

14. Hinds KA, Hill JM, Shapiro EM, Laukkanen MO, Silva AC, Combs CA, et al. Highly efficient endosomal labeling of progenitor and stem cells with large magnetic particles allows magnetic resonance imaging of single cells. *Blood* 2003;102:867-872.

15. Kraitchman DL, Heldman AW, Atalar E, Amado LC, Martin BJ, Pittenger MF, et al. In vivo magnetic resonance imaging of mesenchymal stem cells in myocardial infarction. *Circulation* 2003;107:2290-2293.

16. Chen IY, Greve JM, Gheysens O, Willmann JK, Rodriguez-Porcel M, Chu P, et al. Comparison of optical bioluminescence reporter gene and superparamagnetic iron oxide MR contrast agent as cell markers for noninvasive imaging of cardiac cell transplantation. *Mol Imaging Biol.* 2009 May-Jun;11(3):178-87.

17. Hofmann M, Wollert KC, Meyer GP, Menke A, Arseniev L, Hertenstein B, et al. Monitoring of bone marrow cell homing into the infarcted human myocardium. *Circulation* 2005;111:2198-2202.

18. Huang J, Lee CCI, Sutcliffe JL, Cherry SR, Tarantal AF. Radiolabeling rhesus monkey $CD34^{+}$ hematopoietic and mesenchymal stem cells with ^{64}Cu-Pyruvaldehyde-Bis(N4-Methylthiosemicarbazone) for microPET imaging. *Mol Imaging* 2008;7(1):1-11.

19. Gamsu G, Patel MD. Diagnostic Imaging Review. 2008 W.B. Saunders Company

20. Goedemans W, de Jong M. Comparison of Several Indium-111 Ligands in Labeling Blood Cells: Effect of Diethylpyrocarbonate and CO2. *J Nucl Med* 1987;28:1020-1026.

21. Jain D. Technetium-99m labeled myocardial perfusion imaging agents. *Semin Nucl Med.* 1999;29:221-236.

22. Ravizzini GC, Hanson MW, Shaw LK, Wong TZ, Hagge RJ, Pagnanelli RA, Jain D, Lima Jr HS, Coleman RE, Borges-Neto S. Efficiency comparison between Tc-99m-Tetrofosmin and Tc-99m-sestamibi myocardial perfusion studies. *Nucl Med Comm* 2002;23:203-208.

23. Becker W, Meller J. The role of nuclear medicine in infection and inflammation. *Lancet Infect Dis* 2001;1:326–33.

24. Blackwood KJ, Lewden B, Wells RG, Sykes J, Stodilka RZ, Wisenberg G, Prato FS. In vivo SPECT quantification of transplanted cell survival following engraftment using 111In-tropolone in infarcted canine myocardium. *J Nucl Med* 2009;50(6):927-935.

25. Jin Y, Kong H, Stodilka RZ, Wells RG, Zabel P, Merrifield PA, et al. Determining the minimum number of detectable cardiac-transplanted 111In-tropolone-labelled bone-marrow-derived mesenchymal stem cells by SPECT. *Phys Med Biol* 2005;50(19):4445-4455.

26. Radiation dose to patients from radiopharmaceuticals. *Annals of the ICRP. ICRP Publication 80.* 1998;28(3):113-120.

27. King MA, Glick SJ, Pretorius PH, Wells RG, Gifford HC, Narayanan MV, Farncombe T. Attenuation, scatter and spatial resolution compensation in SPECT. In: Wernick MN, Aarsvold JN, eds. *Emission Tomography: The Fundamentals of SPECT and PET*. 1st ed. San Diego, CA: Elsevier; 2004:473–498.

28. Zaidi H, Hasegawa B. Determination of the attenuation map in emission tomography. *J Nucl Med.* 2003;44:291-315.

29. Batemen TM, Cullom SJ. Attenuation correction single-photon emission computed tomography myocardial perfusion imaging. *Semin Nucl Med* 2005;35:37-51.

30. Cherry SR, Sorenson JA, Phelps ME. Physics in Nuclear Medicine 3rd edition. *Saunders.* 2003 Philadelphia.

31. de Vries DJ, King MA, Window selection for dual photopeak window scatter correction in Tc-99m imaging. *IEEE TNS.* 1994;30:1179-1186.

32. Morano GN, Seibyl JP. Technical overview of brain SPECT imaging: improving acquisition and processing of data. *J Nucl Med Technol.* 2003;31(4):191-195.

33. Bouwens L, Van de Walle R, Nuyts J, Koole M, D'Asseler Y, Vandenberghe S, Lemahieu I, Dierckx RA. Image-correction techniques in SPECT**.** *Comput Med Imaging Graph.* 2001 Mar-Apr;25(2):117-126.

34. Wilson DW, Tsui BMW. Noise properties of filtered-backprojection and ML-EM reconstructed emission tomographic images. *IEEE TNS.* 1993;40(4):1198-1203.

35. Vandenberghe S, Asseler YD, de Walle RV. Kauppinen T, Koole M, Bouwens L, Laere KV, Lemahieu I, Dierckx RA. Iterative reconstruction algorithms in nuclear medicine. *Computerized medical imaging and graphics.* 2001;25:105-111.

36. Laere KV, Koole M, Kauppinen T, Monsieurs M, Bouwens L, Dierck R. Nonuniform transmission in brain SPECT using ^{201}Tl, ^{153}Gd, and ^{99m}Tc static line sources: anthropomorphic dosimetry studies and influence on brain quantification. *J Nucl Med.* 2000;41:2051-2062.

37. Du Raan H, du Toit PD, van Aswegen A, Lotter MG, Herbst CP. Implementation of a Tc-99m and Ce-139 scanning line source for attenuation correction in SPECT using a dual opposing detector scintillation camera. *Med Phys.* 2000;27(7):1523-1534.

38. Patton JA, Turkington TG. SPECT/CT physical principles and attenuation correction. *J Nucl Med Technol.* 2008;36:1-10.

39. Kalki K, Blankespoor SC, Brown JK, Hasegawa BH, Dae MW, Chin M. Myocardial perfusion imaging with a combined x-ray CT and SPECT system. *J Nucl Med.* 1997;38:1535-1540.

40. Gruning T. Brogsitter C, Khonsari M, Jones IW, Ormsby PL, Burchert W. X-ray-based attenuation correction of myocardial perfusion scans: practical feasibility and diagnostic impact. *Nucl Med Commun.* 2006;27:853-858.

41. Delso G, Martinez-Möller A, Bundschuh RA, Ladebeck R, Candidus Y, Faul D, Ziegler SI. Evaluation of the attenuation properties of MR equipment for its use in a whole-body PET/MR scanner. *Phys Med Biol.* 2010;55(15):4361-74.

42. Kadrmas DJ, Frey EC, Tsui BMW. Analysis of the reconstructibility and noise properties of scattered photons in ^{99m}Tc SPECT. *Phys Med Biol.* 1997;42:2493-2516.

43. Liu Z, Obi T, Yamaguchi M, Ohyama N. Modeling scatter in multiple energy windows to incorporate scattered radiation information in single photon emission computed tomography imaging. *Optical Review.* 1999;6(1):49-56.

44. Munley MT, Floyd CE jr, Bowsher JE, Coleman RE. An artificial neural network approach to quantitative single photon emission computed tomographic reconstruction with collimator, attenuation, and scatter compensation. *Med Phys.* 1994;21(12):1889-1899.

45. Shepp LA, Vardi Y. Maximum likelihood reconstruction for emission tomography. *IEEE TMI.* 1982;MI-1(2):113-122.

46. Lange K, carson R. EM reconstruction algorithms for emission and transmission tomography. *J Comput Assist Tomogr.* 1984;8(2):306-316.

47. Bruyant PP. Analytic and iterative reconstruction algorithms in SPECT. *J Nucl Med.* 2002;43:1343-1358.

48. Hudson HM, Larkin RS. Accelerated image reconstruction using ordered subsets of projection data. *IEEE TMI*. 1994;13(4):601–609.

49. Corbett JR, Kritzman JN, Ficaro EP. Attenuation correction for single photon emission computed tomography myocardial perfusion imaging. *Current Cardiology Reports.* 2004;6:32-40.

50. Perisinakis K, Theocharopoulos N, Karkavitsas N, Damilakis J. Patient effective radiation dose and associated risk from transmission scans using 153Gd line sources in cardiac spect studies. Health Phys. 2002;83(1):66-74.

51. Hasegawa BH, Iwata K, Wong KH, Wu MC, Da Silva AJ, Tang HR, Barber WC, Hwang AH, Sakdinawat AE. Dual-modality imaging of function and physiology. *Acad Radiol*. 2002;9(11):1305-21.

52. Hamann M, Aldridge M, Dickson J, Endozo R, Lozhkin K, Hutton BF. Evaluation of a low-dose / slow-rotation SPECT-CT system. *Phys Med Biol.* 2008;53:2495-2508.

53. Preuss R et al. Optimisation of protocol for low dose CT-derived attenuation correction in myocardial perfusion SPECT imaging *Eur. J. Nucl. Med. Mol. Imaging.* 2008;35**:**1133-1141.

54. Schillaci O. Hybrid SPECT/CT: a new era for SPECT imaging? *Eur J Nucl Med Mol Imaging.* 2005;32:521-524.

55. Bach-Gansmo T, Schwarzlmüller T, Jøraholmen V, Salbu J, Biermann M, Naum A, Kleven-Madsen N. SPECT/CT hybrid imaging; with which CT? *Contrast Media Mol. Imaging.* 2010;5(4):208-212.

56. Darambara DG, Todd-Pokropek A. Solid-state detectors in nuclear medicine. *Q J Nucl Med.* 2002;46(1):3-7.

57. Abe A, Takahashi N, Lee J, Oka T, Shizukuishi K, Kikuchi T, Inoue T, Jimbo M, Ryuo H, Bickel C. Performance evaluation of a hand-held, semiconductor (CdZnTe)-based gamma camera. *Eur J Nucl Med Mol Imaging.* 2003;30:805-811.

58. Mori I, Takayama T, Motomura N. The CdTe detector module and its imaging performance. *Annals Nucl Med.* 2001;15(6):487-494.

59. Kubo N, Zhao S, Fujiki Y, Kinda A, Motomura N, Katoh C, Shiga T, Kawashima H, Kuge Y, Tamaki N. Evaluation performance of a pixel array semiconductor SPECT system for small animal imaging. *Annals of Nucl Med.* 2005;19(7):633-639.

60. Jasczack RJ, Greer KL, Floyd CE, Harris CC, Coleman RE. Improved SPECT quantitation using compensation for scattered photons. *J Nucl Med.* 25:893-900.

61. Ogawa K, Harata Y, Ichihara T, Kubo A, Hashimoto S. A practical method for position-dependent Compton scatter correction in single photon CT. *IEEE TMI.* 1991;10:408-412.

62. Ogawa K, Ichihara T, Kubo A. Accurate scatter correction in single photon emission CT. *Ann Nucl Med Sci.* 1994;7:145-150.

63. Penny BC, King MA, Knesaurek K. A projector, back-projector pair which accounts for the two-dimensional depth and distance dependent blurring in SPECT. *IEEE TNS.* 1990;37:681-686.

64. Mitchell AJ, Sabondjian E, Sykes J, Deans L, Zhu W, Lu X, et al. Clearance Kinetics After Subendocardial or Subepicardial Injections of Endothelial Progenitor Cells in a Canine Myocardial Infarction Model. *J Nucl Med.* 2010; 51(3):413-417.

65. Gregoriou GK, Tsui BMW, Gullberg GT. Effect of truncated projections on defect detection in attenuation-compensation fanbeam cardiac SPECT. *J Nucl Med.* 1998;39:166-175.

66. Lalush DS, Tsui BMW. Performance of ordered-subset reconstruction algorithms under conditions of extreme attenuation and truncation in myocardial SPECT. *J Nucl Med.* 2000;41:737-744.

67. Kadrmas DJ, Jaszczak RJ, McCormick JW, Coleman RE, Lim CB. Truncation artifact reduction in transmission CT for improved SPECT attenuation compensation. *Phys Med Biol.* 1995;40:1085-1104.

68. McCue JD, Swingen C, Feldberg T, Caron G, Kolb A, Denucci C, et al**.** The real estate of myoblast cardiac transplantation: negative remodeling is associated with location. *J Heart Lung Transplant.* 2008 Jan;27(1):116-123.

69. Rubinshtein R, Miller TD, Williamson EE, Kirsch J, Gibbons RJ, Primak AN, McCollough CH, Araoz PA. Detection of myocardial infarction by dual-source coronary computed tomography angiography using quantitated myocardial scintigraphy as the reference standard. *Heart.* 2009;95(17):1419-1422.

70. Lund GK, Stork A, Saeed M, Bansmann MP, Gerken JH, Muller V, Mester J, Higgins CB, Adam G, Meinertz T. Acute myocardial infarction: evaluation with first-pass enhancement and delayed enhancement MR imaging compared with ^{201}Tl SPECT imaging. *Radiology.* 2004;232:49-57.

71. Holz A, Lautamaki R, Sasano T, Merrill J, Nekolla SG, Lardo AC, Bengel FM. Expanding the versatility of cardiac PET/CT: feasibility of delayed contrast enhancement CT for infarct detection in a porcine model. *J Nucl Med.* 2009;50(2):259-265.

CHAPTER 2: CARDIAC SPECT/CT: SLOW CT OR FAST CT?

2.1 INTRODUCTION

For many decades SPECT has been routinely used for myocardial perfusion imaging [1]. However, the diagnostic quality and quantitative accuracy of SPECT is affected by the physical effects of attenuation and scatter [2, 3], and therefore, SPECT would benefit from proper correction of these physical effects. The dominant effect reducing quantitative and diagnostic accuracy in cardiac SPECT is photon attenuation [4, 5, 6, 7]. In the past, non-uniform attenuation correction in SPECT was accomplished by way of radioisotope transmission imaging [8, 9, 10, 11, 12, 13, 14, 15, 16, 17]. Some of the challenges of radioisotope transmission imaging are limited resolution in the attenuation map, longer acquisition times that may increase the likelihood of patient motion, conversion of attenuation coefficients from the transmission energy to the emission energy, cross-talk between the transmission and emission data acquisitions, and the cost of frequently replacing the transmission radioisotope [4, 18, 19, 20, 21, 22, 23, 24, 25, 26, 27, 28]. The natural progression of transmission imaging moved toward x-ray CT [29], in part to address these concerns, and in part to provide the added benefit of improved anatomical localization.

Following the success in PET/CT [30], several manufacturers are now developing hybrid Single Photon Emission Computed Tomography / X-ray Computed Tomography (SPECT/CT) platforms [31]. The concept of utilizing CT for SPECT attenuation correction and image fusion has been studied even before the development of PET/CT [23, 32, 33]. The importance of SPECT/CT lies with the desire to provide anatomical

context to the functional information provided by SPECT, and the growing recognition that, in SPECT, attenuation is inherently non-uniform and correcting for its effects requires knowing the distribution of tissue density in the body with high spatial resolution [28]. Thus, moving to CT was received well, and it largely eliminated the problems associated with radioisotope transmission imaging [29, 30, 33, 34, 35]. In fact, a multi-centre evaluation of attenuation correction using both x-ray CT and radioisotope transmission imaging concluded that a high-quality attenuation map provided the best results when comparing uniformity in normal myocardium and defect contrast [36].

Attenuation correction depends upon the registration accuracy between SPECT and CT [37] and that the attenuation map matches the conditions under which the SPECT scan was acquired. In SPECT, due to the axial length of the gamma camera (approximately 30cm), all tomographic slices can be acquired simultaneously. Although some manufacturers acquire data with a gamma camera in continuous rotation, the majority of them acquire data in a stop-and-acquire manner, with each projection lasting about 5 to 20 seconds, depending on the application. Thus, when imaging the torso in SPECT the acquisition of each projection is averaged over the multiple phases, or even multiple cycles, of the respiratory cycle. CT gantries, on the other hand, move much faster and in a continuously rotating manner. In merging SPECT and CT platforms, manufacturers have taken one of two approaches to CT design. In the "slow rotation" design, a CT gantry completes a full 360^{o} rotation in approximately 15 seconds [8]; thus each CT projection is acquired during a different phase of the respiratory cycle, since breathing is maintained. Upon reconstructing data acquired in this manner, transaxial slices are often found to contain radial streaking artifacts that could have negative

implications for attenuation correction [38]. The "fast rotation" design completes a full 360^0 rotation in as little as 0.6 seconds, allowing all projections to be acquired during a single phase of the respiratory cycle (i.e. a breath-hold). With either design, the CT data will not be registered to the SPECT due to respiratory motion during the acquisition of the latter [39, 40], and hence quantitative accuracy will be compromised [41, 42, 43].

Given the above disparity between the methods of acquiring SPECT and CT, the question then arises: which is more suitable for SPECT attenuation correction, "slow rotation" or "fast rotation" CT? The idea of using a slow rotation or fast rotation has already been under debate in PET/CT systems [44]. Phantom and clinical studies have already demonstrated that a slow-rotating CT design in SPECT/CT provides adequate resolution and anatomical localization capabilities for attenuation correction purposes [45, 46], but studies comparing it to fast-rotation CTs have not been published. The purpose of this work was to compare “slow-rotation” with “fast-rotation” CT for their ability to correct for non-uniform attenuation in cardiac SPECT/CT taking into account the impact of physiological motion in both computer simulations and canine experiments.

2.2 METHODOLOGY

2.2.1 Computer Simulations

Computer models were developed of SPECT/CT systems with two CT designs. The slow-rotation CT design has a full-orbit (360^0) rotation time of 15 s, with slice thickness of 5 mm and acquires 4 slices per revolution. The fast-rotation CT features a full-orbit rotation time of 0.6 s, with 1.0 mm slice thickness and a 6-slice detector. These

models were meant to approximate the CT designs of the Infinia/Hawkeye-4 (General Electric, Waukesha, WI, USA) (slow CT) and Symbia/T6 (Siemens, Erlangen, Germany) (fast CT), both of which are in widespread clinical use.

Cardiac computer phantom

Our study used the 4DNCAT [47] digital phantom (see fig 2.1a), which simulates the human chest, including organs in a 3-dimensional spline frame, and features physiologic motion.

For this experiment, motion due to respiration was simulated, wherein the heart moved axially by a maximum of 2.3 cm. The cardiac cycle was not simulated. A five second sinusoidal breathing period was used, which was divided into ten frames comprising the respiratory cycle (0.5 s/frame). The 2.3 cm cardiac displacement is typical in humans during quiet breathing from rest or functional residual capacity (FRC) to FRC plus tidal volume (TV) [48]. Greater displacement would occur in respiratory disease with increased TV (i.e. emphysema), or during non-quiet breathing (i.e. sighs/yawns). The phantom was configured to simulate the distribution of the radiotracer ^{99m}Tc-MIBI, which is commonly used to evaluate myocardial viability (see fig 2.1b). The concentration of the radiotracer in each organ was derived from patient scans acquired in our clinic. The 4DNCAT phantom was also used to simulate the CT scans, which were converted into 140keV equivalent attenuation maps. Attenuation coefficients were calculated from measured values collected in clinical scans, which concur with published values [49]. These attenuation coefficients were for a narrow-beam CT acquisition. We have converted these results to provide broad-beam attenuation coefficients [50], to

compensate for the effects of scatter (Soft tissue = 0.12; Bone = 0.18; Lung = 0.04) during SPECT reconstruction.

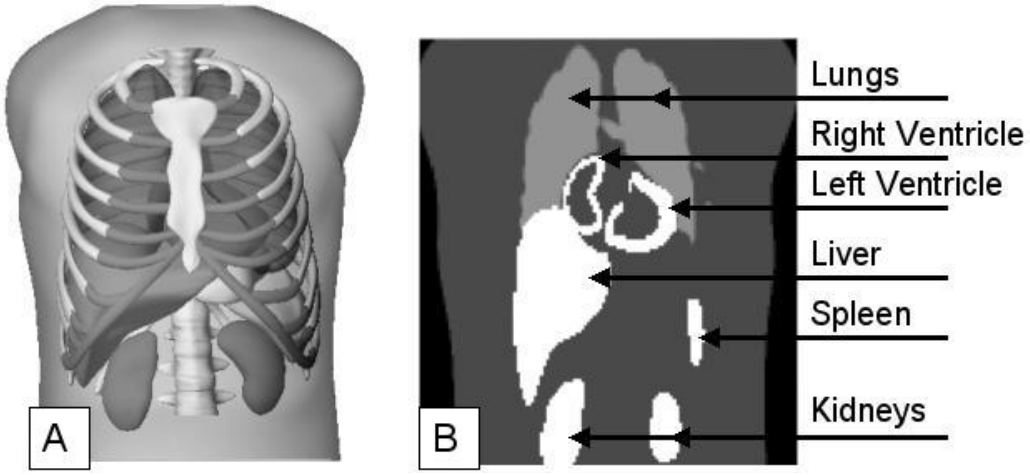

Figure 2.1: The computer phantom model of the chest

(A) 4DNCAT phantom displaying the organs that are simulated. (B) Activity distribution of the different organs. The ratio of the activity distribution was taken from clinical scans at our institution (soft tissue:lung:heart = 2:4:75).

Simulation of SPECT data acquisition

SPECT was simulated using SimSET (University of Washington, Division of Nuclear Medicine), which is a Monte Carlo based simulation software that models the physical effects of photon propagation in the phantom and the performance characteristics of typical SPECT systems. For the case of these simulations we used a typical parallel hole collimator (thickness = 2.405 cm; hole radius = 0.0555 cm; septal thickness = 0.016 cm), and with a detector crystal modelled to have a 10% intrinsic energy resolution. For SPECT, 1.5M counts were simulated to be detected over 128 projections over 360 degrees using 128x128 projection matrices. These parameters are

typical in our clinical cameras and cardiac procedures. The SPECT simulation was gated to the same respiratory cycle as the 4DNCAT phantom; therefore, 10 SPECT acquisitions were obtained providing approximately 150k counts per frame of the respiratory cycle.

Simulation of X-ray CT data acquisition

To model the slow rotation CT, different points in the respiratory cycle were selected and projected into arc-segments of the radon transform, leading to a set of inconsistent projections. These projections were tomographically reconstructed using filtered-backprojection, resulting in "motion-corrupted" tomographic slices, which were then used as the attenuation map in SPECT iterative reconstructions (see Fig.2.2A). To model the fast rotation CT, the respiratory cycle was fixed at FRC for the entire acquisition, and used as the attenuation map [51] in SPECT iterative reconstruction (see Fig.2.2B). As well nine other fast CT acquisitions were simulated, each one taken at a single point in the respiratory cycle progressing from the (FRC phase + TV/5) to (FRC + TV) and back down to FRC corresponding to a total of 10 CT data sets equally separating the cardiac displacement over 2.3cm.

Simulated SPECT/CT data reconstruction

SPECT data were reconstructed using an ordered subset iterative reconstruction algorithm [52] with four different scenarios:

(1) For the slow rotation CT, each of the 10-gated SPECT acquisitions were reconstructed using the single motion-corrupted CT as the attenuation map. (gated-SPECT/slow-CT)

(2) For the fast rotation CT, a breath hold CT at FRC was used as the attenuation map for each of the 10-gated SPECT reconstructions. (gated-SPECT/fast-CT)

(3) Reconstructions of the gated SPECT acquisitions with the corresponding gated CT as the attenuation map were used as our gold standard. (gated-SPECT/gated-CT)

(4) Finally, reconstructions with no attenuation correction were performed on the 10-gated SPECT acquisitions. (gated-SPECT/no-CT)

2.2.2 Analysis of computer simulations

Simulated attenuation maps

A comparison of the slow rotation CT and fast rotation CT attenuation maps with that of the gold standard was measured through the use of a linear sum algorithm [54]. The same central slice of the heart was taken for each map, and the sum of all lines (linear sum) from the centre of the attenuation map towards the exterior was taken for 128 angles spaced uniformly over 360 degrees (figure 3A). The RMS error was measured between the slow rotation and fast rotation CT attenuation maps with that of the gold standard for each of the 10 frames in the respiratory cycle using the following equation:

$$\sqrt{\frac{1}{N}\sum_{N}^{i}\left(\frac{GOLD(map)_i - TEST(map)_i}{GOLD(map)_i}\right)^2} \times 100 \qquad (2.1)$$

Where,
i = angle
N = Total number of angles (360)
GOLD(map) = Gold standard attenuation map
TEST(map) = Slow rotation or fast rotation CT derived attenuation map

Simulated SPECT reconstructions

A polar plot was constructed for each of the reconstructed data in all four scenarios (1 to 4 from section **2.2.1**: Simulated SPECT/CT data reconstruction) using in-house software [53]. To analyse and compare the different reconstruction methods the polar plots were compared in a pixel-by-pixel manner for each of the 10 frames of respiratory cycle and the root mean squared (RMS) error between (1) and (3), (2) and (3), and (4) and (3) was calculated as:

$$\sqrt{\frac{1}{N}\sum_{N}^{i}\left(\frac{GOLD_i - SIM_i}{GOLD_i}\right)^2} \times 100 \qquad (2.2)$$

Where,
i = pixel
N = total number of pixels
GOLD = Gold Standard (gated-SPECT/gated-CT) and,
SIM = Attenuation corrected reconstruction with slow CT (gated-SPECT/slow-CT) OR fast CT (gated-SPECT/fast-CT)
Note: The summation is taken over all pixels in the polar plot.

2.2.3 Canine experiments

Canine studies were approved by the Animal Use Subcommittee at the University of Western Ontario. A total of three adult canines (20 kg average mass) were used for this study. For each experiment the canine was injected with 400MBq of ^{99m}Tc-methoxyisobutylisonitrile (^{99m}Tc-MIBI) for myocardial perfusion imaging, and underwent cardiac SPECT/CT scans using an Infinia/Hawkeye-4 (General Electric Healthcare, Waukesha, WI, USA) (slow rotating CT), and a Symbia/T6 (Siemens Medical Systems, Erlangen, Germany) (fast rotating CT) and, both of which use dual-head SPECT. SPECT scans were acquired using 128 projections over 360 degrees (64 projections over 180 degrees per gamma camera head), 128x128 image matrices, and high-resolution parallel hole collimators (Symbia/T6: thickness = 2.405 cm; hole radius = 0.0555 cm; septal thickness = 0.016 cm, Infinia/Hawkeye-4: thickness = 3.5 cm; hole radius = 0.075 cm; septal thickness = 0.02 cm).

The canine was kept alive for a period of 1.5 hours to maximize the ^{99m}Tc-MIBI uptake. After which point the canine was euthanized and imaged on the Infinia/Hawkeye-4 SPECT/CT 4 hours post-mortem. Myocardial perfusion cardiac SPECT/CTs were performed with no ventilation (no respiratory motion: slow gold standard), and followed with assisted ventilation at 8 breaths/min to simulate respiratory motion. For the case of the Infinia/Hawkeye-4 scans the euthanized canines were ventilated for both the SPECT and CT portion due to the longer scan time for the slow rotation CT. The CT scan consisted of 5 mm thick slices. The time per projection for the SPECT scan was chosen to achieve a 1.5M count level for the entire slow gold standard scan (~35 s/projection), which is what is typically seen for clinical acquisitions.

To compensate for the effects of physical decay of the ^{99m}Tc, the time/projection for the SPECT scan with respiratory motion was increased to provide approximately the same total counts per projection as the slow gold standard scan.

The canine was then scanned on the Symbia/T6 7 hours post-mortem with no respiratory motion (fast gold standard), followed by another while the canine was ventilated (8 breaths/min) to once again simulate the motion of breathing. Since the Symbia/T6 is equipped with a fast rotating CT, the CT for this case was taken at end expiration (no ventilation) to simulate the acquisition at FRC that would have occurred if the canine was alive. The CTs of the chests were once again performed at a slice thickness of 5mm to be comparable to that of the Infinia/Hawkey-4's slow rotating CT. The time per projection for the SPECT scan was once again chosen to achieve a 1.5M count level for the entire fast gold standard scan (~45 s/projection). To compensate for the effects of physical decay of the ^{99m}Tc, the time/projection for the SPECT scan with respiratory motion was increased to provide approximately the same total counts per projection as the fast gold standard scan.

All the data from the Infinia/Hawkeye-4 canine experiments were reconstructed on the Xeleris workstation (version 2.0532) (General Electric Healthcare, Waukesha, WI, USA) and all the data from the Symbia/T6 canine experiments were reconstructed on the Symbia workstation (version 8.1.15.7 SP2) (Siemens Medical Systems, Erlangen, Germany). Clinical cardiac reconstruction parameters were used (ordered subset expectation maximization (OSEM) iterative algorithm consisting of 3 iterations, 16 subsets). In addition all reconstructions were normalized to the total counts in the image,

which corresponded to the gold standard for either the slow rotation CT or fast rotation CT equipped SPECT/CT.

2.2.4 Analysis of canine experiments

Experiments performed on the Infinia/Hawkeye-4 and the Symbia/T6 each had their own gold standard, which consisted of imaging with no respiratory motion (euthanized canine). Since changes in anatomy occur post-mortem [55], imaging on the Infinia/Hawkeye-4 commenced approximately 4 hours post-mortem, and images acquired while the canine was ventilated (with respiratory motion) were compared to images acquired with no respiratory motion. A region of interest (ROI) in a central slice of the heart was chosen and an RMS error was calculated between the two sets of images using the following equation:

$$\sqrt{\frac{1}{N}\sum_{N}^{i}\left(GOLD_i - VENTILATED_i\right)^2} \times 100 \qquad (2.3)$$

Where,
i = pixel
N = total number of pixels in slice
GOLD = Gold standard (no motion SPECT/CT reconstruction)
VENTILATED = SPECT/CT reconstruction with motion using either slow or fast CT attenuation maps
Note: Ventilated data was normalized to total counts in gold data

In addition to the RMS error, the ventilated data for the Infinia/Hawkeye-4 and Symbia/T6 was compared with the slow and fast gold-standard respectively using a scatter plot of the same ROI in the central slice of the heart and a correlation coefficient was recorded.

2.3 RESULTS

2.3.1 Computer Simulations

Results of the slow- and fast-CT 4DNCAT computer simulations are shown in Figure 2.2. Motion artifacts due to respiratory motion are readily apparent in the attenuation map reconstruction from the data acquired by the slow rotating CT. The artifacts can be seen in coronal and trans-axial planes, and are visualized qualitatively as (i) blurring in the direction of motion, most evident at the base of the lungs in the coronal plane, (ii) a contrast reduction in small structures, such as the ribs, and (iii) a background "noise" seen throughout soft-tissue and lung regions. Additionally, in the trans-axial plane, some radial streaking is apparent in soft-tissue regions around the periphery. From a quantitative perspective a profile through the coronal plane confirmed blurring artifacts at object boundaries, the loss of contrast of smaller structures and the presence of noise. The fast CT simulated attenuation map provided an attenuation map without blurring, contrast reduction and image noise.

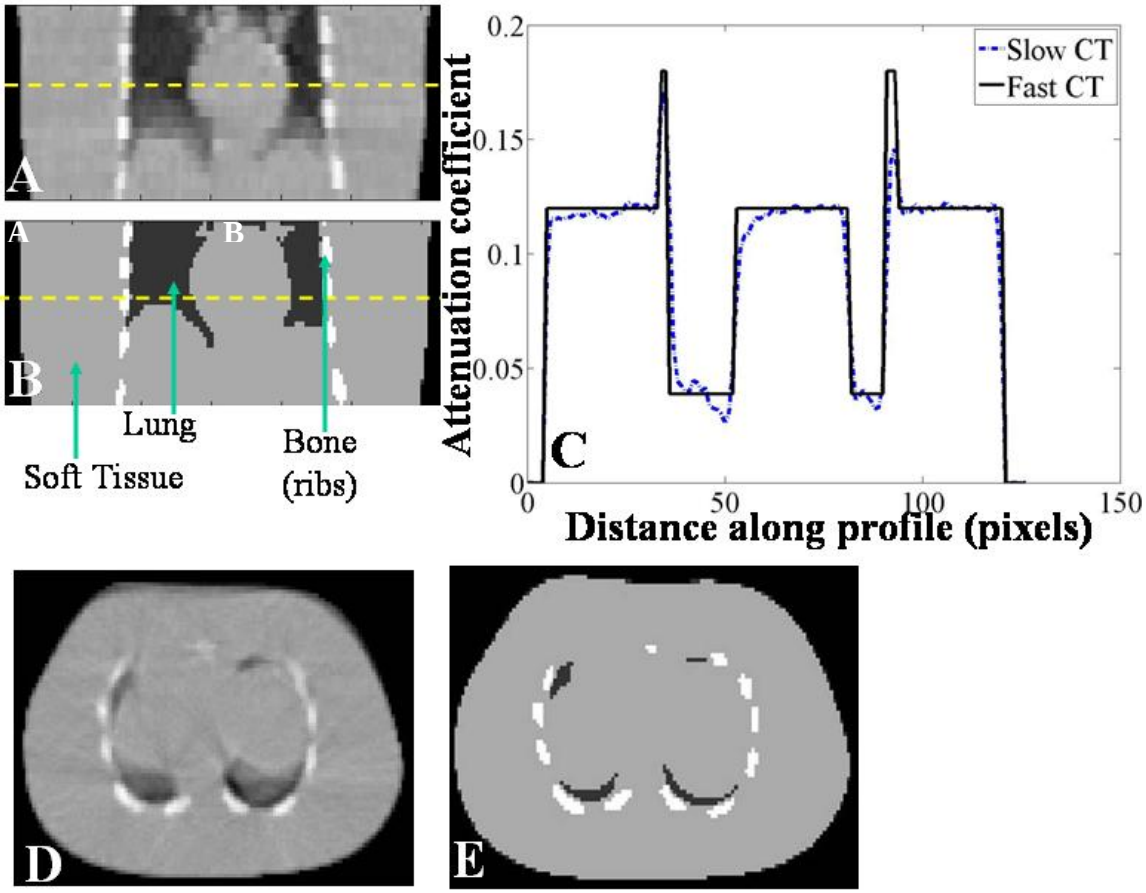

Figure 2.2: Comparing slow and fast CT attenuation maps

(A) Coronal slice of a slow CT attenuation map and a (B) fast CT attenuation map. Profiles taken across the dashed-line in (A) and (B) are seen in (C). Trans-axial slice of a (D) slow and a (E) fast rotation CT attenuation map at the level of the diaphragm. Notice the motion artifacts associated with the slow CT, and the loss of contrast in the image compared to the Fast CT acquisition at FRC.

Simulated attenuation maps

The result of the linear sum analysis of the attenuation maps is shown in Figure 2.3. First, for the slow rotating CT and fast rotating CT, the overall RMS error, relative to the gold standard (gated-CT) depends upon the respiratory frame. The slow-CT RMS error is never zero, since it is never equal to the gold standard. However, with the fast-CT, the RMS error is zero when comparing the same frame in the gold standard (gated-CT) that was used as the attenuation map for the fast-CT acquisition. By comparison of the slow-CT and fast-CT attenuation maps the average RMS error across all frames of the respiratory cycle improves from 2.4% to 1.5% respectively. Additional insight can be gained by considering the angular dependence of the error in linear sums. Figure 2.3(A) illustrates the location of the linear sums as a function of angle. Figure 2.3 (B) shows the linear sums as a function of angle for the slow-CT, the fast-CT as well as the gold-standard (gated-CT) (frames #1 and #5 are both shown). Linear sums are a function of angle as well as the frame in the respiratory cycle. For the slow-CT, linear sums are different than the gold standard (gated-CT) for both frames in the respiratory cycle at nearly all angles. For the fast-CT, linear sums are equal to frame #1 in the gold standard for all angles since this was the frame chosen for the fast-CT attenuation map, but substantial differences are noted for all angles when comparing fast-CT with the gold standard (gated-CT) at Frame #5.

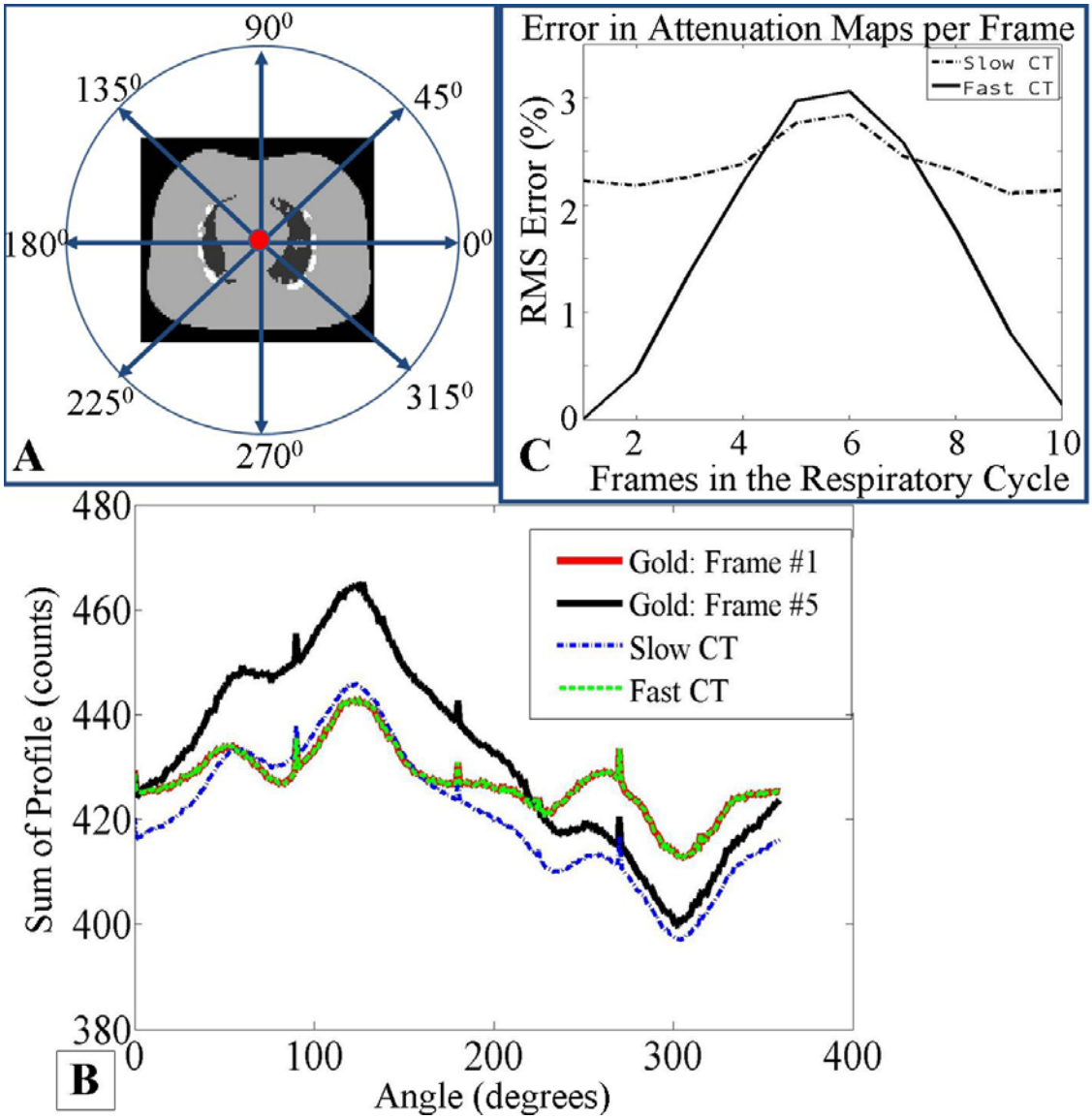

Figure 2.3: Linear sum errors comparing slow and fast CT attenuation maps

(A) Image displaying profile lines taken across all angles of the attenuation map. (B) Sum of profiles at each angle around the attenuation map for the slow-CT, fast-CT, and the gold standard (gated-CT) (frame#1 and frame#5). Note that the profiles for 'Gold: Frame #1' overlap with the profile for 'Fast CT'. (C) RMS error per frame of respiratory cycle between slow-CT and fast-CT attenuation maps compared to gold standard (gated-CT). Note: Frame #1 is equal to the FRC frame of the respiratory cycle.

Simulated SPECT reconstructions

Figure 2.4 summarizes the RMS errors for each frame in the respiratory cycle when analysing the computer simulation respiratory gated SPECT data reconstructed with attenuation correction. The RMS error in this case is calculated relative to the gold standard of gated-SPECT and gated-CT (gated-SPECT/gated-CT). The RMS error plot in figure 2.4 follows a similar trend as the plot in figure 2.3C for both the slow-CT and fast-CT attenuation maps. The RMS error for the first frame of the respiratory cycle was zero when using the fast-CT attenuation map. This is because the frame in the respiratory cycle used for the CT attenuation map (simulation of FRC) was equal to the frame of the respiratory cycle of the SPECT data that were collected. For the fast-CT as we move further away from the initial frame (i.e. from FRC to FRC + TV), the RMS errors increase, and gradually returns back towards zero as we return back to the exhalation frame (i.e. FRC of the respiratory cycle). For the slow-CT attenuation map the RMS error is never zero since the frame of the respiratory cycle of the CT data will never be equivalent to the frame of the respiratory cycle of the SPECT data. The RMS errors averaged across the frames respiratory cycle were found to be 4.2% for the SPECT data corrected with the slow-CT attenuation maps (gated-SPECT/slow-CT), and 4.0% for the SPECT data corrected with the fast-CT attenuation map (gated-SPECT/fast-CT). However, when no attenuation correction was used in SPECT reconstruction (gated-SPECT/no-CT), the average RMS error increased to 68.1%, relative to the gold standard (gated-SPECT/gated-CT).

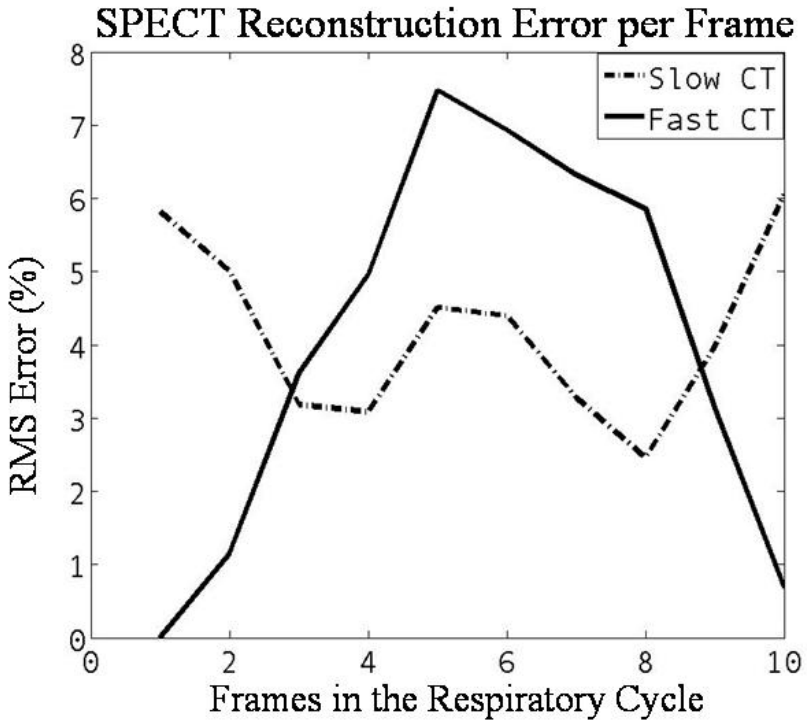

Figure 2.4: plot of error comparing SPECT reconstructions with slow and fast CT attenuation correction (From equation 2.2)

RMS error plot per frame of the respiratory cycle, comparing the SPECT reconstructions using slow-CT and fast-CT attenuation maps (gated-SPECT/slow-CT and gated-SPECT/fast-CT) with the gold standard (gated-SPECT/gated-CT). The RMS error using the fast-CT at the first frame is zero, since this was the frame used for the fast-CT attenuation map. The gated-SPECT/slow-CT RMS error is never zero, since the slow-CT attenuation map is never equal that of the gold standard (gated-CT). The SPECT simulations corresponded to 5 different lung volumes between FRC (frame #1) and FRC+TV (peaking at FRC+TV in frame #6). The fast-CT was acquired at FRC, while the slow-CT was acquired over 15s while the heart moved with a breathing period of five seconds.

To gain further insight into the origins of these errors, we compared count density profiles across the left ventricle from gated-SPECT/slow-CT, gated-SPECT/fast-CT, and gated-SPECT/gated-CT (gold standard) reconstructions. Figure 2.5 shows these profiles taken at frame 2 (FRC + TV/5) and frame 8 (FRC + TVx3/5) of the respiratory cycle. Using the slow-CT attenuation map (gated-SPECT/slow-CT), we notice a slight reduction in count density compared to the gold standard (gated-SPECT/gated-CT). This reduction is more pronounced for gated-SPECT/slow-CT frame 2 (See arrow in Figure 2.5a).

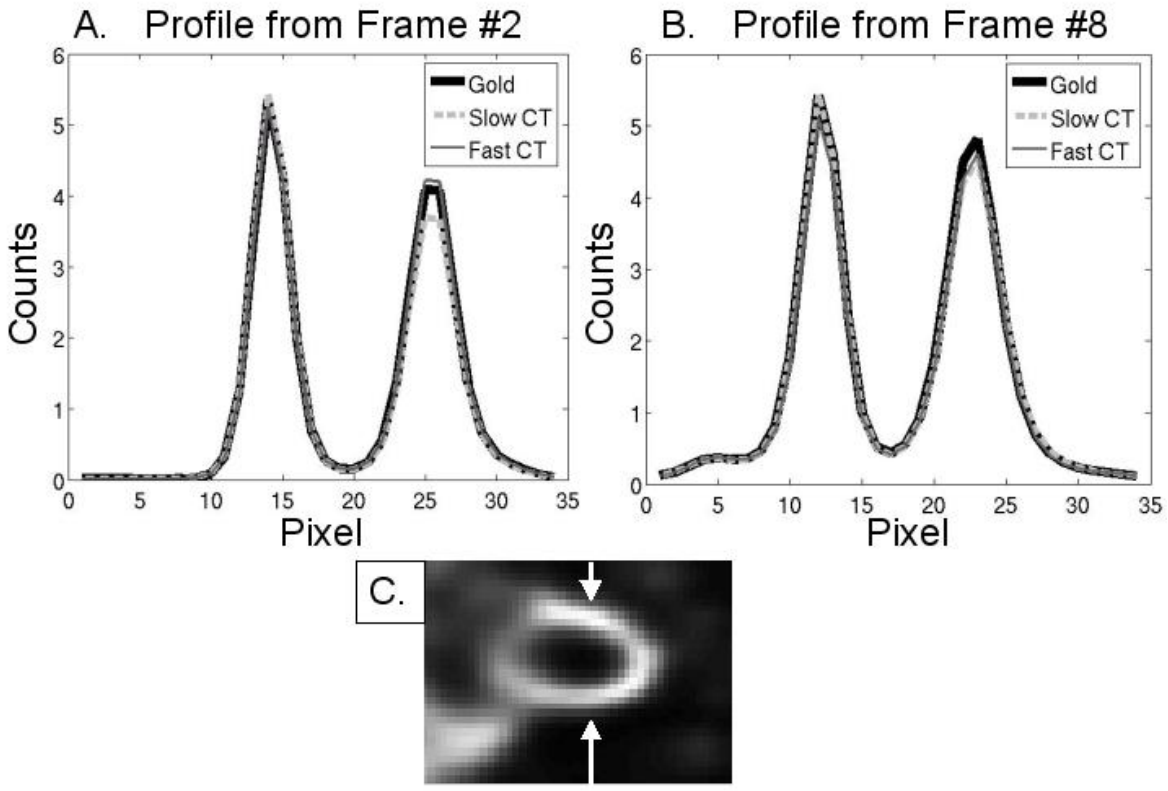

Figure 2.5: Comparing profiles of SPECT reconstructions with slow and fast CT attenuation correction

(A) Linear profile taken from frame 2 and (B) frame 8 from figure 2.4. Profile taken across left ventricle of the heart. (C) Coronal slice of the left ventricle displaying the location of the profiles taken across the heart. The profiles of the heart are comparing the three different attenuation maps for image reconstruction. Notice the loss of contrast when using Slow-CT attenuation map. Note: gated-SPECT/fast-CT and gated-SPECT/gated-CT (gold) profiles essentially overlap.

2.3.2 Canine experiments

To remove the confound of comparing SPECT of a live canine with SPECT of a deceased canine, we focused our experiments on recently deceased canines only. However, to evaluate changes between living and deceased canines, we performed CT scans on each canine prior to euthanization, as well as at multiple times points post-euthanization. Figure 2.6 shows that subtle differences are observed when comparing pre- and post-euthanized canines. Figures 2.6 a-c illustrate an enlargement of the mediastinum post-euthanization.

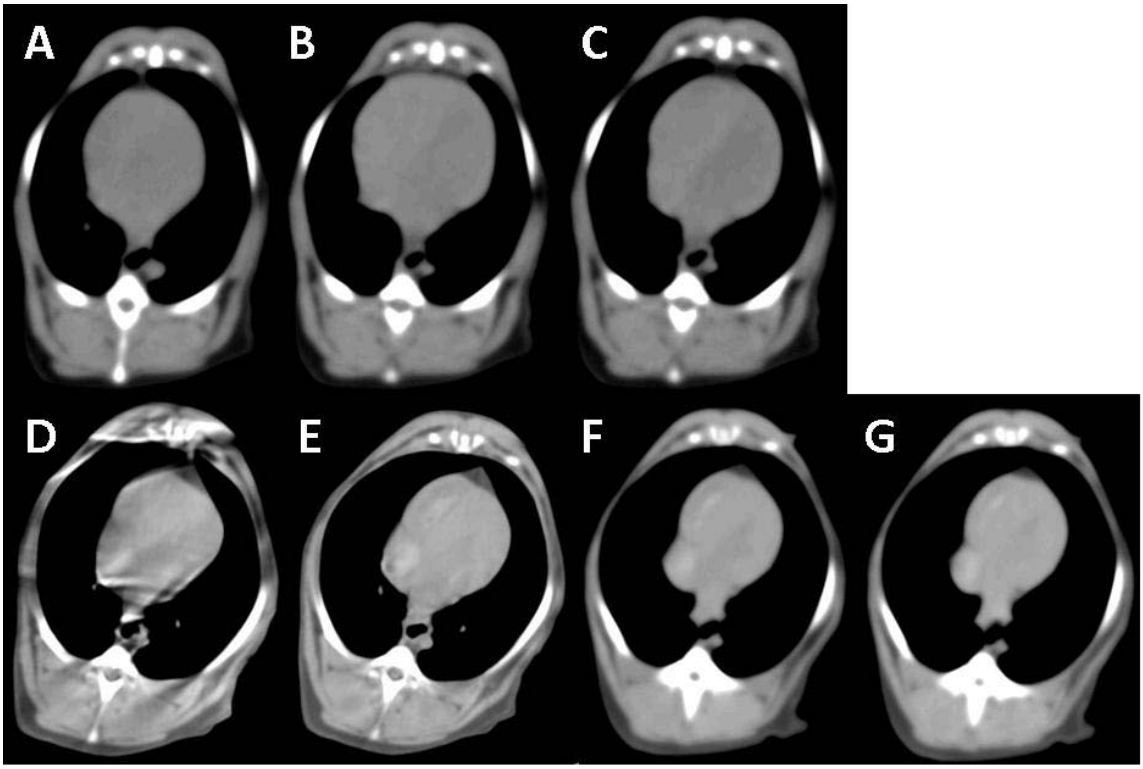

Figure 2.6: Changes in canine anatomy post-mortem

(A) CT scan while canine was alive and being ventilated. (B) CT taken after canine was euthanized, approximately 30min post-mortem, (C) 2 hours post-mortem, (D) 4 hours post-mortem, (E) 5 hours post-mortem, (F) 7 hours post-mortem, and (G) 8 hours post-mortem. For (A), (B), (C), (F), and (G) the CT scans were performed on the Symbia/T6 and were taken at functional residual capacity (FRC) by switching the ventilator off during the scans. For (D) and (E) the CT scans were performed on the Infinia/Hawkeye-4 with and without respiratory motion respectively. These images display the changes in the canine heart anatomy immediately after post-mortem, and the stabilization hours later.

The RMS errors comparing slow and fast rotation attenuation correction in the canine studies showed an improvement for all three canines when using the fast rotation CT of the Symbia/T6 (table 2.1). Figure 2.7 and 2.8 displays the SPECT images for all canines using the Infinia/Hawkeye-4 and the Symbia/T6 respectively. The scatter plot and profile across the chest for the first canine is also shown. The correlation coefficients calculated for all three canines improved when using the fast rotation attenuation map of the Symbia/T6 (table 2.2). The profile taken across the chest of canine #1 comparing the reconstructions with and without respiratory motion shows near perfect alignment for the Symbia/T6 (figure 2.8), as opposed to differences in contrast and the position of the peeks for the SPECT reconstructions using data acquired from the Infinia/Hawkeye-4 (figure 2.7).

Table 2.1: RMS error in Canine Studies

Canine	Infinia/Hawkeye-4 (Slow-CT attenuation map)	Symbia/T6 (Fast-CT attenuation map)
#1	44.4%	27.9%
#2	17.8%	9.8%
#3	21.9%	15.4%

Table 2.2: Correlation Coefficients in Canine Studies

Canine	Infinia/Hawkeye-4 (Slow-CT attenuation map)	Symbia/T6 (Fast-CT attenuation map)
#1	0.71	0.92
#2	0.92	0.99
#3	0.92	0.96

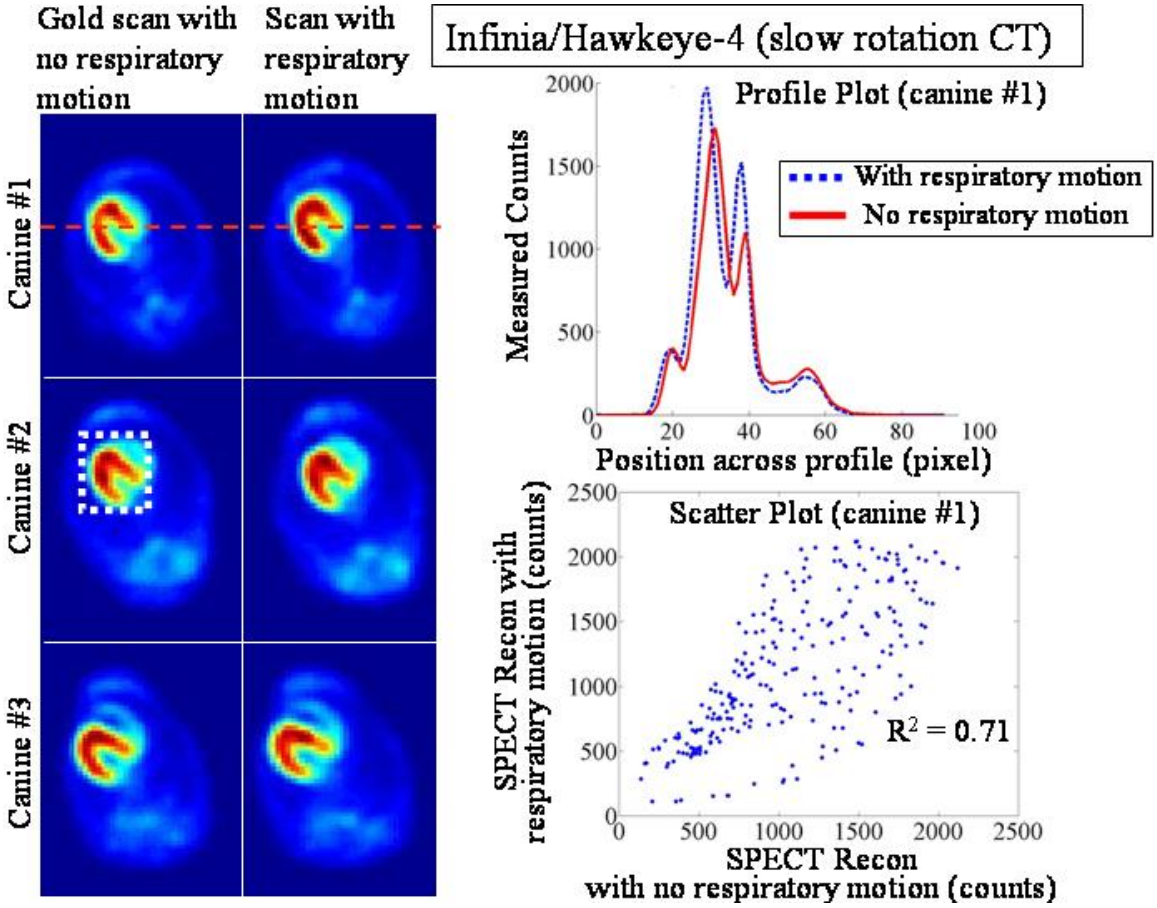

Figure 2.7: Comparing images and scatter plots to gold standard for cardiac canine SPECT/CTs using slow rotation attenuation maps

The first two columns are the central slices of the SPECT reconstruction using the Infinia/Hawkeye-4 slow rotating CT attenuation map with and without respiratory motion. A square ROI shown in canine #2 was used around the heart for the RMS error calculation and scatter plots for all canines. The last column consists of a plot of the profile across the heart and a scatter plot for canine #1 comparing the scan with and without respiratory motion. The profile was taken across the orange dashed line shown in the trans-axial image of canine #1.

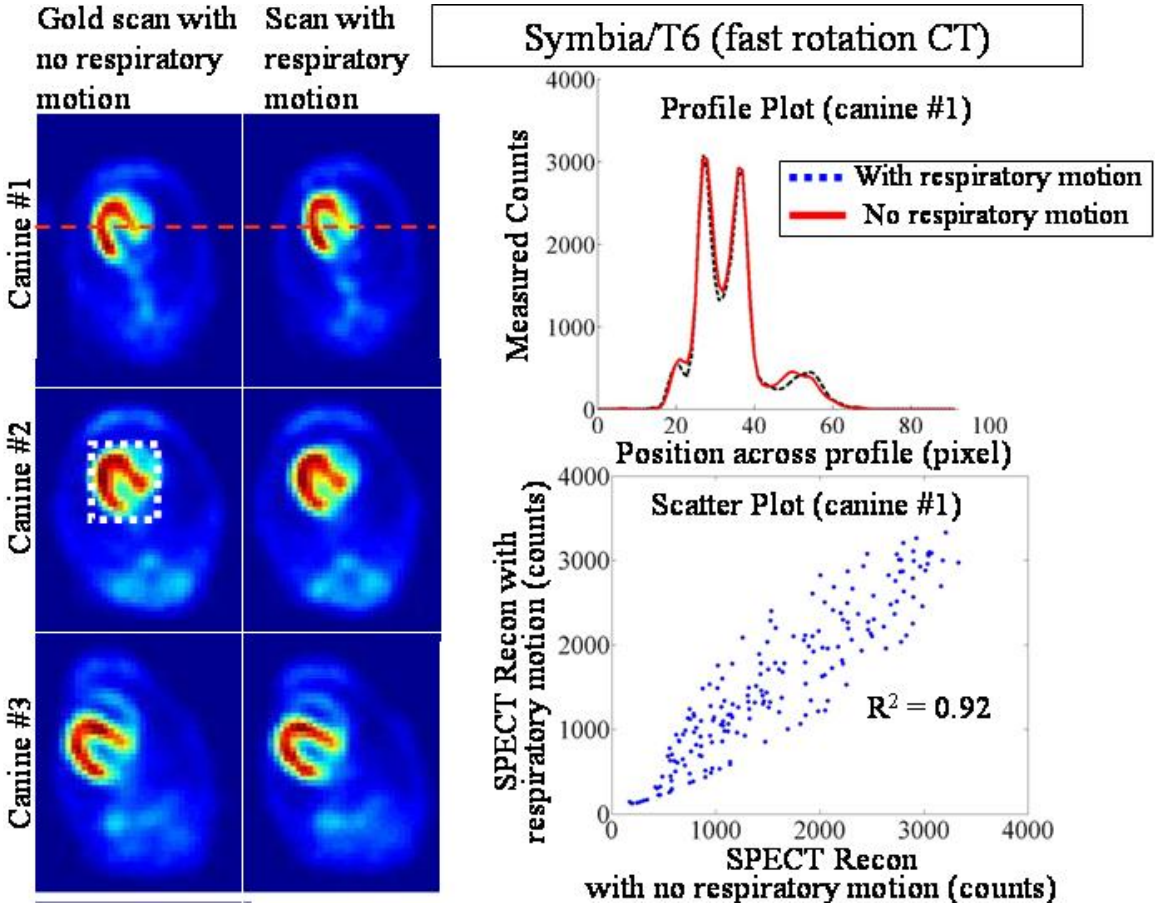

Figure 2.8: Comparing images and scatter plots to gold standard for cardiac canine SPECT/CTs using fast rotation attenuation maps

The first two columns are the central slices of the SPECT reconstruction using the Symbia/T6 fast rotating CT attenuation map with and without respiratory motion. A square ROI shown in canine #2 was used around the heart for the RMS error calculation and scatter plots for all canines. The last column consists of a plot of the profile across the heart and a scatter plot for canine #1 to compare the scan with and without respiratory motion. The profile was taken across the orange dashed line shown in the trans-axial image of canine #1.

2.4 DISCUSSION

The value of attenuation correction in cardiac SPECT/CT has long been the subject of debate [56] with some authors in support of its use [57, 58] and others opposed [59, 60]. Although multiple studies have shown the potential benefits of attenuation correction in SPECT [61], there is now further debate as to how that attenuation correction should be implemented [62]. Therefore, a study comparing SPECT/CT systems available today is opportune to gain knowledge as to which route to take in design of future SPECT/CT technologies. To our knowledge, there are no cardiac SPECT/CT publications comparing the respiratory motion artifacts arising from a slow rotation CT or a fast rotation CT attenuation map that is compared with no respiratory motion (gold standard). To this end, we performed both computer simulations using a well established digital phantom [47], and performed experiments in canines which are utilized widely as models of cardiac disease [63, 64, 65, 66].

2.4.1 Computer Simulations

We found that attenuation maps derived from a fast rotation CT had a lower RMS error (1.5%) than those derived from a slow rotation CT (2.4%). The fast and slow methods of CT data acquisition are different, both in terms of acquisition time per rotation and spatial resolution. These differences can be visualized easily (Figure 2.2). This improvement was found to propagate into the corresponding phantom SPECT reconstructions, where the error was found to depend on respiratory frame, when using both slow-CT and fast-CT attenuation maps. In the fast-CT case, the error ranged from zero error when the fast-CT was in the same respiratory frame as the gold standard CT,

to a maximum error when the fast-CT and gold-standard were at opposite frames in the respiratory cycle. However, in the case of the slow CT attenuation map SPECT reconstructions, the RMS error is less varied as a function of the respiratory frame. The differences in SPECT reconstructions between slow-CT and fast-CT are minimized when summing SPECT frames together to form an averaged SPECT. These 'average' RMS errors are 4.0% and 4.2% for the fast-CT and slow-CT respectively.

2.4.2 Canine Experiments

Our canine experiments were performed on deceased animals to enable complete control of the respiratory cycle, and image acquisition in the absence of respiratory and cardiac motion. Further, our study performed canine experiments in a design that allowed each canine to be its own gold standard. Since each canine is different, and cannot be compared to one another, the experimental design was set up in this manner to properly evaluate the two SPECT/CT designs.

Figure 2.6 shows that, without respiratory motion, CT image quality is similar for both fast and slow CT designs. However, in the presence of respiratory motion, slow rotation CT images were found to contain radial streak artifacts, as previously reported [38]; whereas the fast rotation CT remained free of motion artifacts. By referring to the profile across the heart in figure 2.8, we notice that the profile using the fast CT attenuation map in the Symbia/T6 reconstruction has a near perfect alignment and offers similar correction with and without respiratory motion. The profile across the heart for the slow CT attenuation map in the Infinia/Hawkeye-4 reconstruction (figure 2.7) shows an over correction in counts when respiratory motion is present. This may be explained

by referring to the CT scan seen in figure 2.6d, where motion in the slow CT acquisition changes the attenuation coefficients to higher values which are similar to that of bone due to the streaking artifacts causing the over correction in the SPECT reconstructed image.

Concerning the impact of the fast and slow CT attenuation maps on SPECT reconstructions, RMS errors were smaller and correlation coefficients were higher for the fast CT compared to the slow CT, for all three canines. This effect was larger than what was recorded in the averaged computer simulations. It is important to note that our canine SPECT imaging was performed without respiratory gating, thus the impact of mis-registration is averaged across all SPECT frames of the respiratory cycle. SPECT data is acquired across tens of minutes and each projection is averaged across all frames of the respiratory cycle. In the case of fast CT, data is acquired in seconds and in a single frame of the respiratory cycle (breath-hold). In the case of slow CT, data is acquired in a few minutes with the patient free breathing, thus projections are acquired in different frames of the respiratory cycle. These differences lead to mis-registration errors between SPECT and CT data and thus compromise attenuation correction. Perhaps one method for addressing the challenge of mis-registration is to acquire gated CT (cine CT) and gated SPECT, which has been proposed for PET/CT [53]. However, cine CT acquisitions will substantially increase patient dose, while gated SPECT will lead to a marked reduction in count density or lengthen SPECT acquisition time and increase patient discomfort.

2.4.3 Patient Motion in SPECT/CT

Patient motion is an important determinant in SPECT/CT image quality. In cardiac imaging, two important aspects of motion arise from the beating heart and the respiratory cycle. Our study focused on respiratory motion only, which is generally larger in magnitude than cardiac motion [67]. For our computer phantom, we modelled a breathing phantom with a non-beating heart, and simulated data acquisition using respiratory-gated SPECT and CT, which is not standard clinical practice. For our canine experiments, we once again only looked at respiratory motion and not cardiac motion. This was necessary since only in a deceased canine could we control and arrest completely the respiratory motion, which was required for the gold-standard in our experimental design. The assessment of motion artifacts arising from a beating heart is important, and future studies could examine this aspect via computer simulations. From an experimental perspective, other groups are looking into the potential of respiratory-cardiac double-gated SPECT [68].

2.4.4 Radiation Dose

One concern with SPECT/CT is the increased dose associated with the CT scan. Radioisotope transmission imaging, the predecessor to CT in attenuation map measurements, typically imparted a dose of a few μSv [69]. The typical radiation dose experienced from a slow rotating CT such as the one used in the Infinia/Hawkeye-4, is on the order of 0.5 mSv [70]. The radiation dose associated with a fast rotation CT such as the design used in the Symbia/T6 is on the order of 2-4 mSv [71]. In addition to this radiation dose, the radioisotope dose given to the patient for the SPECT portion must

also be considered. For the purpose of a rest/stress myocardial perfusion SPECT scan the radiation dose is approximately 12.5 mSv [71]. Thus, although the doses associated with measuring attenuation maps are only 10-20% of those involved with SPECT, there is a trend towards increasing dose as technology has progressed in attenuation maps measurements.

2.5 CONCLUSION

This study compared slow-rotation and fast-rotation CT in their abilities to facilitate non-uniform attenuation correction for myocardial perfusion cardiac SPECT/CT. Both strategies for CT data acquisition were susceptible to artifacts induced by breathing, and these artifacts compromised their ability to correct for attenuation.

Effects are most pronounced for attenuation maps, where they are even visually apparent. Effects in SPECT reconstruction are more subtle, but can impact quantitative analysis. Fundamentally, SPECT and CT data are acquired over very different time frames relative to the respiratory cycle; thus fusing these two modalities will always challenge registration and, in turn, attenuation correction.

2.6 REFERENCES

1. Jaszczak RJ. The early years of single photon emission computed tomography (SPECT): an anthology of selected reminiscences *Phys. Med. Biol.* 2006;51:R99-R115

2. Corbett JR, Kritzman JN, Ficaro EP. Attenuation correction for single photon emission computed tomography myocardial perfusion imaging *Current Cardiology Reports.* 2004;6:32-40

3. Van Train KF, Garcia EV, Maddahi J, Areeda J, Cooke CD, Kiat H, Silagan G, Folks R, Friedman J, Matzer L, Germano G, Bateman T, Ziffer J, DePuey EG, Fink-Bennett D, Cloninger K, Berman DS. Multicenter trial validation for quantitative analysis for same-day rest-stress technetium-99m-sestamibi myocardial tomograms *J. Nucl. Med.* 1994;35:609-618

4. Bateman TM and Cullom SJ. Attenuation correction single-photon emission computed tomography myocardial perfusion imaging *Semin. Nucl. Med.* 2004;35:37-51

5. DePuey EG. How to detect and avoid myocardial perfusion SPECT artifacts *J. Nucl. Med.* 1994;35:699-702

6. King MA, Tsui BM, Pan TS. Attenuation compensation for cardiac single-photon emission computed tomographic imaging: Part1. Impact of attenuation and methods of estimating attenuation maps *J. Nucl. Cardiol.* 1995;2:513-524

7. King MA, Tsui BM, Pan TS, Glick SJ, Soares EJ. Attenuation compensation for cardiac single-photon emission computed tomographic imaging: Part2. Attenuation compensation algorithms *J. Nucl. Cardiol.* 1996;3:55-64

8. O'Connor MK and Kemp BJ. Single-photon emission computed tomography/computed tomography: Basic instrumentation and innovations *Semin. Nucl. Med.* 2006;36:258-266

9. Jaszczak RJ, Gilland DR, Hanson MW, Jang S, Greer KL, Coleman RE. Fast transmission CT for determining attenuation maps using a collimated line source, rotatable air-copper-lead attenuators and fan-beam collimation *J. Nucl. Med.* 1993; 34:1577-1586

10. Celler A and Sitek A. Transmission SPECT scans using multiple collimated line sources *Proc. IEEE Med. Imaging Conference* 1995:1121-1125

11. Beekman FJ, Kamphuis C, Hutton BF, van Rijk PP. Half-fanbeam collimators combined with scanning point sources for simultaneous emission-transmission imaging *J. Nucl. Med.* 1998; 39:1996-2003

12. Mayneord WV. The radiography of the human body with radioactive isotopes *Br. J. Radiol.* 1952; 25:517-525

13. Kuhl DE, Hale J, Eaton WL. Transmission scanning: a useful adjunct to conventional emission scanning for accurately keying isotope deposition to radiograhic anatomy *Radiology.* 1966; 87:278-284

14. Ficaro EP, Fessler JA, Rogers WL, Schwaiger M. Comparison of americium-241 and technetium-99m as transmission sources for attenuation correction of thallium-201 SPECT imaging of the heart *J. Nucl. Med.* 1994; 35:652-663

15. du Raan H, du Toit PD, van Aswegen A, Lotter MG, Herbst CP. Implementation of a Tc-99m and Ce-139 scanning line source for attenuation correction in SPECT using a dual opposing detector scintillation camera *Med. Phys.* 2000;27(7):1523-1534

16. Kemp BJ, Prato FS, Dean GW, Nicholson RL, Reese L. Correction for attenuation in technetium-99m-HMPAO SPECT brain imaging *J. Nucl. Med.* 1992;33:1875-1880

17. Stodilka RZ, Kemp BJ, Prato FS, Nicholson RL. Importance of bone attenuation in brain SPECT quantification *J. Nucl. Med.* 1998;39:190-197

18. Cullom SJ, Lui L, White ML. Compensation of attenuation map errors from Tc-99m-sestamibi downscatter with simultaneous Gd-153 transmission scanning *J. Nucl. Med.* 1996;37:215P

19. Almquist H, Arheden H, Arvidsson AH, Pahlm O, Palmer J. Clinical implication of down-scatter in attenuation-corrected myocardial SPECT *J. Nucl. Cardiol.* 1999;6:406-411

20. Gullberg GT, Morgan HT, Zeng GL, et al. The design and performance of simultaneous transmission and emission tomography system *IEEE T. Nucl. Sci.* 1998;45:1676-1698

21. Garcia EV. Updated imaging guidelines for nuclear cardiology procedures, part 1 *J. Nucl. Cardiol.* 2001;8:G5-G58

22. Zhao Z, Ye J, Durbin M, et al. Estimiation of the optimum transmission scan time by using the subjects weight, height and the transmission source strength. *J. Nucl. Med.* 2001;42:195P

23. Zaidi H and Hasegawa B. Determination of the attenuation map in emission tomography *J. Nucl. Med.* 2003;44:291-315

24. Narayanan MV, King MA. An iterative transmission algorithm incorporating cross-talk correction for SPECT. *Am Assoc Med. Phys.* 2002;29(5):694-700

25. Tan P, Bailey DL, Meikle SR, Eberl S, Fulton RR, Hutton BF. A scanning line source for simultaneous emission and transmission measurements in SPECT *J. Nucl. Med.* 1993;28:844-851

26. Celler A, Sitek A, Stoub E, Hawman P, Harrop R, Lyster D. Multiple line source array for SPECT transmission scans: simulation, phantom and patient studies *J. Nucl. Med.* 1998;39:2183-2189

27. Gifford HC, Narayanan MV, Farncombe TH, Simkin PH, Licho R, King MA. Simultaneous emission-transmission imaging with Ga-67 and Tc-99m scanning line source *J. Nucl. Med.* 2001;42:196P-197P

28. Celler A, Dixon KL, Chang Z, Blinder S, Powe J, Harrop R. Problems created in attenuation-corrected SPECT images by artifacts in attenuation maps: a simulation study *J. Nucl. Med.* 2005;46:335-343

29. Bocher M, Balan A, Krausz, Shrem Y, Lonn A, Wilk M, Chisin R. Gamma camera mounted anatomical X-ray tomography: Technology, system characteristics and first images *Eur. J. Nucl. Med.* 2000;27:619-627

30. Beyer T, Townsend DW, Brun T, Kinahan PE, Charron M, Roddy R, Jerin J, Young J, Byars L, Nutt R. A combined PET/CT scanner for clinical oncology *J. Nucl. Med.* 2000;41 1369-79

31. Buck AK, Nekolla S, Ziegler S, Beer A, Krause BJ, Herrmann K, Scheidhauer K, Wester HJ, Rummeny EJ, Schwaiger M, Drzezga A. SPECT/CT *J. Nucl. Med.* 2008;49:1305-1319

32. Hasegawa B, Gingold EL, Reilly SM, et al. Description of a simultaneous emission transmission CT system. *Proc. SPIE* 1990;1231:50-60

33. Kalki K, Blankespoor SC, Brown K, Hasegawa BH, Dae MW, Chin M. Myocardial perfusion imaging with a combined x-ray CT and SPECT system *J. Nucl. Med.* 1997;38:1535-1540

34. Patton JA et al. Image fusion using an integrated, dual-head coincidence camera with x-ray tube-based attenuation maps *Eur. J. Nucl. Med.* 2000;41:1364-1368

35. Seo Y, Mari C, Hasegawa BH. Technological development and advances in single-photon emission computed tomography/computed tomography *Semin. Nucl. Med.* 2008;38:177-198

36. O'Connor MK et al. A multicenter evaluation of commercial attenuation compensation techniques in cardiac SPECT using phantom models *J. Nucl. Cardiol.* 2002;9:361-376

37. Stone CD, McCormick JW, Gilland DR, Greer KL, Coleman RE, Jaszczak RJ. Effect of registration errors between transmission and emission scans on a SPECT system using sequential scanning *J. Nucl. Med.* 1998;39:365-373

38. Chen J, Garcia EV, Folks RD, Peretz A, Galt JR. Adaptive bayesian iterative transmission reconstruction for attenuation correction in myocardial perfusion imaging with SPECT/slow-rotation low-output CT systems *International J. Biomed. Imaging.* 2007;2007:1-7 (ID 18709)

39. McQuaid SJ and Hutton BF. Sources of attenuation-correction artefacts in cardiac PET/CT and SPECT/CT *Eur. J. Nucl. Med. Mol. Imaging* 2008;35:1117-1123

40. Patton JA and Turkington TG. SPECT/CT physical principles and attenuation correction *J. Nucl. Med. Technol.* 2008;36:1-10

41. Goetze S and Wahl RL. Prevalence of misregistration between SPECT and CT for attenuation-corrected myocardial perfusion SPECT *J. Nucl. Cardiol.* 2007;14:200-206

42. Goetze S, Brown TL, Lavely WC, Zhang Z, Bengel FM. Attenuation correction in myocardial perfusion SPECT/CT: Effects of misregistration and value of reregistration *J. Nucl. Med.* 2007;48:1090-1095

43. Tonge CM, Ellul G, Pandit M, Lawson RS, Shields RA, Arumugam P, Prescott MC. The value of registration correction in the attenuation correction of myocardial SPECT studies using low resolution computed tomography images *Nucl. Med. Commun.* 2006;27:843-852

44. Brunken RC et al. Clinical evaluation of cardiac PET attenuation correction using 'fast' and 'slow' CT images *J. Nucl. Med.* 2004;45:120P

45. Hamann M, Aldridge M, Dickson J, Endozo R, Lozhkin K, Hutton BF. Evaluation of a low-dose/slow-rotating SPECT-CT system *Phys. Med. Biol.* 2008;53:2495-2508

46. Preuss R, Weise R, Lindner O, Fricke E, Fricke H, Burchert W. Optimisation of protocol for low dose CT-derived attenuation correction in myocardial perfusion SPECT imaging *Eur. J. Nucl. Med. Mol. Imaging* 2008;35:1133-1141

47. Segars WP. Development and Application of the New Dynamic NURBS-based Cardiac-Torso (NCAT) Phantom. *Ph.D. Dissertation, The University of North Carolina.* 2001

48. Comroe JH. Physiology of Respiration. Chicago, IL, *Year Book Medical Publishers Inc.* 1965

49. Cherry SR, Sorenson JA, Phelps ME. Physics in Nuclear Medicine (ed 3). Philadelphia, PA, *Saunders* 2003

50. Stodilka RZ. Scatter and attenuation correction for brain SPECT. *PhD Dissertation, The University of Western Ontario.* 1999

51. Utsunomiya D, Nakaura T, Honda T, Shraishi S, Tomiguchi S, Kawanaka K, Morishita S, Awai K, Ogawa H, Yamashita Y. Object-specific attenuation correction at SPECT/CT in thorax: optimization of respiratory protocol for image registration *Radiology.* 2005;237:662-669

52. Hudson HM and Larkin RS. Accelerated image reconstruction using ordered subsets of projection data. *IEEE T. Med. Imaging* 1994;13(4):601-609.

53. Russell RAH, Carnes G, Lee TY, Wells RG. Respiration-averaged CT for attenuation correction in canine cardiac PET/CT *J. Nucl. Med.* 2007;48:811-818

54. Lalush DS and Tsui BMW. Fast transmission CT reconstruction for SPECT using a block iterative algorithm *IEEE T Nucl. Sci.* 2000;47(3):1123-1129

55. Heng HG, Selvarajah GT, Lim HT, Ong JS, Lim J, Ooi JT. Serial post-mortem thoracic radiographic findings in canine cadavers. *Forensic Science International* 2009;188:119-124

56. Watson DD. Attenuation correction: To be or not to be *J. Nucl. Cardiol.* 2007;14:15

57. Garcia EV. SPECT attenuation correction: An essential tool to realize nuclear cardiology's manifest destiny *J. Nucl. Cardiol.* 2007;14:16-24

58. Dondi M, Fagioli G, Salgarello M, Zoboli S, Nanni C, Cidda C. Myocardial SPECT: what do we gain from attenuation correction (and when)? *Q. J. Nucl. Med.* 2004;48(3):181-187

59. Germano G, Slomka PJ, Berman DS. Attenuation correction in cardiac SPECT: The boy who cried wolf? *J. Nucl. Cardiol.* 2007;14:25-35

60. Wackers FJ Th. Attenuation compensation of cardiac SPECT: A critical look at a confusing world *J. Nucl. Cardiol.* 2002;9(4):438-440

61. Bybel B, Brunken RC, DiFilippo FP, Neumann DR, Wu G, Cerqueira MD. SPECT/CT imaging: Clinical utility of an emerging technology *RadioGraphics* 2008;28:1097-1113

62. Singh B, Bateman TM, Case JA, Heller G. Attenuation artifact, attenuation correction, and the future of myocardial perfusion SPECT *J. Nucl. Cardiol.* 2007;14:153-164

63. Willmann JK, Paulmurugan R, Rodriguez-Porcel M, Stein W, Brinton TJ, Connolly AJ, Nielsen CH, Lutz AM, Lyons J, Ikeno F, Suzuki Y, Rosenberg J, Chen IY, Wu JC, Yeung AC, Yock P, Robbins RC, Gambhir SS. Imaging gene expression in human mesenchymal stem cells: From small to large animals. Radiology 2009;252(1):117-27.

64. Christian TF, O'Connor MK, Schwartz RS, Gibbons RJ, Ritman EL. Technetium-99m MIBI to assess coronary collateral flow during acute myocardial infarction in two closed-chest animal models. J Nucl Med 1997;38(12):1840-6.

65. Wisenberg G, Lekx K, Zabel P, Kong H, Mann R, Zeman PR, Data S, Culshaw CN, Merrifield P, Bureau Y, Wells G, Sykes J, Prato FS. Cell tracking and therapy evaluation of bone marrow monocytes and stromal cells using SPECT and CMR in a canine model of myocardial infarction. J Cardiovasc Magn Reson 2009; 11:11-27

66. Pereira RS, Prato FS, Sykes J, Wisenberg G. Assessment of myocardial viability using MRI during a constant infusion of Gd-DTPA: further studies at early and late periods of reperfusion. Magn. Reson. Med. 1999;42(1):60–68

67. Ortmaier T, Groger M, Boehm DH, Falk V, Hirzinger G. Motion estimation in beating heart surgery *IEEE T Bio-Med Eng.* 2005;52(10):1729-1740

68. Bitarafan A, Rajabi H, Guy B, Rustgou F, Sharafi AA, Firoozabady H, Yaghoobi N, Malek H, Pirich C, Langesteger W, Beheshti M. Respiratory motion detection and correction in ECG-gated SPECT: a new approach *Korean J. Radiol.* 2008;9:490-497

69. Perisinakis K, Theocharopoulos N, Karkavitsas N, Damilakis J. Patient effective radiation dose and associated risk from transmission scans using 153Gd line sources in cardiac spect studies. Health Phys. 2002;83(1):66-74.

70. Schillaci O. Hybrid SPECT/CT: a new era for SPECT imaging? *Eur J Nucl Med Mol Imaging.* 2005;32:521-524.

71. Bach-Gansmo T, Schwarzlmüller T, Jøraholmen V, Salbu J, Biermann M, Naum A, Kleven-Madsen N. SPECT/CT hybrid imaging; with which CT? *Contrast Media Mol. Imaging.* 2010;5(4):208-212.

72. Radiation dose to patients from radiopharmaceuticals. *Annals of the ICRP. ICRP Publication 80.* 1998;28(3):113-120.

CHAPTER 3: HYBRID SPECT/CARDIAC-GATED FIRST-PASS PERFUSION CT: LOCATING TRANSPLANTED CELLS RELATIVE TO INFARCTED MYOCARDIAL TARGETS

3.1 INTRODUCTION

The transplantation of stem cells for the purpose of treating heart disease is being widely investigated [1]. To accurately evaluate the delivery and therapeutic effectiveness of transplanted cell (TC) therapy sophisticated non-invasive techniques must be established to visualize cell delivery, degree of retention, functionality, and long-term survival. Such techniques that afford the localization and quantification of TC populations throughout early infarct evolution are of particular interest, and several imaging techniques are under investigation [2, 3]. Magnetic Resonance Imaging (MRI) of TCs using iron-oxide particles has shown promise in several animal studies [4, 5]; however, it is currently limited by low sensitivity and lack of specificity for intact, viable cells [2, 6]. Despite this, delayed enhancement MRI does provide the most accurate means of identifying infarct extent and location [7]. Positron Emission Tomography (PET) can also be used to localize TCs with the use of ^{18}F-fluorodeoxyglucose (^{18}F-FDG) labeling, but is limited by the short half-life of the radioisotope [8] and rapid clearance from labeled cells. Recently, it has been shown that cells may also be labeled with ^{64}Cu-Pysuvaldehyde-Bis(N4-Methylthiosemicarbazone) (PTSM), allowing cells to be followed for longer periods of time than with ^{18}F-FDG. However, ^{64}Cu is not readily available and its half-life of 13-hours is still short for following cell lines over extended periods [9].

Hybrid imaging using Single Photon Emission Computed Tomography / Computed Tomography (SPECT/CT), is a novel approach to the localization of TCs and may be accomplished through the labeling of cells with ^{111}In [10]. ^{111}In is more readily available than ^{64}Cu and has a significantly longer half-life (2.8 days). We have shown that this tracer can be used to follow transplanted bone marrow monocytes and mesenchymal cells for a period of two weeks [11], making this technique highly attractive for following TC populations. By combining this technique with concurrently acquired CT (SPECT/CT), accurate spatial registration of these cells to anatomical landmarks can be accomplished. However, it has recently been demonstrated that first-pass cardiac-gated CT can allow spatial localization of myocardial infarction, raising the potential for a combined TC-infarct evaluation using this hybrid-imaging platform.

Delayed-enhancement (DE) imaging using CT has been recently explored, mirroring the more established MRI technique used extensively in clinical practice [12, 13]. However, it has also been observed that first-pass cardiac CT imaging also initially demonstrates hypo-enhancement in regions of myocardial infarction [14, 15]. These regions have been shown to correlate well to areas of reduced perfusion using Technetium (^{99m}Tc) perfusion imaging [16], and DE imaging with either MRI or CT and likely represent the infarct core where micro-vascular blood flow is most severely compromised [15, 17]. Such an evaluation for first-pass CT can be accomplished using low-dose calcium scoring CT protocols with similar sensitivity to high-dose protocols [18], which can be implemented in a commercial hybrid SPECT/CT system.

We previously described experiments involving ^{111}In radio-labeling of cells, transplanting those radiolabeled cells and visualizing the distribution of the ^{111}In hotspot

using SPECT [11]. In that work, we saw that the background corrected signal intensity of the hotspot decreases with time, and we proposed an in-depth model for explaining this decrease [11]. That model proposes that some of the ^{111}In remains in the cells and some washes out of the cells, and further, that some cells remain, and some die and/or are removed from the injection site [11]. In this manuscript, we describe similar experiments involving ^{111}In radio-labeling of cells and then characterizing the ^{111}In hotspot using SPECT in terms of minimum detectable activity. We also evaluate the feasibility of temporally and spatially localizing ^{111}In–labeled stem cells relative to infarcted myocardium using a hybrid SPECT/[first-pass perfusion CT] imaging protocol.

3.2 METHODS

3.2.1 Validation of SPECT and CT Image Co-Registration

SPECT/CT was acquired using a standard clinical protocol (64 projections, 30s/projection, 128x128 image matrix) followed by a CT scan (17mAs, helical CT). This was performed on two capillary tubes (1mm inner diameter) containing identical mixtures of 300mgI/mL CT contrast (Omnipaque, General Electric Healthcare, Waukesha, WI) and 50MBq ^{99m}Tc. These tubes were oriented in a ‘T’ pattern to measure SPECT and CT co-registration in three axes. Spatial alignment was evaluated by comparing locations of tube centroids in SPECT and CT reconstructions.

3.2.2 Animal Preparation

Canine studies were approved by the Animal Use Subcommittee of the University of Western Ontario. Ten adult female mongrel hounds were used (typical weight: 20 kg). All canines underwent general anesthesia using propofol induction followed by Isoflurane (1.5-2%) maintenance and mechanical ventilation. Subsequently, during open thoracotomy, canines underwent surgical ligation of the left anterior descending (LAD) coronary artery using a suture placed distal to the first diagonal branch. To provide a representation of both non-reperfused and reperfused myocardial infarction, 4 dogs underwent a permanent ligation of the LAD, while 6 had reperfusion after 2-hours by releasing the ligature.

3.2.3 Cell Preparation

Peripheral blood was harvested from each canine and endothelial progenitor cells (EPCs) were isolated using density gradient centrifugation with Ficoll-Paque PLUS (General Electric, Waukesha, WI). Culture expansion took place over eight-weeks to allow for cell expansion to thirty million cells, as previously described [19, 20]. Cells were then labeled with ^{111}In (0.1 Bq/cell) by incubating them with ^{111}In-tropolone in 37^{0}C Hanks Balanced Salt Solution (HBSS) for 30 minutes [11, 19]. After washing three times with HBSS, the labeled cells were suspended in HBSS in preparation for cell delivery.

3.2.4 Cell Transplantation

Stem cell delivery was performed epicardially and endocardially. Three canines with epicardial injections received the transplanted cells on the day of infarction. These 10 canines were split into two groups consisting of chronic occlusions (1) and reperfused occlusions (2). Endocardial injections were performed on 7 canines, with 4 out of 7 injections at 1-week post-infarction split evenly between chronic and reperfused cases while the rest were performed on the day of infarction consisting of 2 reperfused occlusions and 1 chronic occlusion (table 3.1).

TABLE 3.1: Summary of Transplantation Method

Dog	Arterial Status	Cell Injection Technique
1	Reperfused	Endocardial*
2	Reperfused	Epicardial*
3	Chronic	Epicardial*
4	Chronic	Endocardial†
5	Reperfused	Endocardial†
6	Chronic	Endocardial*
7	Reperfused	Endocardial*
8	Reperfused	Epicardial*
9	Reperfused	Endocardial†
10	Chronic	Endocardial†

* Injections performed on day of infarction
† Injections performed one-week post-infarction

3.2.5 Endocardial Injections

Following femoral cut-down and insertion of a 7-French introducer sheath, the animal was transported to the angiography suite for cell injection. With the animal in a supine position, separate right anterior (30º) and left anterior oblique (60º) contrast ventriculograms (Omnipaque) were obtained using a 6-French pigtail catheter. Endocardial injections were performed using the Stiletto™ Endomyocardial Injection

System (Boston Scientific, Natick, MA) under X-ray fluoroscopic guidance. This system uses a retractable 26 gauge needle which extends beyond its casing with a length of 3.5 mm. The Stilletto catheter is guided to the endocardium inside a 7-French guiding catheter. The guiding catheter tip was advanced to the distal anterior segment of the left ventricle until contact was made with the endocardium. The catheter has a radiopaque marker, which allowed one to determine that the catheter is abutting perpendicular to the endocardial wall. With confirmation of endocardial contact, the Stilletto catheter was advanced to the edge of the guiding catheter, and multiple (8-10) injections within a 1-2 cm diameter zone into the peri-infarct region were performed for each animal, using the wall motion abnormalities seen on the contrast ventriculograms as a guide.

3.2.6 Epicardial Injections

For the epicardial approach, the cells were injected directly into the peri-infarct region (confirmed by visual identification of discoloration and reduced regional wall motion at the epicardial surface) at 8-10 sites within a 1-2 cm diameter zone using a 25-gauge needle. This was done in the same session as the infarction during the thoracotomy.

3.2.7 SPECT/[First-Pass Perfusion CT] Imaging

The animals were transported while under anesthesia to the SPECT/CT suite 30-40 minutes following stem cell injection, and SPECT/CT was acquired immediately using a 6-slice SPECT/CT scanner (Symbia T6, Siemens Healthcare, Erlangen, Germany). The initial SPECT scan consisted of 64-projections at 30s/projection, and a

128x128 image matrix. This was followed by baseline pre-contrast CT at end expiration [21], employing a 2.5mm slice thickness and in-plane resolution of 0.4x0.4mm (130kVP, 15mAs, 15 second acquisition time). A slice thickness of 2.5mm was chosen based upon reduced voxel size requirements for myocardial imaging and to ensure full heart coverage within a single breath hold. A 30mL bolus of 300mgI/mL Omnipaque was then injected through a peripheral vein using a 30mL syringe by hand, with a cardiac-gated, helical-CT performed 5 seconds post-bolus using a Calcium Scoring protocol (Current = 15mAs) [18,20]. On the Siemens Symbia T6 SPECT/CT the only method to perform a gated-CT is to use the pre-defined Calcium Scoring acquisition sequence, which consists of an ECG-gated helical-CT. All CT imaging was performed at end-expiration. Identical follow-up SPECT/CT scans were performed in each of the canines at 4, and 10 days post stem cell injection. An increase in the SPECT projection time per view was made for the day 10 acquisitions to 120 seconds to partially compensate for the physical decay of ^{111}In and anticipated loss of signal due to reduction in cell density at the transplantation site [11].

3.2.8 Dual-Isotope SPECT Imaging

Since SPECT has the capability to image two isotopes simultaneously, it is possible to label cells with ^{111}In-tropolone as previously described, and inject ^{99m}Tc-sestaMIBI for cardiac perfusion imaging. This was done for one canine experiment with a reperfused occlusion and an endocardial injection strategy to compare this technique with that of SPECT/[first-pass perfusion CT] imaging. The same SPECT image acquisition protocol was used as for the day of transplantation.

3.2.9 Validation of First-Pass Perfusion CT using DE MRI

Two additional canines underwent contrast CT and DE MRI imaging on the same day to validate infarct localization using the contrast CT technique. One canine had a reperfused occlusion of the LAD 65 days prior to imaging with the other having a non-reperfused (chronic) ligation of the LAD 67 days prior to imaging. The animals were anaesthetized and first-pass perfusion CT was performed using the previously described technique. They were then directly transported to the MRI suite and had DE MRI performed during the same anesthetic period (2 hours).

DE MRI was performed using a 3-Tesla MRI scanner (VERIO; Siemens Healthcare, Erlangen, Germany) and a 8-element body matrix radiofrequency coil. Cardiac gating was performed using a standard 3-lead system placed over the anterior thorax. Intravenous gadolinium (0.2 mmol/kg Gadobutrol (Gd-BT-DO3A), Bayer Healthcare Pharmaceuticals) was administered by a peripheral vein and DE imaging performed 15 minutes later. A phase-sensitive inversion recovery (PSIR) pulse-sequence (with the inversion time adjusted in the standard fashion [22]) with matrix size 256 X 192 and slice thickness 6 mm, gap 2 mm was used. The slices were taken from the atrioventricular annulus to the apex in the 4, 3 and 2-chamber views.

Infarct location was visually assessed on both the DE MRI images and first-pass perfusion CT images by an experienced investigator [JW]. The presence and transmurality (0 to 100%) of contrast-enhancement (MRI) and hypo-enhancement (CT) was recorded for each myocardial segment using the AHA 17-segment model [23]. Corresponding segmental scores were then compared between the 2 techniques.

3.2.10 Contrast-to-noise ratio (CNR) Calculations

^{111}In SPECT images were corrected for background activity and reconstructed using Ordered Subset Expectation Maximization (OS-EM) (3 iterations, 16 subsets) [24]. Contrast-to-noise ratio (CNR) was calculated for all the imaging sessions (10 canines, 3 imaging sessions each). CNR calculations were done by choosing an ^{111}In volume-of-interest (VOI) for each reconstruction. The ^{111}In VOI was defined to be the pixels greater than 10% of the maximum pixel value in the ^{111}In SPECT reconstruction [25] for each imaging session. Therefore, the ^{111}In VOI was different for each imaging session depending on the maximum pixel value for each particular ^{111}In SPECT reconstruction. The background activity for each session was taken to be 26 VOIs, each VOI being the same size as the ^{111}In VOI for that particular session and directly adjacent to the ^{111}In VOI [25]. This was performed for each imaging session. The CNR for each session was calculated using the following equation [25]:

$$CNR = \frac{^{111}In \quad signal - background}{SD(background)} \tag{3.1}$$

Where ^{111}In signal was equal to the sum of the counts in the ^{111}In VOI, background is the mean of the sum of the counts in each of the 26 background VOIs, and SD(background) is the standard deviation of the sum of the counts inside each of the 26 background VOIs.

3.3 RESULTS

3.3.1 Validation of SPECT and CT Image Co-Registration

A reconstructed isotropic resolution of 11.5mm was observed in the SPECT, and 5.9mm in the CT. Once data is removed from the acquisition system, the SPECT data is

registered to the CT attenuation map, which is a down-sampled version of the high-resolution CT; hence the lower CT resolution. Centroid measurements indicated minimal co-registration error between SPECT and CT data. These measured 1.63mm, 0.24mm, and 1.34mm in the anterior-posterior, left-right, and apical-caudal directions, respectively (See Figure 3.1).

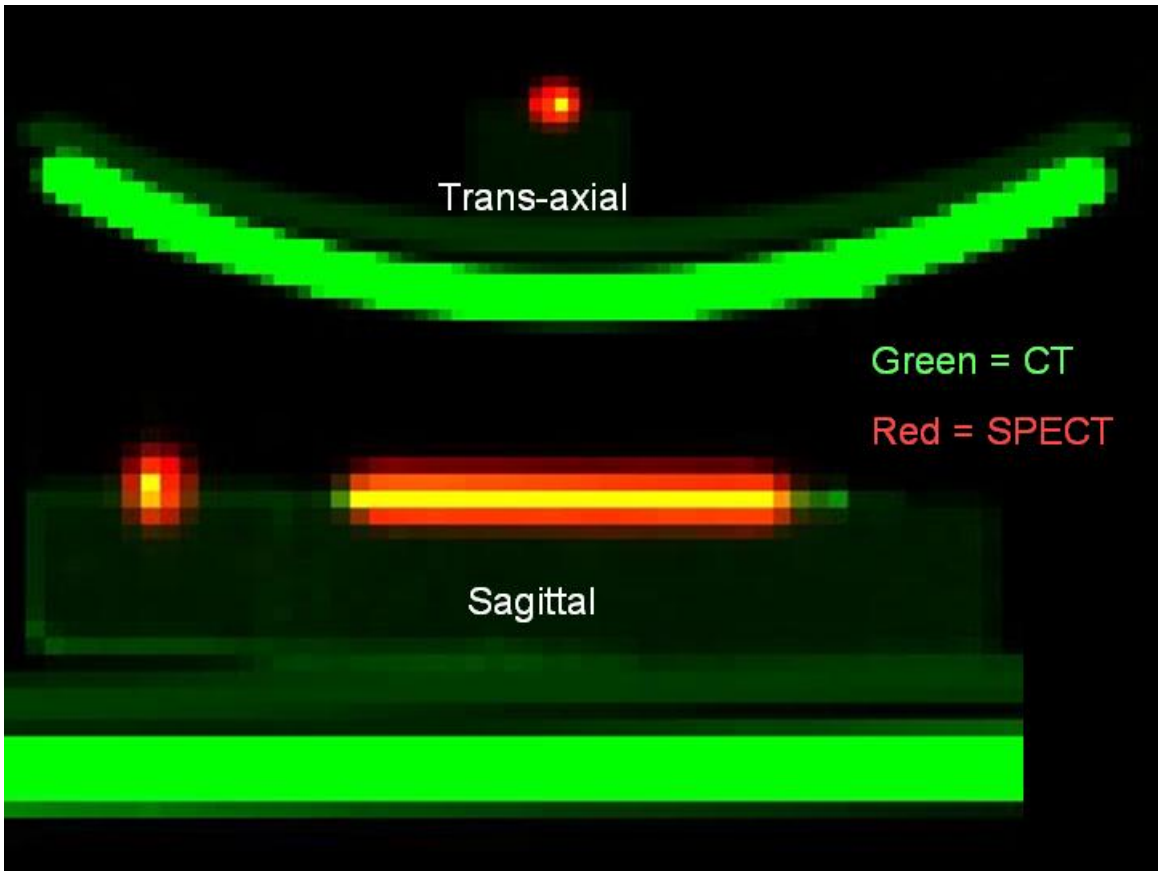

Figure 3.1: SPECT and CT registration

Images displaying both SPECT (RED) and CT (GREEN) reconstructions in the trans-axial (upper image) and the sagital (lower image) planes. The patient table is only CT visible, while the capillary tube phantom is imaged by both SPECT and CT. Notice the near perfect registration between the SPECT and CT (YELLOW).

Canine Infarct Validation Study

All 10 animals completed the study. Examples of both endocardial and epicardial injections are shown in Figures 3.2 and 3.3 respectively.

3.3.2 SPECT/[First-Pass Perfusion CT] Imaging

Baseline SPECT images on the day of cell transplantation demonstrated increased signal in the anterior left ventricular apex in all animals. The ^{111}In-labeling technique was successful in allowing residual signal from retained cells to be visualized for at least 10 days in all animals.

Ten out of 10 (consisting of 30 imaging studies) of the simultaneously acquired first-pass perfusion CT datasets demonstrated regional hypo-enhancement in the distal anterior segments of the left ventricle, consistent with LAD coronary artery vascular distribution.

Fusion of baseline SPECT and first-pass perfusion CT images was successful in all canines. Examples of image fusion are shown in Figures 3.2 and 3.3, each demonstrating successful identification of transplanted stem cells within regions of hypo-perfused myocardium. The location of both the cells and zone of hypo-perfusion (infarction) were clearly visualized on the day of injection, and at all follow-up time points (Figures 3.2 and 3.3). A distinct boundary separating normally perfused vs. reduced flow regions was clearly seen on first-pass perfusion CT studies in all of the imaging studies performed. The ^{111}In focus was visualized consistently at least up to 10

days post cell transplantation, despite a low ^{111}In count rate on day 10 for every animal. For all canines and all imaging sessions, the center of the ^{111}In focus was located within the infarct boundary.

Figure 3.2

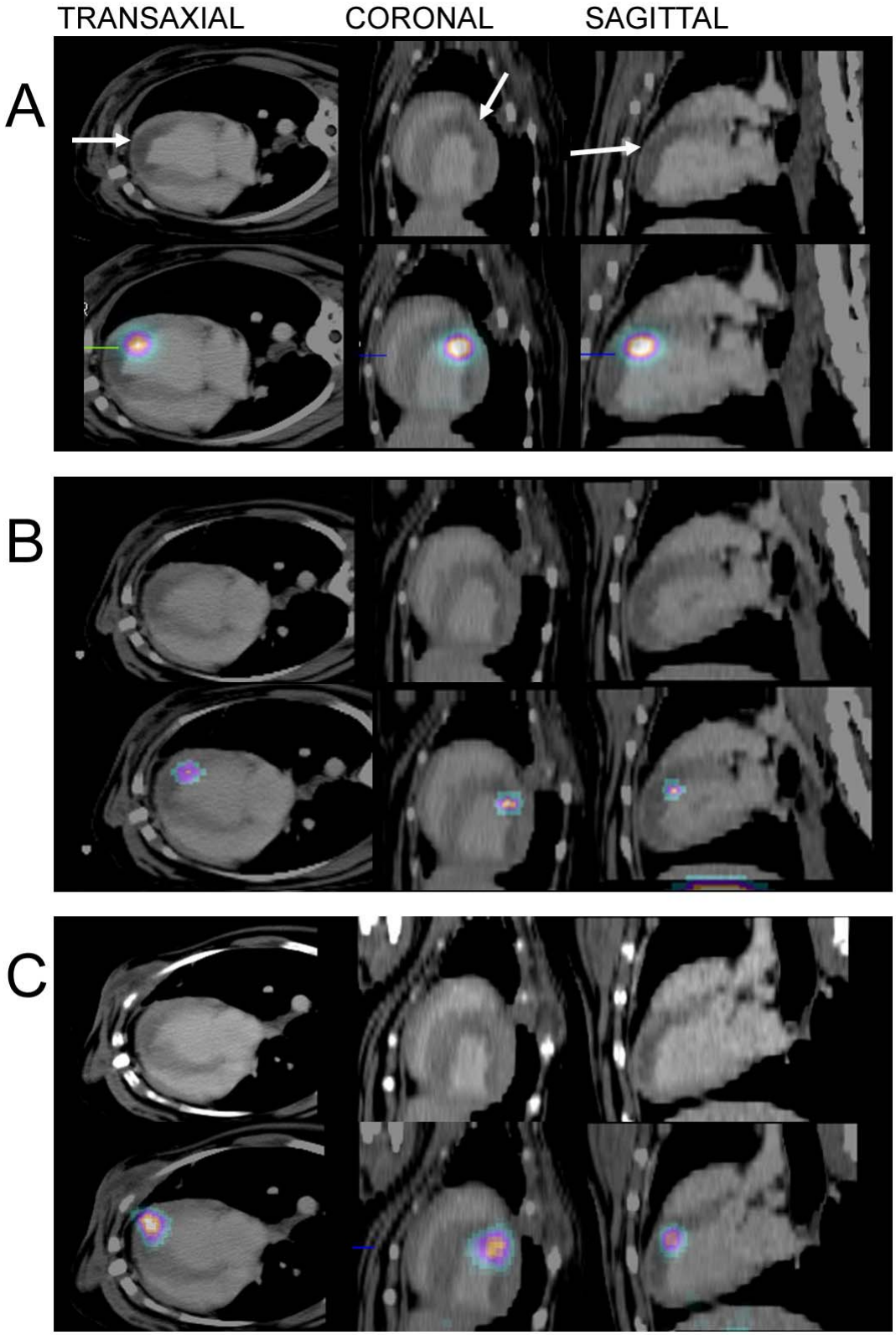

Figure 3.2: Endocardial injection of cells seen on SPECT/[first-pass perfusion CT]

(A) Imaging session on day 0 of endocardial injection (Dog 5: endocardial cell injection 1 week post reperfused occlusion). Top row: Contrast enhanced CT image displaying region of infarction (hypo-enhancement) at the left ventricular apex and extending into the lateral wall. Bottom row: First-pass perfusion CT fused with SPECT displaying location of ^{111}In labeled stem cells near region of infarct. The labeled cells are localized on the inner wall of the left ventricle confirming an endocardial injection.

(B) Day 4 follow-up images taken 4 days post cell transplantation. We notice a weaker signal coming from the cells due to both the physical half-life decay of ^{111}In and clearance of cells from the injection site.

(C) Images acquired 10 days post cell transplantation. Cellular signal is still weak, but a longer imaging session partially compensated for the loss of signal. As well, the area of hypoperfusion seen on CT appears to be both smaller and the contrast between it and normally perfused myocardium is not as marked as on day 0, 1 week post infarct.

Figure 3.3

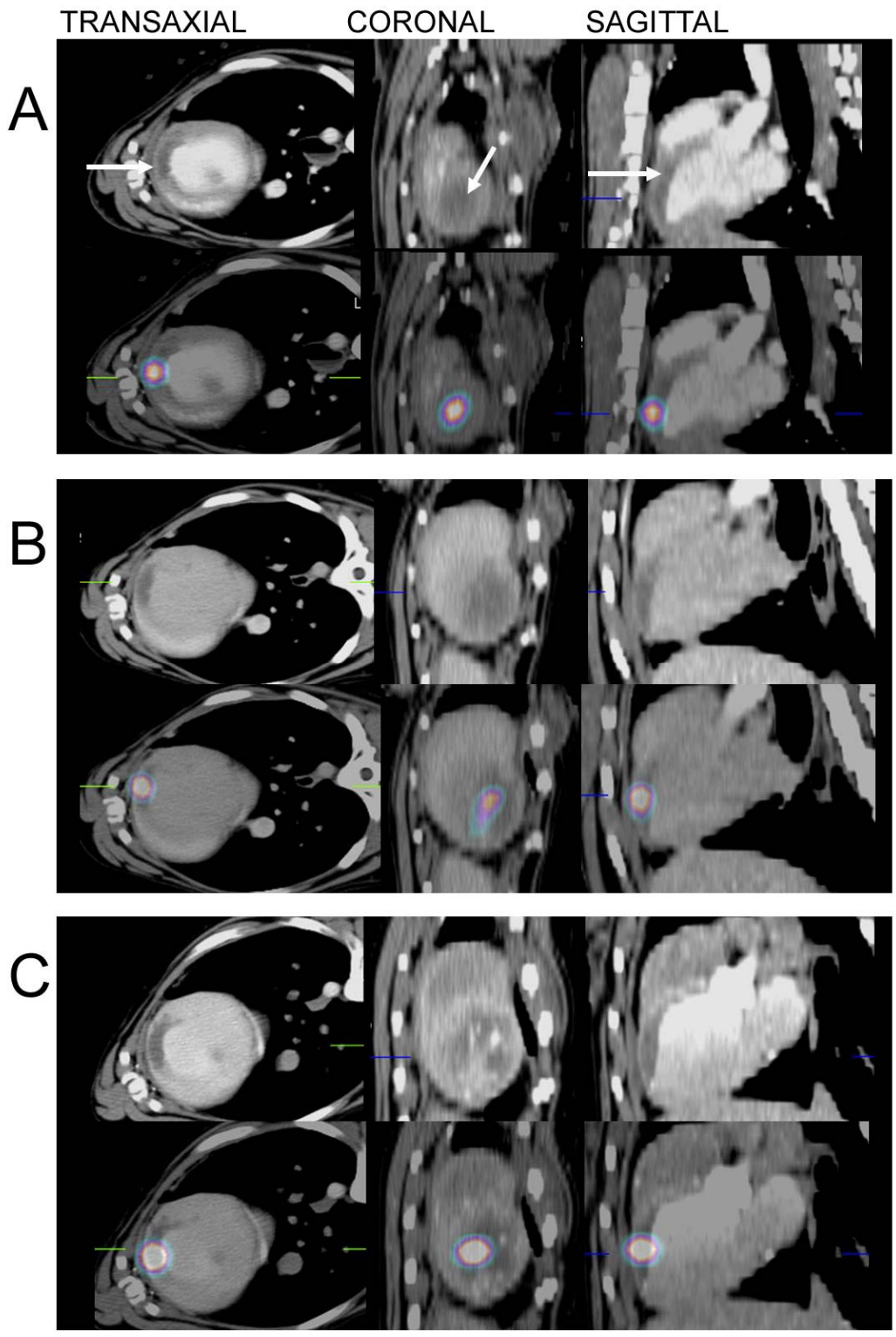

Figure 3.3: Epicardial injection of cells seen on SPECT/[first-pass perfusion CT]

Imaging session on day 0 of epicardial injection (Dog 3: epicardial injection on day of chronic occlusion). Top row: Contrast enhanced CT image displaying region of infarction (hypo-enhancement) at the left ventricular apex and extending into the lateral wall. Since this was a sustained occlusion the infarct can be seen much more clearly than in the animals with reperfusion injury as shown in fig 3.2. Bottom row: First-pass perfusion CT fused with SPECT displaying location of ^{111}In labeled stem cells near region of infarct. The labeled cells were localized on the outer wall of the left ventricle confirming an epicardial injection for this case.

(B) Day 4 follow-up images taken 4 days post cell transplantation.

(C) Day 10 follow-up images acquired 10 days post cell transplantation.

First-pass perfusion CT outlines reduced blood flow, and his region decreased in extent over time from the day of transplantation through to 10 days afterwards. We hypothesize that this is due to augmented collateral flow into the initially hypo-perfused regions in this canine model, with progressive improvement in blood flow into the peri-infarct region. Another explanation for the reduced zone of hypo-enhancement could be that infarct size shrinks over time [26, 27] due to remodeling of the evolving scar.

3.3.3 Dual-Isotope SPECT Imaging

Figure 3.4 compares a dual-isotope SPECT acquisition, with that of SPECT/[First-Pass Perfusion CT]. In dual-isotope SPECT imaging ^{99m}Tc-MIBI shows the cardiac perfusion image while the ^{111}In-tropolone displays the location of the cells that were injected. The spatial resolution was not sufficient to distinguish whether these cells were injected epicardially or endocardially. In addition, it is also more difficult to clearly delineate the zone of reduced blood flow in the cardiac perfusion image using ^{99m}Tc-MIBI. However, using the SPECT/[first-pass perfusion CT] technique the infarct zone was clearly delineated and the location of the cells were located on the inner wall of the left ventricle confirming an endocardial injection.

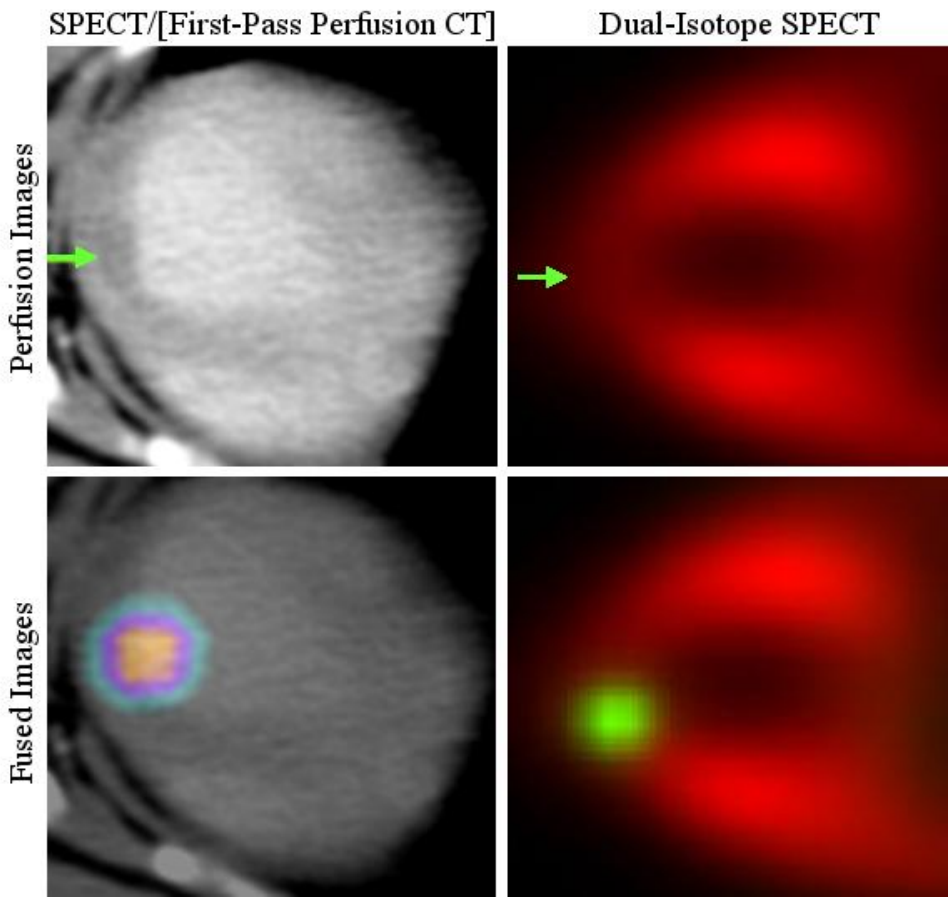

Figure 3.4: Comparing SPECT/[first-pass perfusion CT] with dual isotope SPECT

Case example of endocardial injection of stem cells in a canine model performed 44 days post infarction (reperfused). Cardiac perfusion images performed using first-pass perfusion CT (top left) and ^{99m}Tc-MIBI (top right), demonstrating a region of hypo-perfusion consistent with the infarction territory (arrows). Fused stem cell / perfusion imaging shown using SPECT ^{111}In-tropolone /[First-Pass Perfusion CT] imaging (bottom left) and dual-isotope ^{99m}Tc-MIBI / ^{111}In-tropolone SPECT imaging (bottom right). The improved spatial resolution of the first pass CT perfusion-based fusion image permits a clearer recognition of stem cell delivery to the endocardial border of the myocardial infarction, and the trans-mural immediate contrast provides information regarding the micro flow environment in the region of the transplanted cells.

3.3.4 Validation of First-Pass Perfusion CT using DE MRI

Two canines successfully underwent both first-pass perfusion CT and DE MRI following surgical ligation of the LAD. The reperfused dog had CT hypo-enhancement scored in segments 13 and 14 with transmurality scored at 0-25% and 25-50%, respectively. The corresponding DE MRI images were scored to have enhancement in the same segments with transmurality scores of 25-50% and 50-75%, respectively (Figure 3.5). The non-reperfused (chronic occlusion) dog was scored to have CT hypo-enhancement in segments 7, 13, 14 and 17 of the AHA segmental model, corresponding to the mid anterior, distal anterior, distal septal and apical segments. The transmurality scores for each segment were 25-50% for segment 7, 50-75% for segments 13 and 14 , and 75-100% for segment 17. The corresponding assessment by MRI confirmed enhancement in precisely the same segments with transmurality scores of 50-75% for segment 7 and 75-100% for all remaining segments. (Figure 3.6).

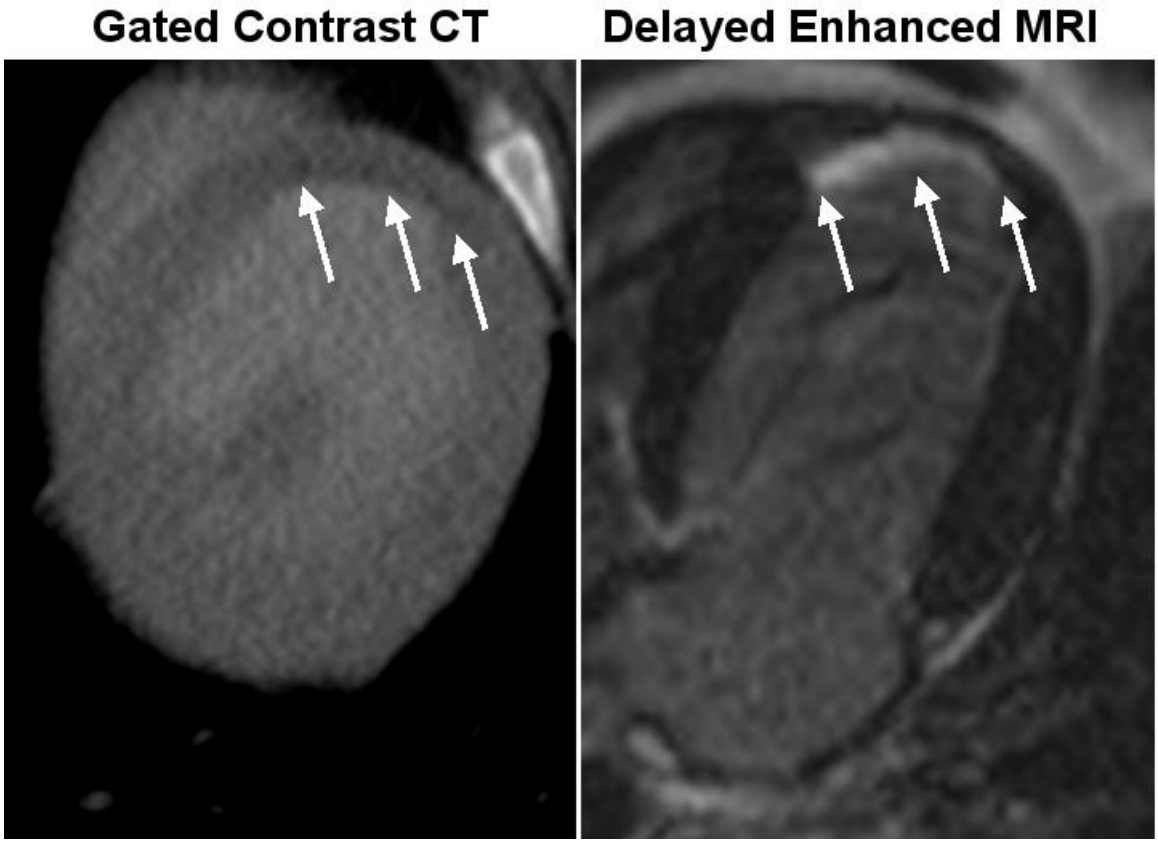

Figure 3.5: Comparing first-pass perfusion CT with delayed-enhanced MRI

Comparison of Contrast enhanced CT (left panel) and delayed enhanced MRI in a dog with a reperfused infarct (Dog 7). Once again, the degree of reduced signal is not as great on CT as is the degree of increased signal seen on the MR images but the smaller area of reduced perfusion in this subendocardial infarct can be identified. The CT hypo-enhancement scores in segments 13 and 14 of the AHA segmental model had transmurality scores of 1 and 2 out of 4, respectively. The corresponding MRI images were scored to have enhancement in the same segments with transmurality scores of 2 and 3 out of 4 respectively, respectively.

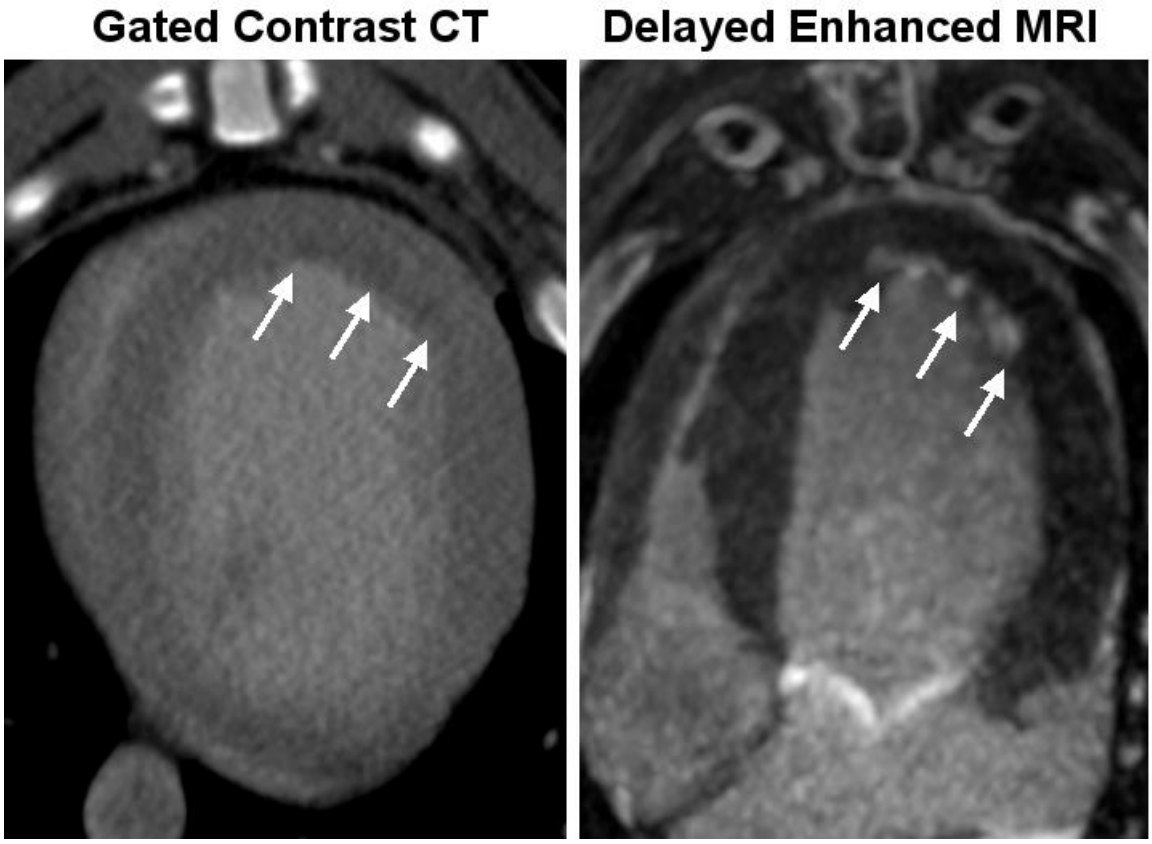

Figure 3.6: Comparing first-pass perfusion CT with delayed-enhanced MRI

Comparison of Contrast enhanced CT (left panel) and delayed enhanced MRI (right panel) in a dog with a chronic occlusion infarct (Dog 4). The degree of reduced signal in the infarct region on the CT images is less than the degree of increased signal seen in the MR image but the hypo-enhanced region is clearly seen (arrows). The CT hypo-enhancement in segments 7, 13, 14 and 17 of the AHA segmental model had transmurality scores of 2, 3, 3 and 3 out of 4, respectively. The corresponding assessment by MRI confirmed enhancement in the same segments with transmurality scores of 3, 4, 4 and 4 out of 4, respectively.

3.3.5 Contrast-to-noise ratio (CNR) Calculations:

The mean and standard error of the mean (SEM) of the natural log of CNR for all 10 canine experiments are shown in figure 3.7. For all imaging sessions the CNR was well above the accepted minimum CNR criterion of 4 (i.e. Rose Criterion [28]). Note that the CNR drops from day 0 to day 4, and then remains relatively unchanged going from day 4 to day 10.

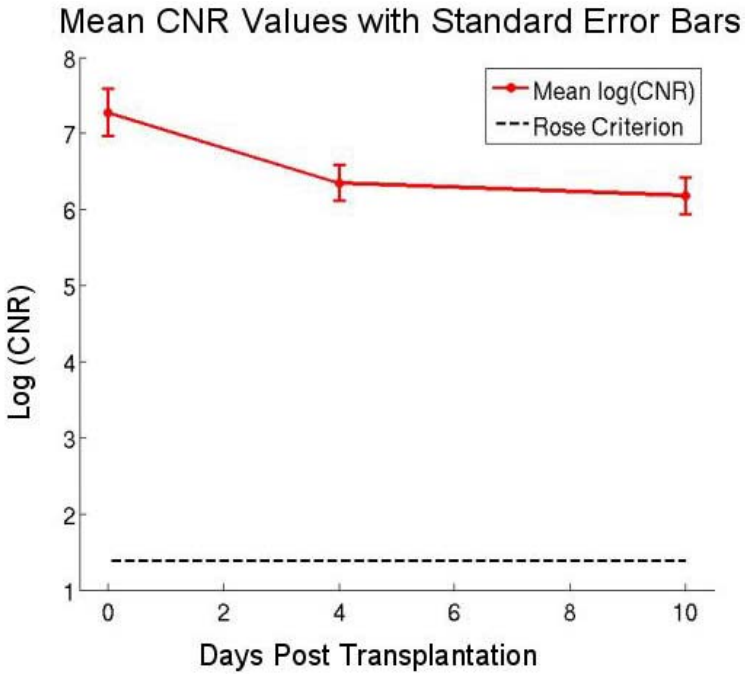

Figure 3.7: CNR analysis

Plot of the average of the natural logarithm of the CNR for 10 dog experiments imaged on day of transplantation of canine endothelial progenitor cells and then at 4 days and 10 days later. Error bars correspond to the SEM. The dashed line near the bottom of the plot corresponds to the *Rose criterion*, the minimum CNR for a signal to be detectable, i.e. CNR=4. SPECT data acquisition time was increased four times on day 10 which reduced the expected drop in CNR as the effective half life of the ^{111}In loss was 2 days. Note that a natural log (CNR) of 6.0 corresponds to a CNR of approximately 400.

3.4 DISCUSSION

This study is the first to demonstrate the feasibility of temporally and spatially localizing TC populations over a 10-day period relative to infarct tissue using a commercially available hybrid SPECT/contrast-CT imaging approach.

A central challenge for the field of cell therapy is the capability to document and monitor TC populations relative to the injured tissue. There continues to be debate with respect to optimal delivery sites relative to recently infarcted tissue. If cells are delivered to the infarct core the marked reduction in perfusion, associated hypoxia, and oxygen free radicals may compromise myocardial regeneration. In contrast, cells placed towards the periphery of infarcted tissue are more likely to produce a therapeutic effect, presumably due to a less hostile environment [29]. While this hypothesis requires further validation, the use of first-pass perfusion CT imaging provides an appropriate means for a qualitative evaluation of myocardial blood flow. Delayed imaging techniques, while attractive for the accurate delineation of full infarct extent, are not appropriate, as they do not define compromised flow within the infarct region. By aiming to deliver stem cells immediately adjacent to, but not within the hypo-perfused infarct core optimal survivability may be obtained.

3.4.1 SPECT/[First-Pass Perfusion CT] in Cellular Imaging

In this study, we report on the use of CT hypo-enhancement following bolus administration of contrast to identify the region of reduced flow. Nieman, et al [12] demonstrated in patients that the extent of this hypo-perfused zone correlates well with

regions of contrast enhancement using contrast-CT or DE MRI, the latter of which is validated for measuring the extent of infarction [7]. In this study, it was confirmed that the hypo-enhanced site detected by CT is within the infarct boundary as determined by DE MRI. In the two animals, the transmural extent of the zone of hypo-enhancement was smaller on CT imaging than the zone of enhancement on MRI, consistent with this representing the infarct core where myocardial blood flow is most diminished [17].

SPECT/contrast-CT demonstrated very good registration accuracy (~1mm) using phantom experiments. However, these experiments were performed on a non-moving phantom. Visual inspection of the in vivo canine fused SPECT/contrast-CT images was performed by an experienced investigator [GW] and the injection strategy was determined 70% of the time. Therefore, cells injected in outer wall (epicardial injection) could be distinguished from those injected in the inner wall (endocardial injection). This implies that the registration accuracy is still sufficient even during in-vivo imaging.

3.4.2 Hybrid Imaging for Cell Localization

This study introduces another application for CT in hybrid SPECT/CT. CT can be used to provide spatial localization of myocardial infarction in addition to providing general anatomic localization and SPECT attenuation correction. Stodilka et al [30] have shown that a high-resolution CT signal can improve the ability to localize and quantify a relatively weak SPECT signal with low-resolution. Thus we expect that, in the case of cell transplantation, as the SPECT signal decays over time due to physical decay and/or washout of cells, the CT can be used to aid in SPECT quantification. It is true that SPECT can be used to image multiple isotopes and ^{99m}Tc perfusion imaging may be used

instead of CT perfusion to locate regions of reduce blood flow. However, relying upon SPECT alone would not provide sufficient spatial resolution to clearly delineate the zone of reduced blood flow as well as the co-registered contrast-CT. Additionally, the use of ^{111}In requires imaging with a medium energy collimator, which will further reduce the spatial resolution of the ^{99m}Tc perfusion SPECT scan.

It could be argued that the introduction of PET/MRI would replace this application of SPECT/CT, given the increased sensitivity of PET and the reduction of ionizing radiation [31]. To-date the preferred PET isotope for cell localization is ^{64}Cu [9]. 3D-PET with ^{64}Cu has approximately a 20-fold greater sensitivity than SPECT with ^{111}In; however, this advantage is lost by a two week time period due to physical half-life differences [32]. Interestingly evidence to date suggest that the limits of radio-label in Bq/cell are similar for ^{64}Cu [9] and ^{111}In [25], hence increasing the sensitivity of ^{64}Cu/PET by increasing the ^{64}Cu load per cell is not an option.

3.4.3 Contrast-to-Noise Ratio

This average CNR curve (figure 7) can be used to predict how far out transplanted cells can be followed. ^{111}In labeled canine EPCs have been shown to have an approximate effective half-life of 2 days (combining both biological and physical decay of ^{111}In [11, 20]). The average CNR decreases from day 0 to day 4. Since imaging time was constant from day 0 to day 4 a decrease in CNR is expected due to the physical and biological decay of the ^{111}In labeled cells. However, the change in CNR from day 0 to day 4 is less than expected for an effective half-life of two days. The signal in the ^{111}In VOI does decrease with a 2-day half-life; however, the background and

the SD of background are significantly lower at 4 days increasing the CNR [25]. The background is higher at day 0 as within hours following cell transplantation a significant fraction of the cells leave the transplantation site. These cells have a biological half-life in the region surrounding the transplant site of approximately 20 hours [11]. Hence, by day 4 they are mostly cleared resulting in the observed reduction in background, and SD of background resulting in increasing the CNR. After day 4, the background activity and SD of background activity remains constant, and the change in CNR from day 4 to day 10 has undergone decay from 3 half lives. However, imaging time was increased by a factor of 4, which compensated for approximately half of the decay. If we maintain a consistent imaging time after day 10, we would theoretically be capable of imaging transplanted cells for a period of 22 days (i.e. 11 two day effective half-lives), before the CNR drops below the *Rose Criterion* provided the background and SD of background do not increase. This trend is similar to cardiac chest phantom experiments conducted by Jin et al [25]. However, to properly image TCs up to 22 days, the cell location must be known beforehand, and this can be accomplished with the aid of CT imaging [25, 30].

3.4.4 Risk to Patient

For the case of our CT imaging, the dose is relatively low, with a computed tomography dose index volume (CTDIvol) of 3.9 mGy. With the settings used on our CT scanner this would produce an effective radiation dose to the patient of around 0.7mSv [33]. This radiation dose would produce a cancer rate of 5.6×10^{-5}, while the spontaneous cancer rate for a general population is 8.4×10^{-1} [34]. The risk associated

with CT contrast agents similar to the one used in this study is nephrotoxicity (renal toxicity), which has a prevalence in the general population of 0.9% [35].

3.4.5 Study Limitations

The SPECT/CT registration experiment was performed on a non-moving phantom. We chose to use a breath-hold CT acquisition at end-expiration for the canine experiments since recent clinical trials have shown this to be the optimal phase of the respiratory cycle for best image registration in SPECT/CT for the purpose of attenuation correction [21]. We recognize that the SPECT and CT data were not acquired under identical conditions since the SPECT data is averaged over multiple respiratory phases in a step and shoot manner, while the CT data was collected in a continuous rotation during a single phase of the respiratory cycle [36]. This is a challenge in hybrid SPECT/CT imaging; not only for image fusion but also for attenuation correction and this should be addressed in more detail in a future study. In our experiments, the animals were ventilated, and the CT data acquisition occurred at the end-expiration phase of the respiratory cycle. They were ventilated at a rate of 8 breaths per minute, and for 70% of the respiratory cycle the canines were at functional residual capacity (FRC). Therefore, we expect the SPECT data to be averaged more closely to the end-expiration phase of the respiratory cycle and hence the end-expiration CT that was acquired. Application to patients is expected to be straightforward. Provided the patients can hold their breath during the CT acquisition for 15 seconds at FRC and can maintain normal tidal breathing during the SPECT portion.

The canines were not sacrificed, and were used in subsequent experiments; therefore, no follow-ups were conducted on the canines post-mortem to determine the effects of the cell transplantation. A previous study in our lab used this technique to compare the survival of the cells following the two injection strategies [20].

3.5 CONCLUSIONS

This study demonstrates the feasibility of hybrid SPECT/first pass perfusion CT imaging for the spatial localization of transplanted stem cells relative to infarcted myocardial tissue. The combination of a diagnostic quality CT on the hybrid platform allows the determination of the ^{111}In signal with transmural resolution, which is not possible using multi-spectral SPECT methods.

3.6 REFERENCES

1. Wollert KC, Drexler H. Clinical applications of stem cells for the heart. *Circ Res* 2005;96:151-163.

2. Beeres SLMA, Bengel FM, Bartunek J, Atsma DE, Hill JM, Vanderheyden M, et al. Role of imaging in cardiac stem cell therapy. *JACC* 2007;49(11):1137-1148.

3. Blackwood KJ, Sabondjian E, Goldhawk DE, Kovacs MS, Wisenberg G, Merrifield P, et al. Progress in Stem Cell Applications: Chapter V: Towards Image-Guided Stem Cell therapy. 2008 Nova Publishers, Inc.

4. Hinds KA, Hill JM, Shapiro EM, Laukkanen MO, Silva AC, Combs CA, et al. Highly efficient endosomal labeling of progenitor and stem cells with large magnetic particles allows magnetic resonance imaging of single cells. *Blood* 2003;102:867-872.

5. Kraitchman DL, Heldman AW, Atalar E, Amado LC, Martin BJ, Pittenger MF, et al. In vivo magnetic resonance imaging of mesenchymal stem cells in myocardial infarction. *Circulation* 2003;107:2290-2293.

6. Chen IY, Greve JM, Gheysens O, Willmann JK, Rodriguez-Porcel M, Chu P, et al. Comparison of optical bioluminescence reporter gene and superparamagnetic iron oxide MR contrast agent as cell markers for noninvasive imaging of cardiac cell transplantation. *Mol Imaging Biol*. 2009 May-Jun;11(3):178-87.

7. Kim RJ, Wu E, Rafael A, Chen EL, Parker MA, Simonetti O, et al. The use of contrast-enhanced magnetic resonance imaging to identify reversible myocardial dysfunction. *N Engl J Med* 2000 Nov;343(20):1445-1453.

8. Hofmann M, Wollert KC, Meyer GP, Menke A, Arseniev L, Hertenstein B, et al. Monitoring of bone marrow cell homing into the infarcted human myocardium. *Circulation* 2005;111:2198-2202.

9. Huang J, Lee CCI, Sutcliffe JL, Cherry SR, Tarantal AF. Radiolabeling rhesus monkey $CD34^{+}$ hematopoietic and mesenchymal stem cells with ^{64}Cu-Pyruvaldehyde-Bis(N4-Methylthiosemicarbazone) for microPET imaging. *Mol Imaging* 2008; 7(1):1-11.

10. Kraitchman DL, Tatsumi M, Gilson WD, Ishimori T, Kedziorek D, Walczak P, et al. Dynamic imaging of allogeneic mesenchymal stem cells trafficking to myocardial infarction. *Circulation* 2005;112:1451-1461.

11. Blackwood KJ, Lewden B, Wells RG, Sykes J, Stodilka RZ, Wisenberg G, Prato FS. In vivo SPECT quantification of transplanted cell survival following engraftment using 111In-tropolone in infarcted canine myocardium. *J Nucl Med* 2009;50(6):927-935.

12. Nieman K, Shapiro MD, Ferencik M, Nomura CH, Abbara S, Hoffmann U, et al. Reperfused myocardial infarction: contrast-enhanced 64-slice CT in comparison to MR imaging. *Radiology* 2008;247(1):49-56.

13. Diesbourg LD, Prato FS, Wisenberg G, Drost DJ, Marshall TP, Carroll SE, et al. Quantification of myocardial blood flow and extracellular volumes using a bolus injection of Gd-DTPA: kinetic modeling in canine ischemic disease. *Magn Reson Med.* 1992;23(2):239-253.

14. Mahnken AH, Bruners P, Katoh M, Wildberger JE, Gunther RW, Buecker A. Dynamic multi-section CT imaging in acute myocardial infarction: preliminary animal experience. *Eur Radiol*. 2006;16(3):746-752.

15. Rochitte CE, Lima JA, Bluemke DA, Reeder SB, McVeigh ER, Furuta T, et al. Magnitude and time course of microvascular obstruction and tissue injury after acute myocardial infarction. *Circulation* 1998;98(10):1006-1014.

16. Rubinshtein R, Miller TD, Williamson EE, Kirsch J, Gibbons RJ, Primak AN. Detection of Myocardial Infarction by Dual-Source Coronary Computer Tomography Angiography Using Quantitated Myocardial Scintigraphy as the Reference Standard. *Heart*. 2009;95(17):1492-1422.

17. Wu KC, Zerhouni EA, Judd RM, Lugo-Olivieri CH, Barouch LA, Schulman SP, et al. Prognostic Significance of Microvascular Obstruction by Magnetic Resonance Imaging in Patients With Acute Myocardial Infarction. *Circulation* 1998;97:765-772.

18. Holz A, Lautamaki R, Sasano T, Merrill J, Nekolla SG, Lardo AC, Bengel FM. Expanding the versatility of cardiac PET/CT: feasibility of delayed contrast enhancement CT for infarct detection in a porcine model. *J Nucl Med*. 2009;50(2):259-265.

19. He H, Shirota T, Yasui H, Matsuda T. Canine endothelial progenitor cell-lined hybrid vascular graft with nonthrombogenic potential. *J of Thorac and Cardiovasc Surg* 2002;126(2):455-464.

20. Mitchell AJ, Sabondjian E, Sykes J, Deans L, Zhu W, Lu X, Feng Q, Prato FS, Wisenberg G. Clearance Kinetics After Subendocardial or Subepicardial Injections of Endothelial Progenitor Cells in a Canine Myocardial Infarction Model. *J Nucl Med.* 2010; 51(3):413-417.

21. Utsunomiya D, Nakaura T, Honda T, Shiraishi S, Tomiguchi S, Kawanaka K, et al. Object-specific attenuation correction at SPECT/CT in thorax: optimization of respiratory protocol for image registration. *Radiology* 2005; 237:662-669.

22. Kim RJ, Shah DJ, Judd RM. How we perform delayed enhancement imaging. *J of Cardiovasc Magn Reson* 2003 Jul;5(3):505-514.

23. Cerqueira MD, Weissman NJ, Dilsizian V, Jacobs AK, Kaul S, Laskey WK, et al. Standardized myocardial segmentation and nomenclature for tomographic imaging of the heart: a statement for healthcare professionals from the Cardiac Imaging Committee of the Council on Clinical Cardiology of the American Heart Association. *Circulation* 2002 Jan;105(4):539-542.

24. Hudson HM, Larkin RS. Accelerated image reconstruction using ordered subset of projection data. *IEEE Trans Med Imaging.* 1994;13(4): 601-609.

25. Jin Y, Kong H, Stodilka RZ, Wells RG, Zabel P, Merrifield PA, et al. Determining the minimum number of detectable cardiac-transplanted 111In-tropolone-labelled bone-marrow-derived mesenchymal stem cells by SPECT. *Phys Med Biol* 2005;50(19):4445-4455.

26. Wisenberg G, Lekx K, Zabel P, Kong H, Mann R, Zeman PR, et al. Cell tracking and therapy evaluation of bone marrow monocytes and stromal cells using SPECT and CMR in a canine model of myocardial infarction. *J Cardiovasc Magn Reson*. 2009 Apr 27;11(1):11.

27. Fieno DS, Hillenbrand HB, Rehwald WG. Infarct resorption, compensatory hypertrophy, and differing patterns of ventricular remodeling following myocardial infarctions of varying size. *J Am Coll Cardiol.* 2004 Jun 2;43(11):2124-31

28. Rose A. Vision: Human and Electronic. New York: Plenum; 1973: 21-23.

29. McCue JD, Swingen C, Feldberg T, Caron G, Kolb A, Denucci C, et al**.** The real estate of myoblast cardiac transplantation: negative remodeling is associated with location. *J Heart Lung Transplant.* 2008 Jan;27(1):116-123.

30. Stodilka RZ, Blackwood KJ, Prato FS. Tracking transplanted cells using dual-radionuclide SPECT. *Phys Med Biol* 2006;51:2619-2632.

31. Rahmim A, Zaidi H. *Nucl Med Commun*. 2008;29(3):193-207.

32. Bettinardi V, Mancosu P, Danna M, Giovacchini G, Landoni C, Picchio M, et al. Two-dimensional vs three-dimensional imaging in whole body oncologic PET/CT: a Discovery-STE phantom and patient study. *Q J Nucl Med Mol Imaging*. 2007 Sep;51(3):214-223.

33. Morin RL, Gerber TC, McCollough CH. Radiation Dose in Computed Tomography of the Heart. *Circulation* 2003;107:917-922.

34. Monson RR, Cleaver JE, Abrams HL, Bingham E, Buffler PA, Cardis E, et al. Beir VII: Health Risks from Exposure to Low Levels of Ionizing Radiation. Report in brief prepared by the National Research Council. Available at: National Academies Press, 500 Fifth Street, NW, Washington, DC 20001; 800-624-6242; www.nap.edu.

35. Liss P, Persson PB, Hansell P, Lagerqvist B. Renal failure in 57 925 patients undergoing coronary procedures using iso-osmolar or low-osmolar contrast media. *Kidney International*. 2006;70:1811-1817.

36. Sabondjian E, Lewden B, Prato FS, Stodilka RZ. Gated Cardiac SPECT/CT: Slow CT or Fast CT? *J Nucl Med.* Meeting Abstracts. 2008 May;49:64P.

CHAPTER 4: SMALL FIELD-OF-VIEW CARDIAC SPECT CAN BE IMPLEMENTED ON HYBRID SPECT/CT PLATFORMS WHEREIN DATA ACQUISITION AND RECONSTRUCTION ARE GUIDED BY CT[1]

4.1 INTRODUCTION

Image truncation in nuclear medicine is an increasing problem. Current reconstruction techniques introduce errors into the image if the activity distribution extends beyond the detector field-of-view (FOV) [1]. Truncation in Single Photon Emission Computed Tomography (SPECT) can arise from several different reasons. The first can be the natural evolution to improve SPECT detectors to incorporate more expensive solid-state technology and reducing field-of-view (FOV); secondly, data acquisition of large patients can cause the projections to be truncated; and lastly, the use of converging collimator geometries in SPECT.

Solid-state detectors may achieve better energy and spatial resolution as well as enhance image contrast [2, 3]. Solid-state detectors demonstrated visual superiority and improved quantitative accuracy for SPECT compared with Anger type cameras [4]. However, the primary detractor to the acceptance of solid-state technology is high cost both for raw material and fabrication. Consequently, in an effort to reduce cost, several groups have explored the concept of using small detectors [5, 6]. The challenge associated with reduced detector size is object truncation.

Data acquisition of large patients also produces object truncation in reconstructed images. Lalush and Tsui [1] evaluated the MLEM iterative algorithm [7] and its

[1] The contents of this chapter have been published as: Sabondjian E, Stodilka RZ, Belhocine T, King ME, Wisenberg G, Prato FS. Small field-of-view cardiac SPECT can be implemented on hybrid SPECT/CT platforms where data acquisition and reconstruction are guided by CT. *Nuclear Medicine Communications* 2009;30(9):718-726. It is reproduced with permission from the publishers.

accelerated derivatives, OS-EM [8] and RBI-EM [9] under circumstances of extreme truncation using the MCAT digital phantom. They suggested a simple modification to the algorithm to substantially reduce truncation, but concluded that extreme truncation had to be avoided.

Finally, truncation also occurs when performing SPECT with converging collimators [5]. Gullberg et al [10] introduced a reconstruction algorithm to correct for ring artifacts from image truncation when performing cone beam tomography of the heart. Zeng et al [11, 12] discuss the use of fan-beam and cone-beam collimators with varying focal lengths to minimize the effects of truncation. A new reconstruction algorithm was developed for such a collimator and has shown promise in reducing truncation artifacts. Chang et al [5] proposed a method for local SPECT using a cylindrically-arranged array of small gamma cameras whose FOVs are focused onto a 13.5 – 18.5 cm diameter central region-of-interest (ROI), sacrificing adequate sampling over the object periphery for improved sensitivity in the central ROI. In a subsequent paper, the group hypothesized that the severity of artifacts is related to the amount of radiotracer present outside the central ROI, and used computer simulations to show errors of approximately 4-10% with a ^{99m}Tc-MIBI tracer when comparing truncated data to non-truncated data [9].

Many authors have studied truncation artifact reduction in radioisotope emission [5, 13] and transmission imaging [14, 15, 16, 17, 18]. Additionally, Defrise et al [19] present a theoretical analysis for reconstructing a small ROI from highly truncated data. Many of the techniques for reduction of transmission artifacts rely on *a priori* knowledge of the body contour, and their accuracy improves with the accuracy of the measured body

contour [20]. Given that solid-state detectors may be clinically realized in the context of hybrid SPECT/CT [21], and SPECT/CT is gaining popularity without increasing patient dose to unacceptable levels [22], we anticipate that a likely imaging scenario will involve the coupling of severely truncated SPECT data and non-truncated CT. In this case, a priori knowledge of the body contour available via CT may be useful in helping reconstruct a truncated SPECT data set.

In this paper, we investigate the concept of SPECT/CT assuming highly truncated SPECT as might be expected when using small FOV detectors or converging geometries, in conjunction with a non-truncated CT. Tomographic sampling is characterized using the concept of crosstalk, introduced by Gifford and Barrett [23]. Additionally, we investigate a simple modification to the OS-EM algorithm that significantly reduces artifacts when the object contour is known, which may be obtained from CT. The modified algorithm was previously evaluated in canine studies [24]; in this paper we demonstrate its application in a cardiac chest phantom and a series of 14 clinical cardiac patients [25]. The modified algorithm is evaluated by comparing its performance using truncated data with the performance of standard OS-EM using non-truncated data. The comparison is in terms of: relative quantification both for large regions-of-interest and individual voxels, as well as impact on defect size.

4.2 METHODS

4.2.1 Proposed System

Figure 4.1 is an example of a system that incorporates a small FOV gamma camera. In this system, the X-ray CT is acquired first and reconstructed. The operator then positions onto the X-ray CT image a circular ROI (cylindrical across multiple trans-axial slices) delineating the scanning area where SPECT measurements are to be obtained. The diameter of the ROI is determined by the gamma camera FOV in the transaxial plane which, for the purpose of the present study, is taken to be 16cm. The position of the ROI determines the trajectory of the gamma camera, which is constrained by the requirement to always face the ROI throughout its orbit. The orbit may include tangential translation in the transaxial plane if the center of the ROI is not coincident with the X-ray CT FOV center. The gamma camera is then tasked to acquire its data. A similar approach has been demonstrated by Rahmim et al [26], which incorporated a converging collimator design.

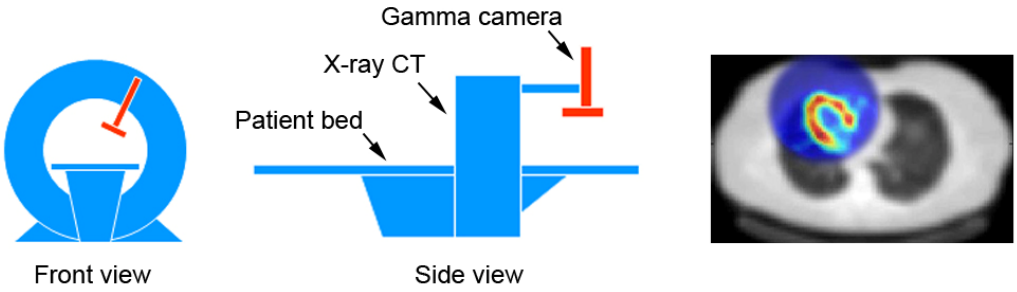

Figure 4.1: The proposed system

Side and front views of the proposed small FOV SPECT/CT system. The right figure is an example of the SPECT/CT acquisition that would be achievable.

4.2.2 Sampling Theory

The forward imaging problem can be expressed as Y = AX, where Y is the projection data wherein gamma ray measurements are binned to provide counts y_t in sinogram element t; A is the transition matrix comprised of elements a_{tj} representing the probability that an emission from voxel j is recorded at t, and X is the radiotracer distribution comprised of elements x_j.

In reducing the size of the FOV, the sampling pattern will be altered drastically, leading to changes in sensitivity and resolution. To characterize these changes, we used the cross-talk concept, originally developed by Gifford and Barrett [23] to study sampling patterns in the Fourier domain. Following [27] we adapt this concept to the spatial domain. The spatial cross-talk matrix is defined as [27]: $H = A^T A$, where T indicates matrix transpose. The diagonal elements of H represent the sensitivity of the sampling pattern to any voxel, and rows of H represent the degree of aliasing between any two voxels resulting from inadequate sampling.

For the purpose of calculating H, we used a simplified transition matrix derived from a radon transform of a single slice, without modeling attenuation, scatter, or detector response to isolate the characteristics of tomographic sampling. The radon transform of the single slice was modeled in accordance with our experimental data acquisition, described in the following section.

4.2.3 Image Reconstruction

Our phantom and patient data were acquired on a two head Infinia-Hawkeye-4 slice (General Electric Healthcare, Waukesha WI, USA). Data was sampled

tomographically over 120 uniformly spaced projections (60 steps per head). The original 34x34cm FOV gamma camera projections were truncated to simulate a small 16x16cm FOV gamma camera acquisition, where the orbit was selected to focus on the heart. Examples of a complete FOV and a truncated FOV sinogram are shown in figure 4.2 for a clinical ^{99m}Tc-MIBI scan. The size of the SPECT sinogram matrix is chosen as if a full FOV gamma camera is being used; this representation illustrates clearly the truncated locations. A typical human chest is approximately 30cm across, therefore as demonstrated in figure 4.2 a large portion of the data will be truncated.

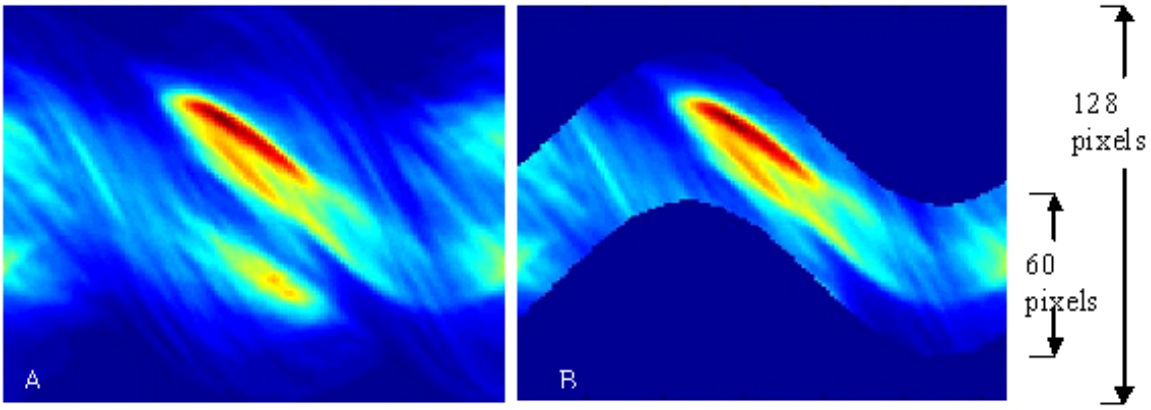

Figure 4.2: Displaying truncated projection data

(A) Complete FOV sinogram. (B) Truncated sinogram to simulate small gamma camera.

The ROI, delineated on the X-ray CT as previously described, is then re-sampled to the SPECT coordinate frame and projected into an empty matrix such that the spatial and angular coordinates of the projection pixels have a one-to-one correspondence with coordinates of the SPECT sinogram matrix. The sinogram of the ROI is then thresholded to create a binary mask, which demarcates coordinates within the ROI where gamma camera measurements were acquired (binary value of 0), and coordinates outside of the

ROI, which are also beyond the FOV of the gamma camera (binary value of 1). SPECT data is then reconstructed using the OS-EM algorithm of Hudson and Larkin [8], modified slightly to explicitly show truncated regions in the SPECT sinogram matrix. The modified OS-EM algorithm can be written in two parts as:

Forward projector:

$$\mu_t^k = \sum_{j=1}^{J} a_{tj} x_j^k \,, \tag{4.1}$$

Back-projector and update:

$$x_j^{k+1} = \left(\frac{x_j^k}{\sum_{t \varepsilon S_n} a_{tj}} \right) \sum_{t \varepsilon S_n} a_{tj} \left[\left(\frac{y_t}{\mu_t^k} \right) (1 - m_t) + m_t \right], \tag{4.2}$$

where gamma-ray measurements are binned to provide counts y_t in sinogram elements t; the expected number of gamma-ray emissions from voxel j is denoted by x_j, with its estimate after the k^{th} iteration denoted as x_j^k. The elements a_{tj} represent the probability that an emission from voxel j is recorded at t; which is derived from a model of gamma-ray propagation through tissue, which in the present case included non-uniform attenuation. S_n denotes a subset of the sinogram elements grouped into those corresponding to a set of gamma camera gantry positions. The final factor in square brackets in equation (4.2) includes the mask vector with elements m_t corresponding to elements of the measured sinogram y_t. For all $m_t = 0$, this factor reduces to the ratio of measured and re-projected data (i.e. y_t/μ_t^k). In this case equations (4.1) and (4.2) together

reduce to the well-known OS-EM algorithm. For all $m_t = 1$, the final factor reduces to unity. In other words, when $m_t = 1$, the corresponding x_j's are not updated. The re-projected data is considered unmeasured [1], rather than measured as 0 (as in regular OS-EM). Theoretically, the truly correct way to model truncation is to set appropriate terms in the transition matrix 'A' to zero; however, this is already known [1] and results in artifacts under conditions of extreme truncation [1]. The algorithm is initialized using *a priori* knowledge of the object support, available from X-ray CT. Thus, the X-ray CT reconstruction is re-sampled to the SPECT voxel coordinate frame, the patient table is deleted; and all x_j^0 (i.e. 0^{th} iteration) are set to 1 within the object support, and to 0 otherwise.

4.2.4 Phantom Study

An anthropomorphic torso phantom (model ECT/TOR/P, Data Spectrum Corp., Hillsborough NC, USA) was filled with 444MBq of ^{99m}Tc. The cardiac insert with the standard defects supplied were placed in the apex and septal wall of the left ventrical. The activity ratios in heart: soft tissue: liver were set to 7: 1: 3, where the ratios were determined from SPECT/CT clinical scans at our center. The acquisition time was set so that 10,000 counts/projection was recorded in the first projection, which is typical and was generally observed in clinical cardiac rest scans.

The data was reconstructed in three different ways: (1) Using non-truncated data and standard reconstruction (gold standard - NTOSEM). (2) Using truncated data and standard reconstruction (TOSEM). (3) Using truncated data and the modified reconstruction (TMOSEM)

4.2.5 Clinical Study

In addition to the phantom study, we evaluated our method in a series of fourteen patients (8 male, 6 female, mean age = 65 +/- 13 years, mean BMI = 32 +/- 5) who underwent SPECT/CT myocardial perfusion imaging (MPI) under a rest/stress 1-day protocol. For this paper we analyzed the rest SPECT/CT studies, which were performed on patients 45 minutes after an injection of approximately 370MBq of ^{99m}Tc-MIBI. Among the patient group, 8 patients had a definitely normal study and 6 patients had a definitely abnormal study after SPECT/CT - MPI using the QGS/QPS software (Cedars-Sinai Medical Center, Los Angeles, CA, USA).

4.2.6 Image Analysis

Voxel-by-Voxel Analysis

Performance of the modified OS-EM algorithm was evaluated on a voxel-by-voxel basis. This was done by calculating the Pearson correlation coefficient for TOSEM vs NTOSEM; and TMOSEM vs NTOSEM, for each patient and the phantom, for voxels within the reconstructed region of interest (ROI). We report the mean ± standard deviation of the correlation coefficients for the group of patient data. Also, we include example difference images and scatter plots showing the voxel-by-voxel relationship between TOSEM vs NTOSEM; and TMOSEM vs NTOSEM. Calculations were performed using MATLAB (The MathWorks, Natick, Massachusetts, USA). To determine the impact of activity outside the reconstructed ROI on correlation

coefficients: we calculate the ratio of activity within the reconstructed ROI to activity outside the reconstructed ROI, and compared this ratio with the correlation coefficients.

Count Ratios

The cardiac images were aligned manually into standard orientations and a central coronal slice of the heart was chosen by an experienced operator [T.B.]. Three ROIs were drawn: (A) Apex, (B) Lateral Wall, and (C) Septal Wall of the left ventricle (see figure 4.4). Each ROI was circular and had a diameter of 2cm. The location of the ROIs were consistent for each patient. Ratios were calculated (A/B, B/C, and A/C) for each reconstruction: NTOSEM, TOSEM, and TMOSEM. For each ratio the percent error, equation (4.3), was calculated and averaged for each patient.

$$\frac{\left|Ratio(Truncated) - Ratio(Gold)\right|}{Ratio(Gold)} \times 100 = \text{Percent Error}, \qquad (4.3)$$

Ratios of normal and abnormal myocardium were both used. The goal of the analysis was not to study the actual ratio value, but rather to compare the ratios of the truncated projections to that of the gold standard.

Defect Size Comparison

The resting defect size was determined by the thresholding technique [28], using a cutoff of 2.5 standard deviations below the mean of a group of normal patients to define the perfusion defect. The defect size was determined using an in-house program. The size of the defect within the whole heart seen in the two truncated reconstructions (TOSEM, TMOSEM) was compared to that of the gold standard (NTOSEM) giving a relative percent error.

$$\frac{Defect(Truncated) - Defect(Gold)}{Defect(Gold)} \times 100 = \text{Relative \%Error}, \qquad (4.4)$$

4.3 RESULTS

4.3.1 Sampling Theory

The diagonal elements of the crosstalk matrix (H) can be sorted into an image to visualize sensitivity (see Fig 4.3A). For the case of the truncated FOV, the sensitivity within the ROI varied by -/+1%; indicating that sensitivity is relatively uniform in this region. This is also illustrated quantitatively in Fig 4.3D which is a profile across the ROI from Fig 4.3A. The rows of H can also be sorted into an image showing the aliasing between voxels as shown in Figure 4.3B.

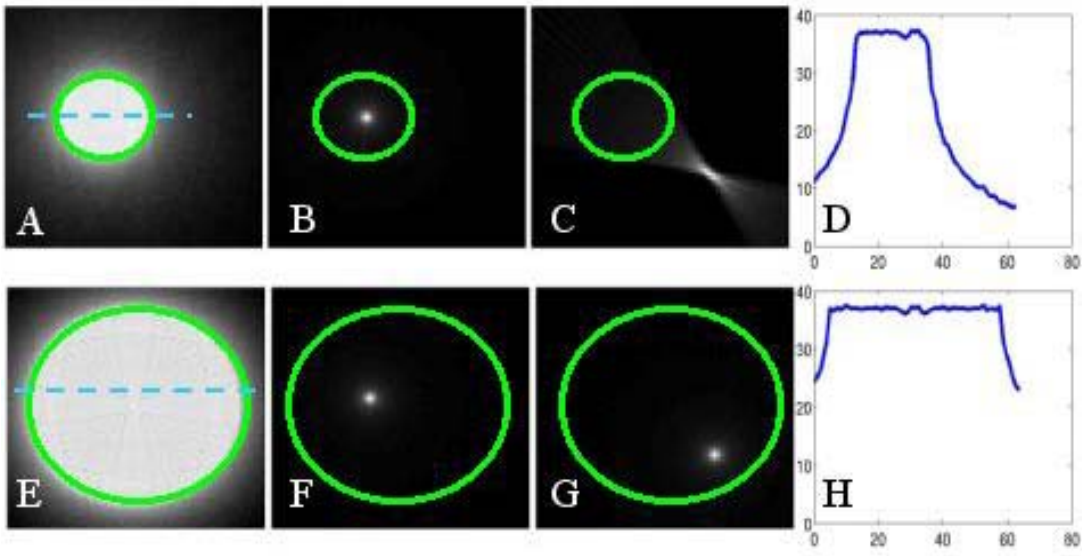

Figure 4.3: The sampling theory for large and small FOV gamma camera imaging

Top row is for truncated FOV, bottom row is for non-truncated FOV. Diagonal elements of H sorted into an image to visualize sensitivity across a transaxial plane (A, E). The circular region represents the region of interest (ROI), with a diameter equal to the gamma camera FOV, where sensitivity is maximized. Rows of H sorted into an image showing aliasing from a voxel within the ROI into nearby voxels (B, C, F, G). Image (B) shows a relatively isotropic point-spread function with little aliasing. Image (C) shows aliasing from a voxel beyond the ROI into nearby voxels, showing considerable anisotropic aliasing. Together (B) and (C) indicate spatially variant resolution when the FOV is small. Profiles across the dashed lines at the center of the sensitivity plots (D, H). This demonstrates that sensitivity does not change going from small FOV to larger FOV gamma cameras in the ROI.

4.3.2 Clinical Study

Figure 4.4 displays three clinical acquisitions and one phantom acquisition. All examples are reconstructions of a region of interest (ROI) around the heart with trans-axial slices being displayed.

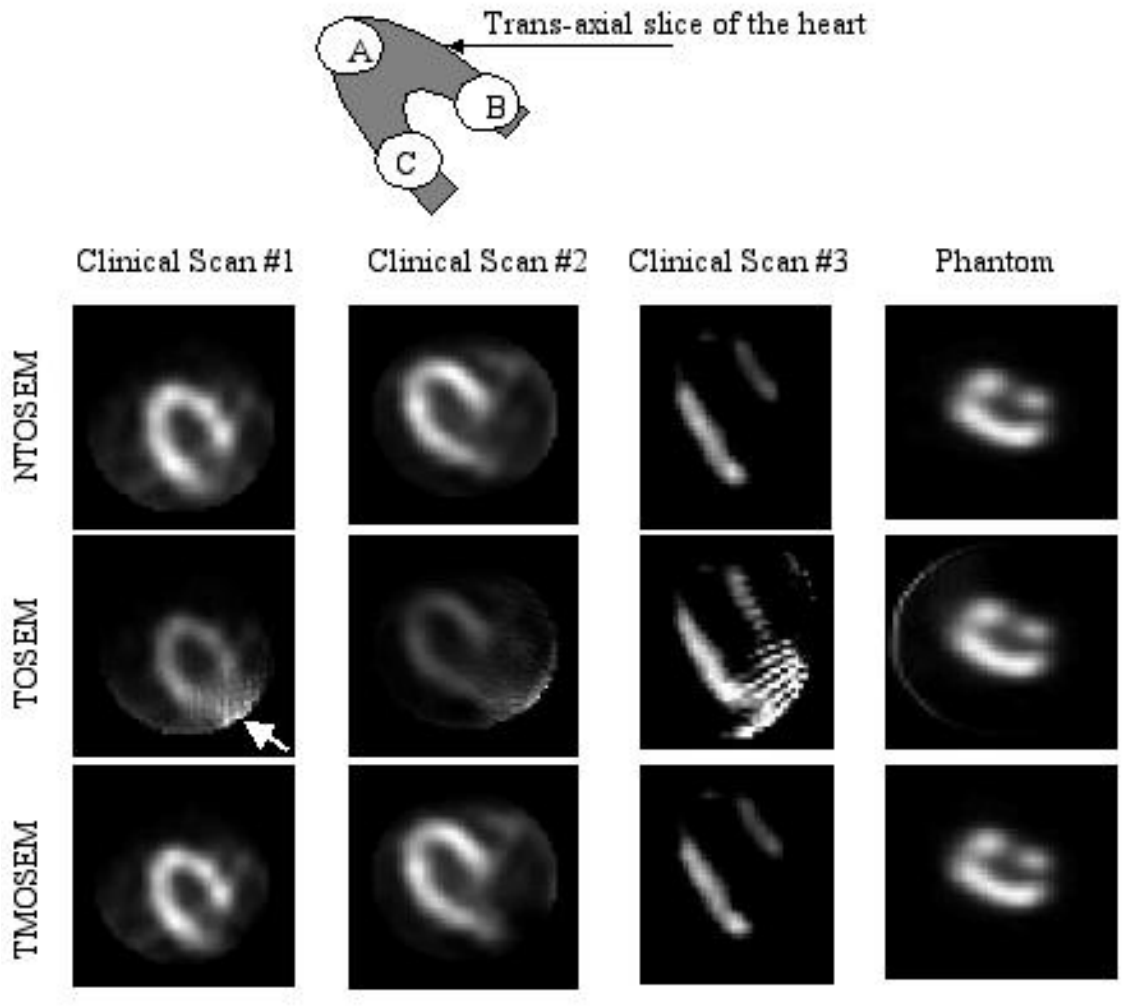

Figure 4.4: Clinical and phantom results

Diagram displaying location of ROIs chosen for ratio analysis shown on top. Left ventricle displayed for three clinical patients and the phantom study (trans-axial view). Hot rim artifacts are seen when using TOSEM (shown with arrow in scan #1). Scan #3 had a significant perfusion defect, which becomes obscured when using TOSEM. In general, observation of the ROI around the heart shows the loss of cardiac signal with TOSEM; however, the signal is properly recovered when using TMOSEM.

4.3.3 Image Analysis

Figure 4.5 shows scatter plots of the reconstructed counts with the heart that are associated with clinical scan #1 and scan #2 in figure 4 when compared to NTOSEM. For clinical scan #1, comparing TMOSEM with NTOSEM, the correlation coefficient was found to be 0.996; whereas when comparing TOSEM with NTOSEM, the correlation coefficient was found to be 0.734. On average for the 14 patients the correlation coefficient was 0.991 -/+0.008 when comparing TMOSEM with NTOSEM, and 0.609 -/+0.130 when comparing TOSEM with NTOSEM. The correlation coefficients for the phantom study were 0.999 and 0.996 when comparing TMOSEM and TOSEM with NTOSEM, respectively.

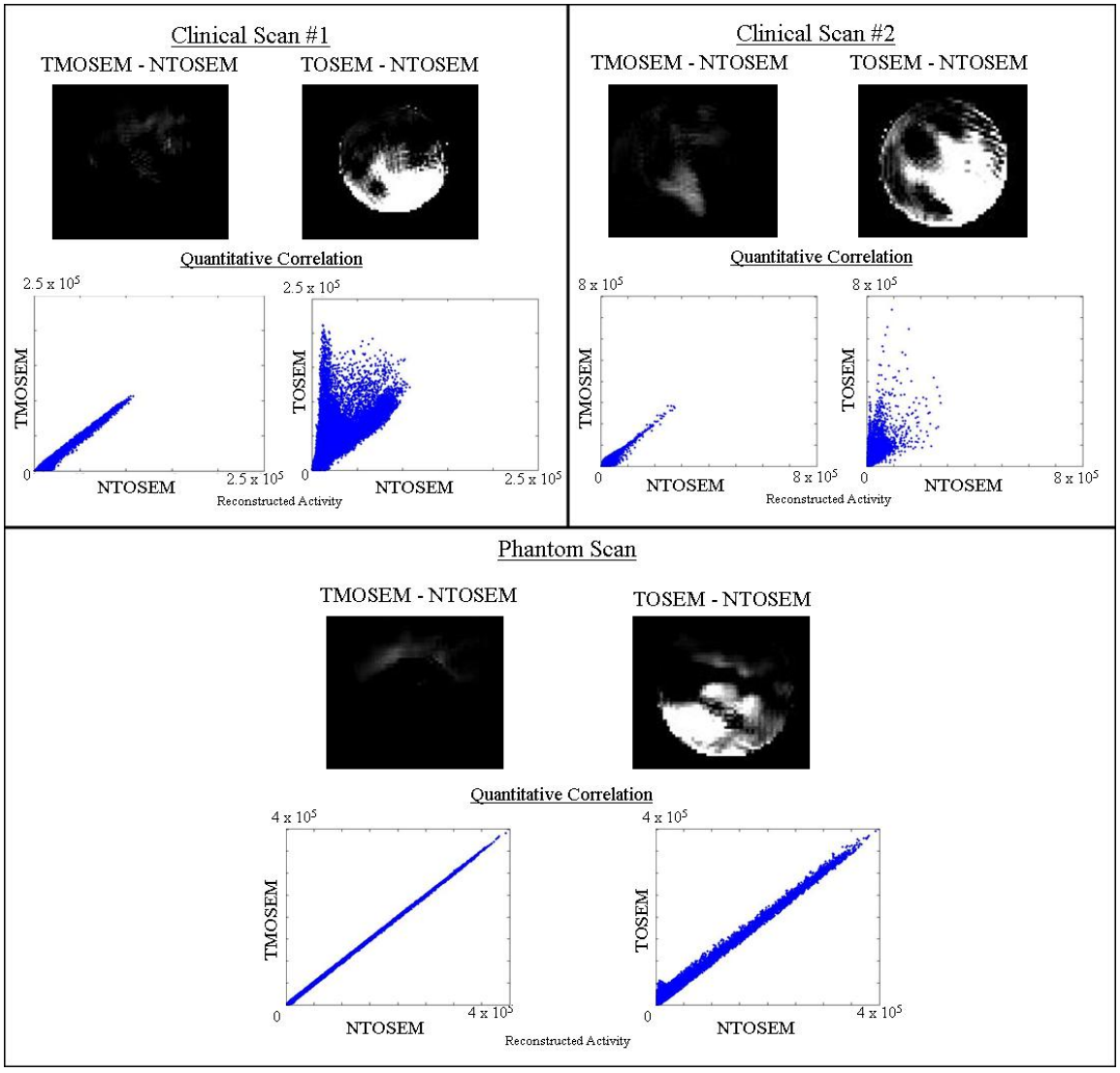

Figure 4.5: Scatter plots

Difference images and scatter plot showing the voxel-by-voxel correlation between TMOSEM and NTOSEM as well as TOSEM and NTOSEM for clinical scan #1 and scan #2 in figure 4, and the phantom study. The difference images and scatter plots only consider the counts within the reconstructed ROI.

The similarity in correlation coefficients for the phantom study may be related to the phantom having a higher ratio of activity within the reconstructed ROI to activity outside the reconstructed ROI, compared with the same ratio in clinical scenarios. Further, it was seen that the correlation coefficients of the patient data were related to this ratio. For example, as the ratio of activity within the reconstructed ROI to activity outside the reconstructed ROI decreased, the correlation coefficients decreased. This is shown in Table 4.1.

Table 4.1: Relationship between background activity and correlation coefficients

	TOSEM vs NTOSEM Correlation Coefficient	TMOSEM vs NTOSEM Correlation Coefficient	Reconstructed ROI / Background
Phantom	0.996	0.999	0.90
Clinical Scan #1	0.734	0.996	0.36
Clinical Scan #2	0.658	0.984	0.28

Count Ratio and Defect Size Analysis

Severe truncation led to large errors in count ratios between different heart regions. Table 4.2 shows that these errors for clinical data were on average larger than 100% when reconstructing using TOSEM. Use of TMOSEM resulted in an average error of 8.9%, which is a substantial improvement. A similar improvement was noted for the phantom data. In the case of defect size analysis, severe truncation of data led to an average error of 17% for the clinical data. This error was reduced to 0.19% when data was reconstructed via TMOSEM (See Table 4.3).

Table 4.2: Error between count ratios compared to gold standard (NTOSEM)

COUNT RATIO ANALYSIS	Clinical Data			Phantom Data
	Min. Error	Max. Error	Average Error	Average Error
TOSEM	19.3%	>100%	>100%	>100%
TMOSEM	1.7%	17.4%	8.9%	4.3%

Table 4.3: Percent error of defect size compared to gold standard (NTOSEM)

DEFECT SIZE ANALYSIS	Clinical Data		
Relative Difference	Min. Error	Max. Error	Average Error
TOSEM	9.56%	24.62%	17.13%
TMOSEM	0.0%	0.46%	0.19%

4.4 DISCUSSION

In this manuscript, we used the cross-talk concept to evaluate the tomographic sampling characteristics of highly truncated SPECT. This analysis was independent of reconstruction algorithm, and is fundamental to the geometry of data acquisition. Cross-talk analysis demonstrated that imaging with a small FOV gamma camera results in non-uniform sensitivity across the trans-axial plane. However, it is uniform within a small ROI corresponding to the size of the gamma camera FOV. This was demonstrated in figure 3A, where the sensitivity was at its highest level within the ROI and gradually decreased away from the ROI. Also, it was observed that within the ROI the resolution was isotropic, while it was highly anisotropic outside the FOV (figures 4.3B and 4.3C). The aliasing is consistent with the gamma camera sampling pattern. Areas within the ROI are always seen by the gamma camera, leading to circularly symmetric point spread functions. However, areas outside the ROI are seen only during limited arcs as the gamma camera rotates. Consequently, these areas featured elongated point spread

functions along dimensions that were under sampled. As indicated in the methods section, we used a simplified transition matrix to isolate the effects of imaging geometry. In practice, the transition matrix 'A' is much more complex, being dependent upon the physical effects such as the object scatter and attenuation, and the depth dependent resolution effects for the collimator on the object being imaged. Future work could explore the calculation of the crosstalk matrix using a Monte Carlo derived transition matrix evaluating the effects of attenuation, scatter, and collimator response.

Using TOSEM resulted in the appearance of a hot rim artifact in the reconstructed images, which is seen commonly when projections are truncated. This is because the OSEM algorithm, in many implementations, constrains the radioactivity to remain within the boundaries of the truncated projection data. The OSEM algorithm is programmed to count all activity that is measured to be within the FOV of the camera causing the hot rim artifact. The reconstruction method of equations 4.1 and 4.2 relax this constraint and use the body contour information provided by the full FOV X-ray CT to effectively eliminate artifacts within the reconstructed FOV. This was demonstrated in figures 4.4 and 4.5, the scatter plot analysis for all patients, the count ratio analysis given in table 4.2 and the infarct size analysis given in table 4.3, when using TMOSEM compared to NTOSEM. In the case of the phantom study, the differences seen were not as great. This, we speculate, is due to comparatively less background activity injected around the cardiac insert of the torso phantom. With less activity in the area outside the reconstructed ROI, there is less probability of image interference when analyzing the reconstructed ROI. When analyzing the relationship between the ratio of counts in the reconstructed ROI to counts outside the reconstructed ROI and the correlation between TOSEM vs NTOSEM, we

discovered that the said count ratio decreased as the correlation decreased. In other words, the performance of the conventional OSEM algorithm deteriorated. Note that the performance of the modified OSEM algorithm, TMOSEM, also deteriorated, but not to the same extent. It is important to note that there is no standard method for compensating for truncation in clinical systems, and manufacturers may take differing approaches [1]. For the sake of clarity here, we delineate explicitly the method of equations 4.1 and 4.2, which is simple to implement and extremely flexible in dealing with complex gamma camera orbits.

When simulating acquisitions by a 16x16 cm FOV gamma camera, and comparing the ratio of counts within the heart and the change in defect size, the average errors using TMOSEM compared to NTOSEM were 8.9% and 0.19% respectively in our patient population. The difference in defect size comparing TMOSEM and NTOSEM was less than 1%. The errors when comparing count ratios are significantly less when using TMOSEM as opposed to TOSEM; however, a maximum error of 17.4% is high for many applications. Future work could focus on better understanding the impact of TMOSEM outside the FOV and the role scattered activity originating outside of the FOV contribute information inside the reconstructed FOV. Also, the optimization of the number of subsets and iterations of the modified OSEM could be studied. Future experiments could also focus on better understanding of how background noise will effect the reconstruction and the effect of the location and size of the ROI in the reconstruction.

4.5 CONCLUSION

The topic of truncation and its management has always been important, and will likely grow with the potential benefits of solid state detectors which may decrease the size of gamma detectors, the increase in imaging of larger patients, using converging geometries in collimation, and the need of hotspot imaging to follow radio-labeled transplanted cells. In this work we have demonstrated that significantly truncated SPECT data compromises tomographic sampling, yielding non-uniform sensitivity and a non-stationary anisotropic resolution. However, we also demonstrated in phantom and clinical cardiac data that within a small region that is sampled adequately, the truncated data can be largely restored back to its original non-truncated form via a simple modification to the OS-EM algorithm when non-truncated CT is available.

4.6 REFERENCES

1. Lalush DS, Tsui BMW. Performance of ordered-subset reconstruction algorithms under conditions of extreme attenuation and truncation in myocardial SPECT. *J Nucl Med.* 2000;41:737-744.

2. Heanue JA, Brown JK, Tang HR, Hasegawa BH. A bound on the energy resolution for quantitative SPECT. *Med Phys.* 1996;23(1):169-173.

3. Darambara DG, Todd-Pokropek A. Solid state detectors in nuclear medicine. *QJ Nucl Med.* 2002;46(1):3-7.

4. Mori I, Takayama T, Motomura N. The CdTe detector and its imaging performance. *Ann Nucl Med.* 2001;15(6):487-494.

5. Chang W, Liu J, Yu D, Loncaric S. A cylindrical geometry for cardiac SPECT imaging. *IEEE TNS*. 1996;43(4):2219-2224.

6. Zeng GL, Gagnon D, Natterer F, Wang W, Winkler M, Hawkins W. Local tomography property of residual minimization reconstruction with planar integral data. *IEEE TNS.* 2003;50(5):1590-1594.

7. Shepp LA, Vardi Y. Maximum Likelihood Reconstruction for Emission Tomography. *IEEE TMI.* 1982;MI-1(2):113-122.

8. Hudson HM, Larkin RS. Accelerated image reconstruction using ordered subset of projection data. *IEEE Trans Med Imaging*. 1994;13(4): 601-609.

9. Byrne CL. Block-iterative methods for image reconstruction from projections. *IEEE Trans Imag Proc.* 1996;5:792-794.

10. Gullberg GT, Christian PE, Zeng GL, Datz FL, Morgan HT. Cone beam tomography of the heart using single-photon emission-computed tomography. *Invest Radiol.* 1991;26(7):681-688.

11. Zeng GL, Gullberg GT, Jaszczak RJ. Fan-Beam Reconstruction Algorithm for a Spatially Varying Focal Length Collimator. *IEEE TMI.* 1993;12(3):575-582.

12. Zeng GL, Gullberg GT. Iterative and analyitical reconstruction algorithms for varying-focal-length cone-beam projections. *Phys Med Biol*. 1998;43:811-821.

13. Yu DC, Chang W, Pan TS. A study of reconstruction accuracy for a cardiac SPECT system with multi-segmental collimation. *IEEE TNS.* 1997;44(3):1403-1408.

14. Manglos SH. Truncation artifact suppression in cone-beam radonuclide transmission CT using maximum likelihhod techniques: evaluation with human subjects. *Phys Med Biol.* 1992;37(3):549-562.

15. Pan TS, King MA, Penney BC, Rajeevan N, Luo DS, Case JA. Reduction of truncation artifacts in fan beam transmission by using parallel beam emission data. *IEEE TNS.* 1995;42(4):1310-1320.

16. Zeng GL, Gullberg GT. An SVD study of truncated transmission data in SPECT. *IEEE TNS.* 1997;44(1):107-111.

17. Gregoriou GK, Tsui BMW, Gullberg GT. Effect of Truncation Projections on Defect Detection in Attenuation-Compensated Fanbeam Cardiac SPECT. *J Nucl Med.* 1998;39(1):166-175.

18. Pan TS, Tsui BMW, Byrne CL. Choice of Initial Conditions in the ML Reconstruction of Fan-Beam Transmission with Truncated Projection Data. *IEEE TMI.* 1997;16(4):426-438.

19. Defrise M, Noo F, Clackdoyle R, Kudo H. Truncated Hilbert transform and image reconstruction from limited tomography data. *Inverse Problems.* 2006;22:1037-1053.

20. Gullberg GT, Zeng GL Datz FL, Christian PE, Tung CH, Morgan HT. Review of convergent beam tomography in single photon emission computed tomography. *Phys Med Biol.* 1992;37(3):507-534.

21. Jansen FP, Venderheyden JL. The future of SPECT in a time of PET. *Nuclear Medicine and Biology.* 2007;34:733-735.

22. Tonge CM, Fernandez RC, Harbinson MT. Current issues in nuclear cardiology. *The British Journal of Radiology.* 2008;81:270-274.

23. Barrett HH, Gifford H. Cone-beam tomography with discrete data sets. *Phys Med Biol.* 1994;39:451-476.

24. Stodilka RZ, Blackwood KJ, and Prato FS. Large Animal Hybrid SPECT/CT using a Small Field-of-view Gamma Camera: Proof of Principle for Monitoring Cardiac Transplanted Stem Cells [abstract]. *Soc Molec Imag.* 2006 (ID#: 766).

25. Sabondjian E, Stodilka RZ, Belhocine T, King M, Prato FS. Small Field-of-View (FOV) SPECT/CT for Cardiology: Theory and Preliminary Clinical Evaluation [abstract]. *IEEE NSS-MIC.* 2007 (ID#: M13-257).

26. Rahmim A, Zaidi H. PET versus SPECT: strengths, limitations and challenges. *Nuclear Medicine Communications.* 2008;29(3):193-207.

27. Qi J, Huesman H. Wavelet crosstalk matrix and its application to assessment of shift-variant imaging systems. *IEEE TNS.* 2004;51:123-129.

28. DePuey EG, Garcia EV, Berman DS. *Cardiac SPECT imaging.* Philadelphia PA: Lippincott Williams & Wilkins; 2001:42-52.

CHAPTER 5: CONCLUSIONS

5.1 Summary of Results

An important goal in myocardial stem cell therapy is the development of tools to determine the location of transplanted stem cells and assess their viability. This thesis demonstrated that a form of medical imaging technology – SPECT/CT – has the potential to achieve this goal. Three aspects of SPECT/CT application to monitoring cardiac stem cell therapy were evaluated: comparing two popular models of SPECT/CT systems, evaluating use of contrast-enhanced CT in SPECT/CT to improve transplanted stem cell localization, and exploring the potential for small field-of-view gamma cameras in SPECT/CT.

There are currently two popular SPECT/CT systems that are commercially available. One incorporates a slow rotation CT (GE Infinia/Hawkeye-4), while the other incorporates a fast rotation CT (Siemens Symbia/T6). To date there have been no publications comparing the two systems for attenuation correction in cardiac SPECT perfusion imaging, and therefore indicating which SPECT/CT system would be better suited for imaging cells. Our computer simulations showed an improvement in RMS error comparing SPECT cardiac polar plots using a fast rotation CT attenuation map as opposed to a slow rotation CT attenuation map. Canine experiments also showed an advantage of using a fast rotation CT. Improvements in RMS error and correlation coefficient were recorded for all canines when analyzing a central trans-axial slice of the heart when using a fast rotation CT attenuation map.

An important aspect of monitoring cardiac stem cell therapy is determining the location of transplanted cells relative to the region of reduced blood flow. To this end, we developed a technique combining SPECT with cardiac gated first-pass perfusion CT, which is only possible when using a fast rotation CT, and evaluated it in a canine model of heart disease. Our technique was capable of localizing the transplanted cells in relation to the region of reduced blood flow. In addition, viability is also important in imaging transplanted cells, but before viability can be assessed, the period of time that cells can be followed had to be determined. A CNR analysis was performed on the SPECT/CT system and results showed that cells can be followed for up to a period of 22 days if the location of the cells is known, which is possible with the fused first-pass perfusion CT and SPECT imaging technique. To image cells for an even longer period of time post-transplantation, improvements to the sensitivity of gamma camera imaging systems would be required. Such an improvement might be achieved via solid-state detector technology.

Several groups and manufacturers have begun to explore a "next generation" of gamma cameras wherein the scintillation crystal and photomultiplier tube combination is replaced with a solid-state semiconductor detector. One challenge to the implementation of solid-state detectors is their very high cost. For cardiac imaging, these high costs might be lessened by using small detectors that are sufficient in size to image the heart. However, in this scenario, the presence of radioactivity outside the heart introduces artifacts into the reconstructed SPECT images that compromise quantification. In the case of cardiac imaging, we demonstrated that imaging with a small field-of-view detector can introduce errors in relative quantification in the heart of over 100%. We

introduced a new reconstruction algorithm that substantially reduced these artifacts and reduced errors to less than 10%.

5.2 Future Work

As this field is still fairly new, there are many interesting avenues to investigate. To begin, the NCAT phantom in Chapter 2 can be manipulated to simulate both male and female anatomies in addition to different body types (from very thin to very obese). Currently, only the male anatomy in a standard body type was employed by us. Repeating our investigations using the female anatomy and more body types may further generalize our results in comparing slow and fast CT attenuation maps in SPECT. In addition to body type, the NCAT phantom can include cardiac motion which was not modeled in the current experiments. Regarding the canine imaging aspect: it might be beneficial to compare more SPECT/CT systems such as the design introduced by Phillips.

For the experiments in chapter 3, a standardized delivery system using an automated power injector, rather than hand-injection for the contrast agent will help in the ability to better quantify the results obtained from the first-pass perfusion CT imaging. Currently, these results are qualitative, but if the delivery system can be standardized allowing the same rate of injection for all studies, then perhaps the results can be made more quantitative, and may be used to measure the therapeutic effects of the transplanted cells. The objective of this chapter was to introduce a new imaging technique and show its feasibility on clinical equipment (albeit with a pre-clinical large animal model of heart disease). Since we demonstrated the technique can localize

transplanted cells in relation to an underlying infarct, its role could be expanded to evaluate the efficacy of different cell transplant locations for stem cell therapy.

A final direction that this project may take is to combine the techniques developed in this thesis into a single study. Specifically: a study using a solid-state small field-of-view detector SPECT scanner coupled with a fast rotation CT to acquire first-pass perfusion CT may prove to be the best combination for imaging transplanted myocardial stem cells. The solid-state detector should improve SPECT counting statistics and scatter correction to image the transplanted cells for a longer period of time. Combining this with the localization aspect of the first-pass perfusion CT images could make this an interesting and powerful platform for cell tracking.

APPENDIX: Reproduction Permission – Chapter 4

WOLTERS KLUWER HEALTH LICENSE TERMS AND CONDITIONS

Nov 04, 2010

This is a License Agreement between Eric Sabondjian ("You") and Wolters Kluwer Health ("Wolters Kluwer Health") provided by Copyright Clearance Center ("CCC"). The license consists of your order details, the terms and conditions provided by Wolters Kluwer Health, and the payment terms and conditions.

All payments must be made in full to CCC. For payment instructions, please see information listed at the bottom of this form.

License Number	2542130293747
License date	Nov 04, 2010
Licensed content publisher	Wolters Kluwer Health
Licensed content publication	Nuclear Medicine Communications
Licensed content title	Small field-of-view cardiac SPECT can be implemented on hybrid SPECT/CT platforms where data acquisition and reconstruction are guided by CT
Licensed content author	Eric Sabondjian, Robert Stodilka, Tarik Belhocine, et al
Licensed content date	Jan 1, 2009
Volume Number	30
Issue Number	9
Type of Use	Dissertation/Thesis
Requestor type	Individual
Title of your thesis / dissertation	Improvements in Cardiac SPECT/CT for the Purpose of Tracking Transplanted Cells
Expected completion date	Dec 2010
Estimated size(pages)	135
Billing Type	Invoice
Billing Address	St. Joseph's Hospital Lawson Health Research Institute London, ON N6A 4V2 Canada
Customer reference info	
Total	0.00 USD
Terms and Conditions	

APPENDIX: Animal Ethics Approval – Chapter 2

Western

July 17, 2009

"This is the Original Approval for this protocol"

Dear Dr. Stodilka:

Your Animal Use Protocol form entitled:
Correcting for attenuation using slow and fast CT design in SPECT/CT
Funding Agency CRF-cardiac #R-08-262

has been approved by the University Council on Animal Care. This approval is valid from **July 17, 2009 to July 31, 2010.** The protocol number for this project is **2009-059**

1. This number must be indicated when ordering animals for this project.
2. Animals for other projects may not be ordered under this number.
3. If no number appears please contact this office when grant approval is received.
   If the application for funding is not successful and you wish to proceed with the project, request that an internal scientific peer review be performed by the Animal Use Subcommittee office.
4. Purchases of animals other than through this system must be cleared through the ACVS office. Health certificates will be required.

ANIMALS APPROVED FOR 4 Years

Species	Strain	Other Detail	Pain Level	Animal # Total for 4 Years
Dog	Canine-Hound X	~ 23 kg. F	B	5

REQUIREMENTS/COMMENTS
Please ensure that individual(s) performing procedures on live animals, as described in this protocol, are familiar with the contents of this document.
The holder of this Animal Use Protocol is responsible to ensure that all associated safety components (biosafety, radiation safety, general laboratory safety) comply with institutional safety standards and have received all necessary approvals. Please consult directly with your institutional safety officers.

c.c. Approved Protocol - R. Stodilka, J. Sykes, D. Forder
Approval Letter - R. Stodilka, J. Sykes, D. Forder

The University *of* Western Ontario
Animal Use Subcommittee / University Council on Animal Care
Health Sciences Centre, • London, Ontario • CANADA – N6A 5C1
PH: 519-661-2111 ext. 86770 • FL 519-661-2028 • www.uwo.ca / animal

APPENDIX: Animal Ethics Approval – Chapter 3

Western

07.01.08
*This is the 1ST Renewal of this protocol
*A Full Protocol submission will be required in 2008

Dear Dr. **Wisenberg**

Your Animal Use Protocol form entitled:

Optimizing the Administration of Marrow-derived Stem Cells to Repair Left Ventricular Structure and Function in a Canine Model of Myocardial Infarction

has had its yearly renewal approved by the Animal Use Subcommittee.

This approval is valid from **07.01.08** to **06.30.09**

The protocol number for this project remains as **2005-054**

1. This number must be indicated when ordering animals for this project.
2. Animals for other projects may not be ordered under this number.
3. If no number appears please contact this office when grant approval is received.
   If the application for funding is not successful and you wish to proceed with the project, request that an internal scientific peer review be performed by the Animal Use Subcommittee office.
4. Purchases of animals other than through this system must be cleared through the ACVS office. Health certificates will be required.

REQUIREMENTS/COMMENTS
Please ensure that individual(s) performing procedures on live animals, as described in this protocol, are familiar with the contents of this document.

c.c. Approved Protocol - G. Wisenberg, J. Sykes, D. Forder
Approval Letter - G. Wisenberg, J. Sykes, D. Forder

The **University** *of* **Western Ontario**
Animal Use Subcommittee / University Council on Animal Care
Health Sciences Centre, • London, Ontario • CANADA – N6A 5C1
PH: 519-661-2111 ext. 86770 • FL 519-661-2028 • www.uwo.ca / animal

ERIC SABONDJIAN

EDUCATION

DOCTORATE OF PHILOSOPHY Jan 2007 – Dec 2010
Medical Biophysics (Concentration: Medical Imaging)
Thesis title: *Improvements in Cardiac SPECT/CT for the Purpose of Tracking Transplanted Cells*
The University of Western Ontario, London, Ontario

MASTER OF SCIENCE Sept 2004 – Nov 2006
Medical Biophysics (Concentration: Medical Imaging)
Thesis title: *Improving Resolution in Wrist SPECT with Converging Collimators and CT Anatomical Priors*
The University of Western Ontario, London, Ontario

BACHELOR OF APPLIED SCIENCES Sept 1999 – May 2003
Electrical Engineering (Photonics and Microwaves Option)
4th year project: *Designed a Wide Area Network (WAN) in collaboration with NORTEL*
University of Ottawa, Ottawa, Ontario
Graduated with **Summa Cum Laude**

DIPLÔME D'ÉTUDE COLLÉGIAL (DEC) Sept 1997 – May 1999
Pure and Applied Science
John Abbott College, Sainte-Anne-de-Bellevue, Québec

ACADEMIC AWARDS

- OGSST Scholarship ($15000/yr) Jan 2010 - Dec 2010
- CIHR Vascular Training program ($10000/yr) Jan 2008 - Dec 2009
- Travel Award from Bioelectromagnetics Society ($1000) 2008
- Travel Award from Society of Molecular Imaging ($1000) 2008
- Schulich Graduate Scholarship ($6000/yr) Jan 2007 - Dec 2010
- Ontario Graduate Scholarship ($15000/yr) May 2005 - Apr 2006
- Western Graduate Scholarship ($1500/yr) May 2005 - Apr 2006
- Western Graduate Scholarship ($6000/yr) Sept 2004 - Apr 2005
- NORTEL NETWORKS Admission Scholarship ($2500/yr) Sept 1999 - May2003
- University of Ottawa Dean's Honour List Sept 1999 - May2003
- Faculty of Engineering Entrance Award ($1000) 1999

WORK EXPERIENCE

Ph.D. STUDENT / RESEARCH ASSISTANT Jan 2007 - Present

- Single Photon Emission Computed Tomography (SPECT) imaging of the heart
- Implementing new reconstruction algorithms for use in small field of view imaging
- Improving attenuation correction in cardiac SPECT/CT
- Development of fused first-pass perfusion CT and radio-labelled stem cell imaging

Additional Responsibilities

- Performed acceptance testing and NEMA report for newly installed SPECT/CT
- Quality control of gamma camera systems
- Helped with NRCan grant submission for seeking alternative production methods for Tc-99m
- **Clinical responsibilities**
    - Consult with nuclear medicine technologist and ensure proper equipment operation
    - Involved with meetings with commercial vendors, clinicians and senior hospital administration
    - Helping with the Ontario Ministry of Health HARP licence for an X-ray CT: 2007 HARP licence for X-ray CT - Designation 5252; Registration 286-1; Room B5-252 St. Joseph's Health Care - London - Equipment: Siemens Symbia T6 SPECT/CT
    - CT imaging technologist for Thames Valley Veterinary Services
    - Provided guidance to Drs J Taylor and R Rodriguez (London Regional Cancer Program) regarding SPECT/CT image fusion for a lung cancer study.
- Chairing cardiac lab meetings
- Knowledge on use of Co-60 irradiation source
- Included in protocol for cardiac stem cell therapy project [Jan. (2006) – present]
    - Acquire SPECT/CT scans + data analysis
- Lecturer
    - Conducted clinical physics rounds for Nuclear Medicine Residents
    - Provide lectures for radiation dosimetry at the University of Western Ontario

HUMAN RESEARCH PROTOCOL EXPERIENCE

- Nicholson RL (PI), Stodilka RZ, Pavlosky W and 15 others / An Observational Pilot Study of 18F-Sodium Fluoride (Na18F) Whole Body PET Scans in Patients for whom 99mTc MDP Bone Scans Would Normally be Indicated / HSREB 16340 / Funding: MOHLTC. Helped adapt the protocol from the Hamilton Health Sciences Centre template to the University of Western Ontario template; and adapted physics aspects (SJHC PET/CT scanner) and reviewed dosimetry.

MASTER'S STUDENT / RESEARCH ASSISTANT May 2004 –Nov 2006

Lawson Health Research Institute, London, Ontario

- Single Photon Emission Computed Tomography (SPECT) imaging of the wrist
- Implementing various Maximum A Posteriori (MAP) in reconstruction algorithms
- Developing the use of anatomical priors to improve image quality in SPECT
- Comparing fan-beam and pinhole collimators for wrist imaging

Additional Responsibilities

- Help with quality control experiments on Nuclear Medicine Gamma cameras

CO-OP STUDENT Jan 2002 - May 2002

University of Ottawa Heart Institute, Ottawa, Ontario

- Kinetic modelling of the heart using Rb-82 and FDG radio-active tracers
- Solving various differential equations for different types of models using Matlab and verifying everything by paper and pencil calculations

CO-OP STUDENT May 2001 - Sept. 2001

Defence Research and Development Canada (DRDC), Ottawa, Ontario
Electronic Counter Measures Division

- Upgrading the cruise missile simulation software
- Running simulations to verify the survivability of a ship undergoing a cruise missile attack

ENGINEERING RESEARCH ASSISTANT June - Sept 2000 and 2003

Naizil Coated Fabrics Inc., Bolton, Ontario

- Analysing and researching production line problems
- Preparing the company's first research laboratory
- Reading up on ISO 9002 protocols

INTERNATIONAL AND NATIONAL PRESENTATIONS

- **Sabondjian E**, Mitchell AJ, Wisenberg G, White J, Blackwood KJ, Sykes J, Deans L, Stodilka RZ, Prato FS. *'Hybrid SPECT and First-Pass Perfusion CT: Application in Cell Localization'*. Canadian Organization of Medical Physicists Conference 2010 (Oral Presenation)
- **Sabondjian E**, Mitchell AJ, Wisenberg G, Sykes J, Deans L, Stodilka RZ, Prato FS. *'Value of Contrast Enhanced CT in SPECT/CT for the Monitoring of Transplanted Stem Cells in a Canine Model'*. European Association of Nuclear Medicine Meeting 2009. (Poster Presentation: Selected 3rd best abstract in the Cardiology category)
- **Sabondjian E**, Lewden B, Prato FS, Stodilka RZ. *'Comparison of Slow CT vs Fast CT in Cardiac SPECT/CT'*. Imaging Network of Ontario, 2008. (Poster Presentation: Winner 3rd place)
- Stodilka RZ, Lewden B, Theberge J, **Sabondjian E**, Mitchell A, Dorrington L, Sykes J, Prato FS. *'Hybrid PET/MRI: Deriving a PET Attenuation map from Multi-Parameter MRI, in a canine'*, IEEE Medical Imaging Conference 2008. (Poster Presentation).
- Stodilka RZ, Lewden B, Theberge J, **Sabondjian E**, Mitchell A, Dorrington L, Sykes J, Prato FS. *'Hybrid PET/MRI: Deriving a PET Attenuation map from Multi-Parameter MRI, in a canine'*, Society of Molecular Imaging Conference 2008. (Poster Presentation).
- **Sabondjian E**, Lewden B, Prato FS, Stodilka RZ. *'Gated Cardiac SPECT/CT: Slow CT or Fast CT?'*, Society of Nuclear Medicine Conference 2008. (Oral Presentation).
- **Sabondjian E**, McKay JC, Stodilka RZ, Thomas AW, Keenliside L, Prato FS. *'Radio-Frequency Transmissions from Cellular Phone Do Not Interfere with Nuclear Medicine Brain Imaging Equipment'*, Bioelectromagnetic Society Annual Meeting 2008. (Poster Presentation).

- **Sabondjian E**, Stodilka RZ, Belhocine T, King M, Prato FS. *'Small Field of View (FOV) SPECT/CT for Cardiology: Theory and Preliminary Clinical Evaluation'*, IEEE Nuclear Science Symposium and Medical Imaging Conference, 2007. (Poster presentation)
- **Sabondjian E**, Belhocine T, Prato FS, Stodilka RZ. *'Clinical Evaluation of Small Field of View (FOV) SPECT/CT Reconstruction for Cardiac Imaging'*, Canadian Society of Nuclear Medicine, 2007. (Oral presentation)
- **Sabondjian E**, Stodilka RZ, Belhocine T, Prato FS. *'Single Photon Emission Computed Tomography / X-ray CT Using a Small Field of View (FOV) Gamma Camera: Theory and Preliminary Cardiac Clinical Scanning'*, Imaging Network of Ontario, 2007. (Poster presentation)
- **Sabondjian E**, Wells RG. *'Using CT priors in SPECT/CT wrist imaging'*, IEEE Nuclear Science Symposium and Medical Imaging Conference, 2006. (Poster presentation)
- **Sabondjian E**, Wells RG. *'Using CT prior information to improve small animal SPECT imaging',* Imaging Network of Ontario, 2006. (Poster presentation)
- **Sabondjian E**, Wells RG. *'Investigating pinhole SPECT for wrist imaging'*, IEEE Nuclear Science Symposium and Medical Imaging Conference, 2005. (Poster presentation)

RESEARCH AWARDS

- **Sabondjian E**, Mitchell AJ, Wisenberg G, Sykes J, Deans L, Stodilka RZ, Prato FS. *'Value of Contrast Enhanced CT in SPECT/CT for the Monitoring of Transplanted Stem Cells in a Canine Model'*. European Association of Nuclear Medicine Meeting 2009. (Poster Presentation: Selected 3rd best abstract in the Cardiology category)
- **Sabondjian E**, Lewden B, Prato FS, Stodilka RZ. *'Comparison of Slow CT vs Fast CT in Cardiac SPECT/CT'*. Imaging Network of Ontario, 2008. (Poster Presentation: Winner 3rd place)

PUBLICATIONS

Book Chapters

- Blackwood KJ, **Sabondjian E**, Goldhawk DE, Kovacs MS, Wisenberg G, Merrifield P, Prato FS, DeMoor JM, Stodilka RZ. *'Progress in Stem Cell Applications'*, Invited book chapter "Towards Imaging Guided Stem Cell Therapy". Nova Science Publishers Inc. 2008.
- Stodilka RZ, Lewden B, Jerosch-Herold M, **Sabondjian E**, Prato FS. *'Advanced Signal Processing, Theory and Implementation for Sonar, Radar and Non-Invasive Medical Diagnostic Systems'*, Invited book chapter "Examination of Contrast Agents in Medical Imaging using Physiologically-Constrained De-convolution". Editor: Stergios Stergiopoulos, PhD. CRC Press [in press, pub date Dec 2008].

Papers Published

- **Sabondjian E**, Stodilka RZ, Belhocine T, King M, Wisenberg G, Prato FS. *'Small Field-of-View Cardiac SPECT Can Be Implemented On Hybrid SPECT/CT Platforms Wherein Data Acquisition and Reconstruction are Guided by CT'*. Nuclear Medicine Communications. 2009; 30(9):718-726
- Mitchell AJ, **Sabondjian E**, Sykes J, Deans L, Zhu W, Lu X, Feng Q, Prato FS, Wisenberg G. *'Clearance Kinetics After Subendocardial or Subepicardial Injections of Endothelial Progenitor Cells in a Canine Myocardial Infarction Model'*. Journal of Nuclear Medicine. 2010; 51(3):413-417.

Papers Submitted

- **Sabondjian E**, Mitchell A, Wisenberg G, Sykes J, Deans L, White J, Stodilka RZ, Prato FS. *'Hybrid SPECT / Cardiac-Gated First-Pass Perfusion CT: Localizing Transplanted Cells Relative to Infarcted Myocardial Targets'*. (Submitted to Nuclear Medicine Communications: accepted pending revision)
- **Sabondjian E**, Stodilka RZ, Wisenberg G, King ME, Lewden B, Prato FS. *'Cardiac SPECT/CT: slow CT or fast CT'*. (Submitted to Physics in Medicine and Biology)

TECHNICAL AND PROFESSIONAL SKILLS

Computers

- Operating systems: Windows and Linux/Unix
- Languages: MATLAB, Simulink, C programming, and Assembly
- Software: Microsoft Office, Maple V, Minitab, Pspice (Circuit analysis), Seranade (Designed a microwave amplifier micro-strip circuit), Ensemble (Solved equivalent circuits for bends in micro-strips), and LabView

Laboratory

- SPECT imaging for bone and cardiac studies
- PET/CT whole body imaging
- MRI imaging for cardiac studies

Communication

- French and English (written and spoken)
- Armenian (spoken)
- Have given numerous presentations locally, nationally and internationally

INTERESTS

Martial arts, weight training, automobiles, running, tennis, squash, history, and reading

REFERENCES

Furnished upon request